UNIVERSITY OF COPENHAGEN
FACULTY OF SCIENCE

Master's thesis

Charge order in kagome metals

Emil Hellebek

Advisors: Brian Møller Andersen and Morten Holm Christensen

Submitted: May 20, 2022

Abstract

The discovery of coexisting time reversal symmetry breaking and superconductivity in the kagome metals AV_3Sb_5 (A = K, Cs, Rb) have made the scientific community pour huge efforts into understanding the nature of the materials, and a flurry of papers has been written in the last two years. Concurrent with the onset of the time reversal symmetry breaking, a charge ordering phase has been found in the materials that break translational symmetry. The phase is believed to form a Tri-Hexagonal or Star-of-David bond order in the kagome plane. In this thesis we investigate the new kagome metals starting from two tight-binding models: One considering the bare kagome lattice, the other using a materially specific model fitted to CsV_3Sb_5. We introduce interactions and decouple them using the unrestricted Hartree-Fock approximation, such that we can minimize the free energy using a self-consistency algorithm. In the phase diagrams for the bare kagome lattice, we find a large region where the Tri-Hexagonal bond order is the ground state, and regions with coexisting Tri-Hexagonal, charge density wave and spin density wave phase. Curiously, the latter of the two phases conserves the symmetries that AV_3Sb_5 breaks at the onset of the charge ordering phase. In the phase diagrams for the materially specific tight-binding model, we find a coexisting ferromagnet, imaginary spin density wave and imaginary charge density wave phase, with a loop current configuration that matches a previous proposal to the time reversal symmetry breaking order. With this study we have contributed to the current discussion on how the charge bond order emerges and how time reversal symmetry breaking might be linked to the charge bond order.

Acknowledgments

I would first like to acknowledge the tremendous help and guidance given to me by my supervisors Brian Møller Andersen and Morten Holm Christensen. I am thankful for the support given to me in understanding the physics behind the new materials, assisting me, when the algorithm was bugging, and helping me guide the project towards a fruitful end. Morten also needs my thanks, as he helped me proofread the final report yielding a much improved thesis.

Furthermore, I would like to thank the wider CMT group for the past nine months that have given me new acquaintances. Here the afternoons spend with many from the group, especially Morten, Clara N. Breiø and Henrik Røising have helped me wind down after days of research. I would also like to thank Anders E. Dahl for being office mates this past year having many fruitful discussions and good laughs to keep the spirits high.

I am further grateful for my parent's support and encouragement in the past nine months has helped me finalize the project. Finally, my fiancée Ida Rye Johansen has my utmost gratitude for the past nine months, where she has encouraged me and given me good advice about the project. Especially when I needed her help the most, she was there to guide me over the finish line.

Contents

1 Introduction **1**

2 AV_3Sb_5, A = K, Rb, Cs **3**
- 2.1 Lattice geometry and transport measurements . . . 3
- 2.2 Band structure and density functional theory . . . 4
- 2.3 Charge bond order . . . 6
- 2.4 Time reversal symmetry breaking . . . 8

3 The kagome lattice and tight-binding model **10**
- 3.1 The kagome lattice geometry . . . 10
- 3.2 Tight-binding model . . . 12

4 Mean field theory **18**
- 4.1 Mean field decoupling of the interaction . . . 19
- 4.2 Mean field Hamiltonian in momentum space basis . . . 20
- 4.3 Self-consistency algorithm . . . 22
- 4.4 Order parameters . . . 23
- 4.5 Candidate phases . . . 25

5 Results **29**
- 5.1 At the upper van Hove point . . . 29
- 5.2 Above the upper van Hove point . . . 33
- 5.3 At the lower van Hove point . . . 38
- 5.4 Summary of the results . . . 39

6 Seven band model **40**
- 6.1 Modifications to the interaction Hamiltonian . . . 42
- 6.2 Candidate phases . . . 43
- 6.3 Results . . . 43

7 Conclusion and outlook **47**

A Mean field decoupling for 3 band model **A1**

B Seven band model **B1**

C Mean field decoupling of the 7 band model **C1**

Chapter 1

Introduction

The study of new phenomena from simple lattice models is one way for theorists to work with condensed matter systems. The results of the studies can then be applied to materials hosting the simple lattice structure. One of such simple lattice is the kagome lattice, schematically drawn in Fig. 1.1, which was introduced by I. Syôzi in Ref. [1]. The lattice consists of corner sharing triangles, which means it can be an ideal host for magnetic frustration. If we consider three sites constituting a triangle with Ising-spins, where the spins want to be anti-parallel, we see that when two of the three spins have been fixed, the third spin is magnetically frustrated as it does not want to be spin-up or spin-down, as sketched in Fig. 1.1. From the built-in magnetic frustration, the lattice is considered to host exotic magnetic states [2].

The kagome lattice has also been found to interesting electronic properties from the band structure. The lattice host a completely flat band, yielding essentially infinitely heavy fermion, and a linear dispersion yielding massless Dirac fermions [3, 4]. Furthermore, at two chemical potentials other than the flat band the density of states diverges, yielding a so-called van Hove points [5]. Finally, the materials have been predicted to host superconductivity [6, 7].

A set of prototype kagome materials was discovered in 2019, see Ref. [8]. The compounds KV_3Sb_5, CsV_3Sb_5 and RbV_3Sb_5, collectively called AV_3Sb_5 where A stands for the alkali metal, were found to host a kagome lattice made of vanadium atoms. The resistivity of the materials was found to show typical metallic behavior [8], and the resistivity was further measured to be much larger in the plane with the kagome lattice than out-of-plane [9]. The Fermi surface, measured by angle resolved photoemission spectroscopy

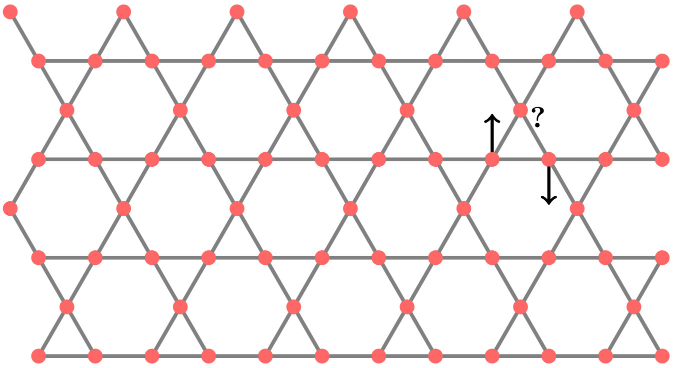

Figure 1.1: Schematic drawing of the kagome lattice. An example of the magnetic frustration is shown in the lattice.

(ARPES), revealed very small changes along the out-of-plane direction, which means the metals are quasi two-dimensional [10]. Shortly after their discovery, AV_3Sb_5 were found to be superconducting with the critical temperatures $T_C \approx 2.3\,\mathrm{K}$ for the cesium variant [9], $T_C \approx 0.93\,\mathrm{K}$ for the potassium variant [11] and $T_C \approx 0.75\,\mathrm{K}$ for the rubidium variant [12]. This has sparked an interest in the wider scientific community, as is seen research activity regarding the kagome lattice [13–35]. With the discovery of the materials, anomalies in the magnetization and heat capacity of the materials were detected. These anomalies have been linked to a phase transition where the metal enters a charge ordered phase [16, 20, 21]. The phase shows evidence of time reversal symmetry breaking, which persists to temperatures below superconductivity [17], thus the superconducting pairing lives in a time reversal symmetry broken state hinting at unconventional pairing mechanisms and the exotic phenomena.

In this thesis we will study the new kagome metals on a microscopic level, focusing on the charge ordered phase. To accomplish this, we will consider two tight binding models: One based on the pristine kagome lattice, and a materially specific multi-orbital tight-binding model published in Ref. [15]. We add interactions of the two the tight-binding models and use unrestricted Hartree-Fock approximation to obtain a single particle problem. By employing a self-consistency algorithm we obtain a phase diagram in the space defined by the interaction strengths.

The thesis is structured as follows: In Chapter 2 the new kagome metals AV_3Sb_5 are discussed, and some experimental results are presented. In Chapter 3 the kagome lattice and the symmetries of the lattice are discussed, and the tight binding model of the kagome lattice is solved. In Chapter 4 we introduce interactions to the system, and use mean field theory to obtain a single-particle problem, which can be solved via a self-consistency algorithm, also presented in this chapter. In Chapter 5 we present phase diagrams from the solutions to the self-consistency algorithm, and discuss the obtained results. In Chapter 6 a multi orbital tight-binding model is introduced to model AV_3Sb_5 more closely. We present phase diagrams of the self-consistent solutions to the tight-binding model with mean field decoupled interactions. In Chapter 7 we summarize the findings presented in the thesis and discuss further possible investigations of the new kagome metals.

Chapter 2

AV_3Sb_5, A = K, Rb, Cs

In this chapter we give a brief non-exhaustive overview of the new kagome metals. The focus of the overview will be the experiments relevant to the work presented in the thesis.

2.1 Lattice geometry and transport measurements

The lattice structure of AV_3Sb_5 is illustrated in Fig. 2.1. The materials have a hexagonal lattice of the alkali metal, a vanadium kagome layer between the layers of the alkali metal. This layer also has an antimony hexagonal lattice with the sites in the center of the kagome hexagons. Between the kagome layer and the hexagonal alkali layer is a honeycomb layer of antimony atoms. The three structural degrees of freedom are a_0, the in-plane distance between alkali sites; c_0 the out-of-plane distance between alkali sites, and the z-coordinate of the antimony site between the vanadium layer and the alkali layer [8]. The point group of a particular point in the lattice defines the possible symmetry operations of the lattice. The point group of AV_3Sb_5, choosing the on the antimony atom in the kagome plane as the center, is D_{6h}, meaning the system in the disordered state has a six-fold rotational

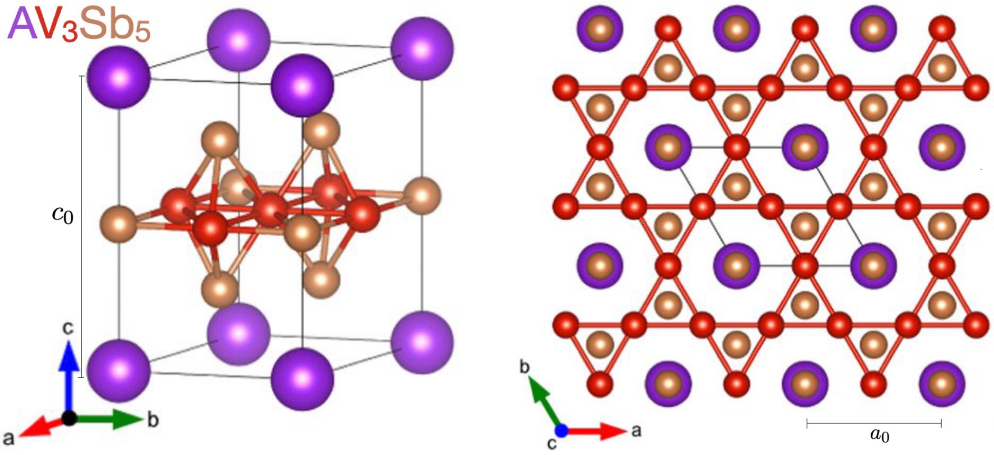

(a)

(b)

Figure 2.1: The lattice structure of AV_3Sb_5. The purple spheres represent the alkali atoms, the red spheres represent the vanadium atoms and the brown spheres represent the antimony atoms. The lattice constants are indicated on the lattice. **(a)** seeing the lattice structure in the out-of-plane direction **(b)** the lattice structure from the top, seeing a kagome net by vanadium atoms. Figures adapted from Ref. [8].

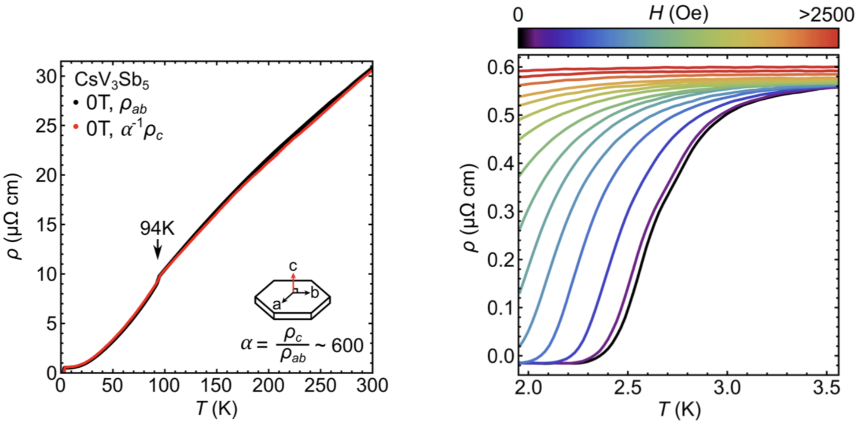

(a) **(b)**

Figure 2.2: Resistivity measurements for CsV_3Sb_5 at various temperatures. **(a)** Measurements of the resistivity in the kagome plane and out-of-plane resistivity in the normal state. **(b)** Resistivity measurements at low temperatures for a range of applied magnetic field strengths. A superconductivity transition is revealed, limited by applying a magnetic field. Figures are from Ref. [9].

symmetry, inversion symmetry, and mirror symmetries, with mirror planes both in the kagome plane and perpendicular to the kagome plane.

Results from the transport measurements of the resistivity of CsV_3Sb_5, presented in Ref. [9], are shown in Fig. 2.2. The resistivity displays typical metallic behavior for most temperatures, however, the in-plane resistivity is measured to be ~ 600 times smaller than the out-of-plane resistivity, revealing that the electrons in CsV_3Sb_5 primarily move in the kagome plane. Finally, an anomaly of the in-plane resistivity is found at 94 K, which has been linked to a phase transition into the previously mentioned charge bond order. At low temperatures, the resistivity decreases to zero revealing a superconducting state emerging with a critical temperature of $T_C \approx 2.3\,\mathrm{K}$. Similar measurements have been presented for the rubidium variant in Ref. [11] and for the potassium variant in Ref. [12]. The temperatures of the anomalies are slightly different in the three materials (102 K for RbV_3Sb_5 and 78 K for KV_3Sb_5), as well as the critical temperature of superconductivity (0.93 K for RbV_3Sb_5 and 0.75 K for KV_3Sb_5).

Regarding an overall magnetic structure both neutron scattering experiments [8] and muon spin relaxation experiments [34] have detected no long range magnetic order in the materials [8, 34]. The muon spin relaxation experimental technique is discussed in Section 2.4

2.2 Band structure and density functional theory

One method of calculating ground state properties of a many-body system is using density functional theory (DFT). This method is based on the fact that the ground state properties can be written as a functional of the ground state density. Finding the wave function is thus not necessary, if one knows how the Hamiltonian depends on the ground state density. While the kinetic term and the electron-electron interaction have a known dependence on the ground state density, how the so-called exchange-correlation potential depends on the ground state density is not generally known, but can be approximated using various methods and algorithms [36]. One application of DFT is calculations of the band structure

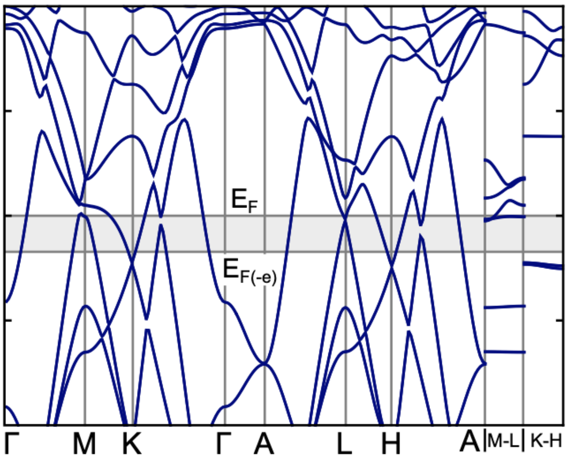

Figure 2.3: DFT calculated band structure of CsV_3Sb_5, along the high symmetry path. Γ is the center of the Brillouin zone, M is the center of an edge, K is at the vertex where $k_z = 0$. A, L and H, are equivalent to Γ, M and K at $k_z = \pi/c$. The in-plane part of the high symmetry path can be seen in Fig. 3.2. The Fermi energy is indicated along with the Fermi energy after deintercalation of cesium atoms ($\mathrm{E}_{\mathrm{F(-e)}}$). The plot is taken from [8].

and the Fermi surface, which has been done for the new kagome metals. In Fig. 2.3 the DFT calculated band structure of CsV_3Sb_5 are shown, following the high symmetry path around the Brillouin zone (see Fig. 2.4 for the path at $k_z = 0$). We notice here that the band structure has locally flat bands close to the Fermi energy at the M point (the center of an edge of the Brillouin zone). These parts of the bands yields a diverging density of states and are called van Hove points [5]. The van Hove points at M is a feature of the band structure of the kagome lattice, which will be shown in Section 3.2, when the band structure of the kagome lattice is found. Noticeably the bands around the Fermi energy are dominated by electrons of the vanadium orbitals, hinting at the importance the vanadium kagome layer has for the physics of the new kagome metals.

ARPES measurements have been conducted for the new kagome metals measuring the Fermi surface and the band structure [9, 10]. We present the ARPES measurements of the Fermi surface measured in Fig. 2.4. The surface at the center of the vanadium orbital comes from the antimony orbitals, where the bands closer to edge of the Fermi surface comes from the vanadium orbitals [10, 15]. Furthermore, the Fermi surface changes little when varying k_z [10], yielding us to describe the metal as quasi two-dimensional.

To qualitatively estimate the accuracy of the DFT calculations one can compare the band structure to ARPES measurements. Such a comparison was made in Ref. [9] for CsV_3Sb_5, where the calculations were seen to closely match the experimental results, see Fig. 2.5.

One application of DFT is to make a minimal tight-binding model fitted to the DFT calculated band structure. In this way the tight-binding model is made materially specific, capturing the physics of the real material, while being simple enough to be implemented effectively. Two of such minimal tight-binding models were presented in Ref. [15], where the focus was on capturing the van Hove points close to the Fermi surface, and calculate the impact of spin orbit coupling in the materials. We will discuss the tight binding models in greater detail in Chapter 6.

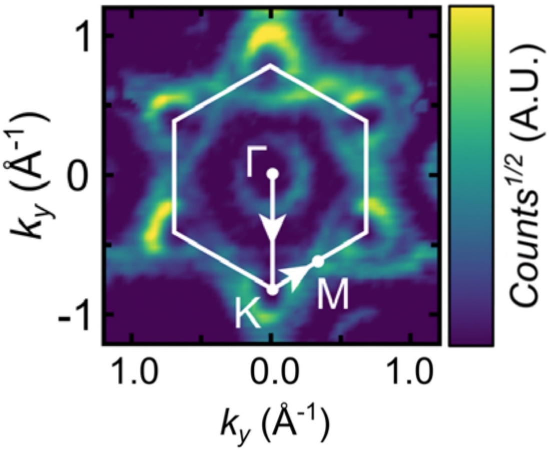

Figure 2.4: ARPES measurement of CsV_3Sb_5 at the Fermi energy for $k_z = 0$. Where the first Brillouin zone is indicated by the white lines. Figure is from Ref. [9]

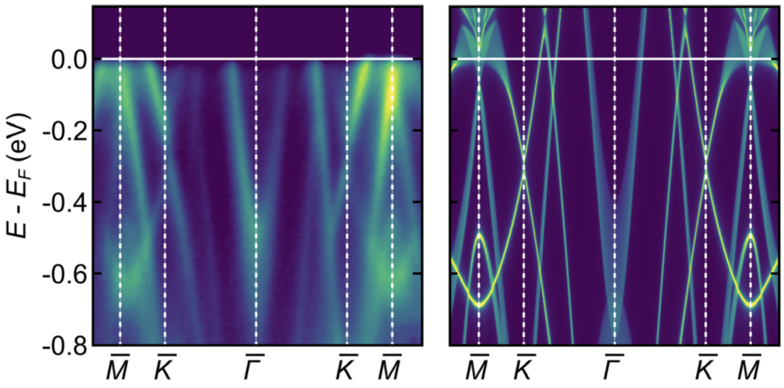

Figure 2.5: Band structure from ARPES measurements (left) and DFT calculations (right) for CsV_3Sb_5, following the high M-K-Γ-K-M path around the Brillouin zone. Excellent agreement is seen between the experiment and the calculations. Figure is from Ref. [9].

2.3 Charge bond order

The topographic images of scanning tunneling microscopy (STM) measurements of AV_3Sb_5 revealed a new superlattice structure of the materials, which breaks translation symmetry. The Fourier transform of the images of the STM, revealed that the phase breaks translational symmetry by doubling of the size of the unit cell along both in kagome plane lattice directions ($2a_0 \times 2a_0$), as is shown in Fig. 2.6. The order is not believed to break the rotational symmetry in the kagome plane [18]. The anomalies in the resistivity, seen in Fig. 2.2, heat capacity and magnetization have been linked to the phase transition to the new superlattice structure [37], meaning the critical temperature of the new order T_{CBO} is 78 K, 94 K and 103 K for KV_3Sb_5, CsV_3Sb_5 and RbV_3Sb_5 respectively [16, 20, 21].

Due to the band structure of the kagome lattice, see Section 3.2, the order in the kagome metals is thought to be a charge bond order. Such an order adds an effective term to the Hamiltonian $H_{\text{CBO}} = \Delta_{ij} c_i^\dagger c_j$, which is summed over neighboring sites i and j. This term means the effective hopping strength between two sites is modulated throughout the lattice, yielding to the conclusion that some sites are coupled more strongly to each other, and some sites are coupled more weakly to each other. The symmetry requirements of the

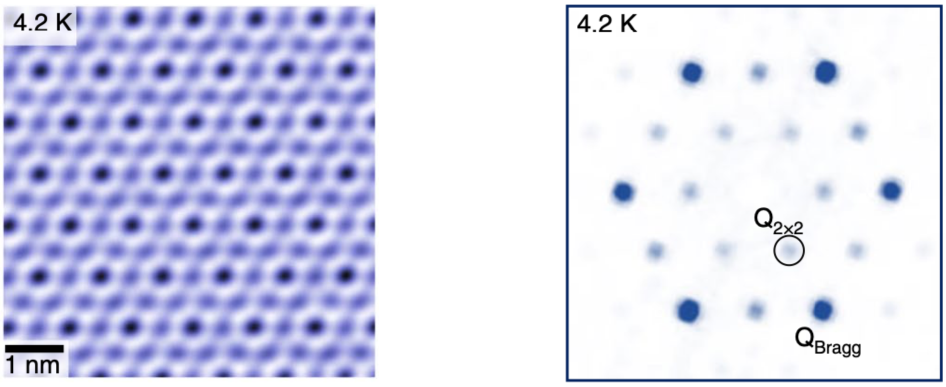

(a)

(b)

Figure 2.6: **(a)** The topographic image of the charge order in KV_3Sb_5 taken at 4.2 K and **(b)** its Fourier transform. A peak at the $2a_0 \times 2a_0$ superlattice structure is clearly seen in the Fourier transform. Figures are from Ref. [16].

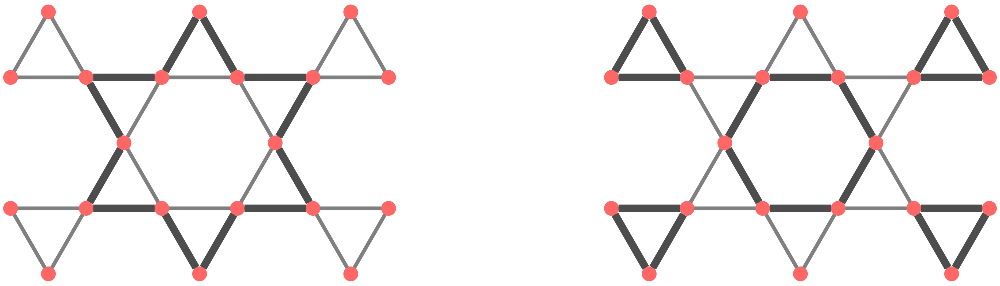

(a)

(b)

Figure 2.7: Schematic drawings of the **(a)** Star-of-David **(b)** Tri-Hexagonal bond orders on the kagome lattice. The gray dots are the sites in the kagome lattice, the thick black lines represent strong bonds, and the thin gray lines represent weak bonds.

phase yield to two candidate phases: The Tri-Hexagonal and Star-of-David. Both phases are schematically drawn on the bare kagome lattice in Fig. 2.7.

The exact spatial modulation of the CBO is still under some debate, especially regarding how translational symmetry is broken along the out-of-plane direction and whether the global six-fold rotational symmetry is reduced to a two-fold rotational symmetry. For the potassium and rubidium variants it is generally accepted that the charge order breaks rotational symmetry and that the unit cell is doubled in the out-of-plane direction, yielding a combined $2a_0 \times 2a_0 \times 2c_0$ phase [19, 25, 30, 31, 35]. Some experiments see a quadrupling of the unit cell in CsV_3Sb_5 in the out-of-plane direction ($2a_0 \times 2a_0 \times 4c_0$), where the order conserves the six-fold rotational symmetry of the disordered state [18, 32]. Other studies have found the order is similar to the order in the potassium and rubidium variants, meaning the new unit cell has the size $2a_0 \times 2a_0 \times 2c_0$ and reduces the rotational symmetry to a two-fold rotational symmetry [20, 26, 30, 31, 35].

Proposals for the microscopic modulations of the full charge bond order have appeared. Two propositions for a $2a_0 \times 2a_0 \times 2c_0$ phase can be seen in Fig. 2.8, where one phase reduces to a two-fold rotational symmetry, while the other conserves six-fold rotational symmetry. Propositions for the $2a_0 \times 2a_0 \times 4c_0$ phase, consists of one Tri-Hexagonal layer followed by three layers with either the Star-of-David configuration or no bond configuration [18, 32].

Finally, in CsV_3Sb_5, a different in-plane CBO has been reported by STM measure-

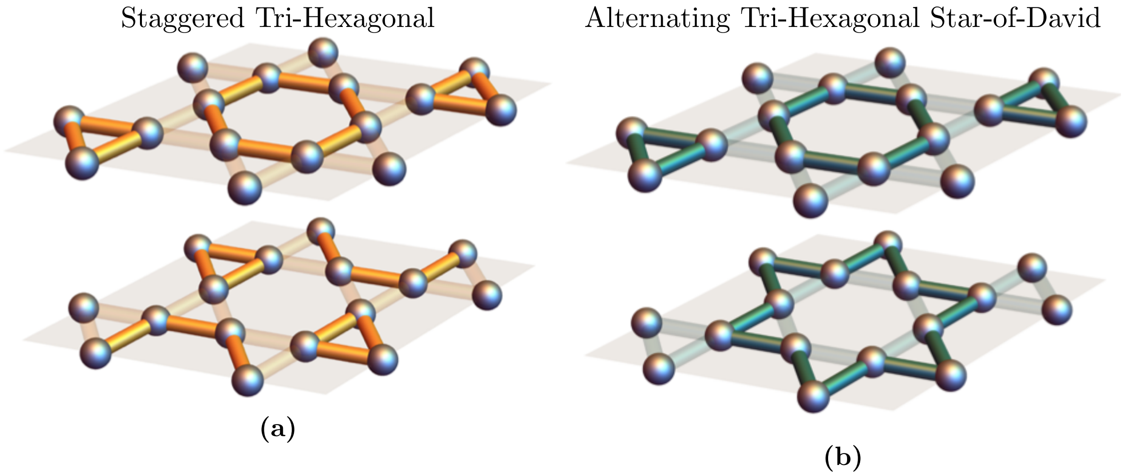

Figure 2.8: Schematic drawings of the **(a)** staggered Tri-Hexagonal **(b)** alternating Tri-Hexagonal Star-of-David. While the staggered Tri-Hexagonal reduces to a two-fold rotational symmetry, the alternating Tri-Hexagonal Star-of-David conserves rotational symmetry. Both break translational symmetry of the form a new unit cell of the size $2a_0 \times 2a_0 \times 2c_0$. Figures are from Ref. [13].

ments, with a critical temperature between 50 K and 60 K. This charge bond order quadruples the unit cell in one primary direction ($4a_0$) yielding a rotational symmetry breaking order[20]. However, bulk probe x-ray diffraction measurements did not detect the ordered phase, instead linking the $4a_0$ order to how the surface was cleaved and small shifts in the bonds between antimony and vanadium atoms [26].

2.4 Time reversal symmetry breaking

Muon spin relaxation experiments have revealed a time reversal symmetry breaking order in the new kagome metals. The muon spin relaxation experimental method consists of implanting spin-polarized muons into the studied materials. The muon's spin will then rotate due to local magnetic fields. After some time the muon will decay into a positron among other particles. The direction of the radiated positron depends on the direction of the muon's spin. By fitting the decay rates, one can estimate the effective local magnetic field felt by the muons. A sudden change in the relaxation rates, can hence be linked to the emergence of magnetic fields, yielding a time reversal symmetry broken state.

In Ref. [17] a muon spin relaxation experiment for KV_3Sb_5, and some results of the experiments are shown in Fig. 2.9. At the onset of the charge bond ordered phase, a change is seen in the relaxation rates both with and without transverse magnetic fields. The change of the relaxation rates in the zero field experiment could come from the change in where the muons stop in the material after the charge bond order sets in. However, the experiments with a transverse magnetic field indicates that an effective magnetic field has appeared in the material, thus a time reversal symmetry broken order exists. The size of the effective magnetic field can be estimated from the relaxation rates, yielding $B_{\text{eff}} = 0.3\,\text{G}$. Furthermore, during the transition to the superconducting state, no change in the relaxation rates of the muons were found, meaning superconductivity exists in a time reversal broken state. For the cesium variant, similar experiments have revealed time reversal symmetry breaking, however the critical temperature of the time reversal symmetry breaking has been reported both at a lower temperature the onset of

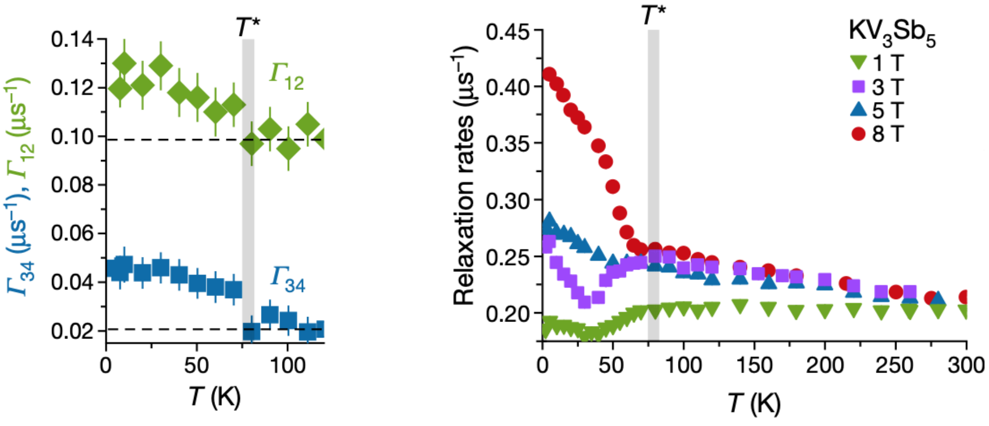

(a) (b)

Figure 2.9: Muon spin relaxation rates for KV_3Sb_5. T^* indicates the onset of the charge bond ordered phase. **(a)** Zero transverse magnetic field has been applied, where Γ_{12} is the rate for the out-of-plane direction, and Γ_{34} is the direction in the kagome plane. **(b)** Transverse magnetic field has been applied, with the strengths indicated. The relaxation rates are in the kagome plane. Figures are from Ref. [17].

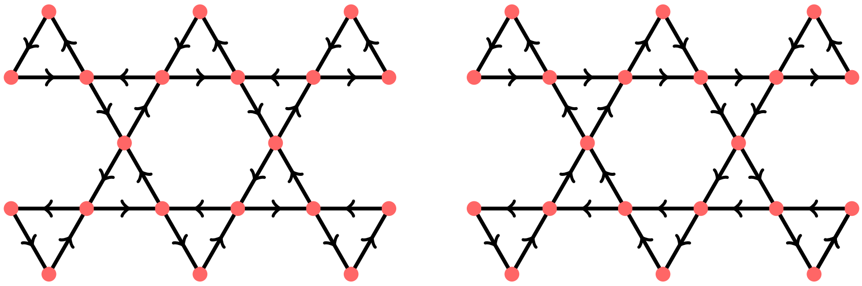

(a) (b)

Figure 2.10: Schematic drawings of current orders proposed in **(a)** Ref. [17] and **(b)** Ref. [29]. As can be seen form the drawings both current orders conserve the rotational symmetry, and **(a)** translational symmetry is conserved in **(a)** and broken in **(b)**.

the charge bond order [27] and as having the same critical temperature as the charge bond order [33]. In the rubidium variant the muon spin relaxation experiments reveal a time reversal symmetry breaking at the same temperature as the charge bond order [24]. Magneto optical Kerr effect experiments on all three compounds have revealed time reversal symmetry breaking in with the same critical temperature as the charge bond order [31].

As discussed in Section 2.1, the materials show no overall magnetic structure. An explanation of the time reversal symmetry breaking comes with the charge bond order parameter taking complex values. Such a phase would yield loop currents in the ground state. Various proposals for loop currents in the kagome lattice have been presented, with two of them schematically drawn on the kagome lattice in Fig. 2.10.

Chapter 3

The kagome lattice and tight-binding model

From the discussion of the band structure, Fermi surface and the transport measurements in Sections 2.1 and 2.2, we know that AV_3Sb_5 is quasi two-dimensional with the kagome layer made of vanadium atoms constituting the important bands around the Fermi energy. We thus start by modelling the kagome metals with a single orbital pristine kagome lattice.

3.1 The kagome lattice geometry

The kagome lattice is schematically drawn in Fig. 3.1. It is a two-dimensional hexagonal lattice with the primitive lattice vectors

$$\mathbf{t}_1 = a \begin{pmatrix} 1 & 0 \end{pmatrix}, \qquad \mathbf{t}_2 = a \begin{pmatrix} \frac{1}{2} & \frac{\sqrt{3}}{2} \end{pmatrix}, \tag{3.1}$$

where a is the distance between unit cells. For the remainder of the thesis we set $a = 1$. The unit cell consists of three sites, denoted A, B and C, and they are labelled in Fig. 3.1. The basis vectors, i.e. positions of sites in the unit cell, are

$$\mathbf{d}_A = \begin{pmatrix} \frac{1}{2} & 0 \end{pmatrix}, \qquad \mathbf{d}_B = \begin{pmatrix} \frac{1}{4} & \frac{\sqrt{3}}{4} \end{pmatrix}, \qquad \mathbf{d}_C = \begin{pmatrix} 0 & 0 \end{pmatrix}, \tag{3.2}$$

where we note that $2\mathbf{d}_\alpha$ is a lattice vector [3, 6, 38].

We consider the spatial symmetries of kagome lattice, as we want to examine what possible symmetries an ordered phase can break. By definition a lattice has translational symmetry, which in this case is given by the primitive lattice vectors in Eq. (3.1). The point group of the kagome lattice is D_6 [39]. Each group is defined by its generators, i.e. the symmetry operations from which all other symmetry operations of the point group can be generated by repeated application, and D_6 has two generators: A six-fold rotation (C_6) and a reflection (σ). An example of the axis of rotation and the median plane of reflection are shown in Fig. 3.1.

For systems with continuous translational symmetry, the momentum space becomes a better basis to work in as states are defined by their momentum. For systems with discreet translational symmetry in real space, there exist a translational symmetry in momentum space as well, called the reciprocal lattice. This means that two spatial modulations with momenta $\mathbf{k}$ and $\mathbf{k} + \mathbf{G}$, where $\mathbf{G}$ is a reciprocal lattice vector, will be indistinguishable on real space lattice. The primitive vectors of the reciprocal lattice $\mathbf{g}_n$ are defined such that

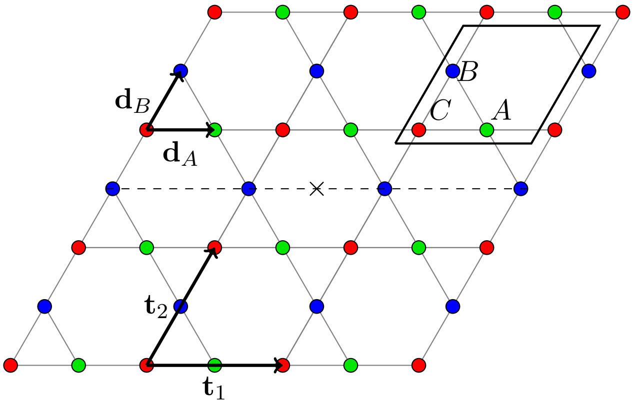

Figure 3.1: The kagome lattice, where the dots represent the different lattice sites. On the figure we show our definition of the sublattice indices. The primitive lattice vectors are shown together with the unit cell indicated by the black parallelogram, the primitive lattice vectors, the basis vectors and an example of the axis with six-fold rotational symmetry, symbolized by ×, and a mirror plane indicated by the dashed line.

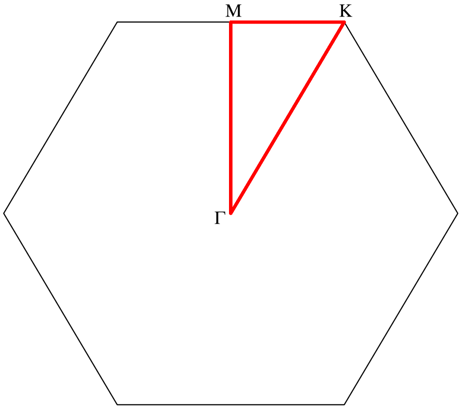

Figure 3.2: The first Brillouin zone of the kagome lattice. The high symmetry points Γ, M and K are marked. The high symmetry path of the lattice is shown with the red line.

$\mathbf{t}_m \cdot \mathbf{g}_n = 2\pi\delta_{mn}$. The primitive vectors of the reciprocal lattice of the hexagonal lattice are

$$\mathbf{g}_1 = 2\pi \begin{pmatrix} 1 & -\frac{1}{\sqrt{3}} \end{pmatrix}, \qquad \mathbf{g}_2 = 2\pi \begin{pmatrix} 0 & \frac{2}{\sqrt{3}} \end{pmatrix}. \tag{3.3}$$

We can from this partition momentum space in zones, where each zone contains all the momenta creating unique spatial modulations, called Brillouin zones. The Brillouin zone formed by the momenta closest to the origin is the first Brillouin zone, and the first Brillouin zone of the kagome lattice is shown in Fig. 3.2. The symmetries of the lattice is captured in momentum space, meaning we can consider certain points of high symmetry, that are invariant under symmetry operations: Γ, the center of the Brillouin zone; M, the center of an edge, and K, the vertex.

3.2 Tight-binding model

To consider how electrons forms ordered phases on the kagome lattice, we need to consider how electrons behave in the lattice. We consider the simplest form of the tight-binding model, where electrons can hop between neighboring sites defined by $t > 0$. All sites in the kagome lattice have four neighboring sites: The two other sites in the same unit cell, and two sites in different unit cells. The intra-unit cell contribution to the tight-binding Hamiltonian is

$$H_{TB}^{\text{intra}} = -t \sum_{\mathbf{R}\sigma} \sum_{\alpha \neq \beta} c_{\mathbf{R}\alpha\sigma}^{\dagger} c_{\mathbf{R}\beta\sigma}, \tag{3.4}$$

where we have introduced the creation (annihilation) operator $c_{\mathbf{R}\alpha\sigma}^{\dagger}$ ($c_{\mathbf{R}\alpha\sigma}$), which creates (annihilates) a spin-σ particle at the α site located in the unit cell at $\mathbf{R}$. While this notation looks daunting, it allows us to separate the translationally invariant part, i.e. the lattice vector, from the sublattice index, which is convenient for the coming Fourier transform.

The inter-unit cell contribution is not found as trivially, since we need to be certain what unit cell the neighboring site is in. To accomplish this, we define the vector from site α to site β in the same unit cell

$$\mathbf{a}_{\alpha\beta} \equiv \mathbf{d}_{\beta} - \mathbf{d}_{\alpha} \tag{3.5}$$

which trivially fulfill the relation $\mathbf{a}_{\alpha\beta} = -\mathbf{a}_{\beta\alpha}$. The vector connecting site α to its nearest neighbor β site in a different unit cell is $-\mathbf{a}_{\beta\alpha}$. Hence, the nearest neighbor β site of the α site in the unit cell at lattice vector $\mathbf{R}$, is located at $\mathbf{R} + \mathbf{d}_{\alpha} - \mathbf{a}_{\alpha\beta}$, which can be rewritten as $\mathbf{R} - 2\mathbf{a}_{\alpha\beta} + \mathbf{d}_{\beta}$. Since $2\mathbf{a}_{\alpha\beta}$ is a lattice vector, $\mathbf{R} - 2\mathbf{a}_{\alpha\beta}$ is the lattice vector of the unit cell with the β site. Hence, we can write inter-unit cell contribution to the tight-binding Hamiltonian

$$H_{TB}^{\text{inter}} = -t \sum_{\mathbf{R}\sigma} \sum_{\alpha \neq \beta} c_{\mathbf{R}\alpha\sigma}^{\dagger} c_{\mathbf{R}-2\mathbf{a}_{\alpha\beta}\beta\sigma}, \tag{3.6}$$

yielding the combined tight-binding Hamiltonian in the real space basis

$$H_{TB} = -t \sum_{\mathbf{R}\sigma} \sum_{\alpha \neq \beta} \left(c_{\mathbf{R}\alpha\sigma}^{\dagger} c_{\mathbf{R}\beta\sigma} + c_{\mathbf{R}\alpha\sigma}^{\dagger} c_{\mathbf{R}-2\mathbf{a}_{\alpha\beta}\beta\sigma} \right). \tag{3.7}$$

As we know from Bloch's theorem, the wave functions of the states in a periodic potential, like a lattice, are modulated plane waves, where the modulation has the same period as the potential. This means that the solution to the tight-binding Hamiltonian is most easily obtained in the momentum space basis. We consider a system of N unit cells, and assume that the system has periodic boundary conditions, meaning we can Fourier transform the annihilation operators

$$c_{\mathbf{R}\alpha\sigma} = \frac{1}{\sqrt{N}} \sum_{\mathbf{k}} e^{i\mathbf{k}\cdot\mathbf{R}} c_{\mathbf{k}\alpha\sigma}, \tag{3.8}$$

where we have chosen to let the position in real space associated with each operator be the position of the unit cell. This choice of gauge is convenient as it is invariant under a translation in momentum space with any reciprocal lattice vector $\mathbf{G}$, i.e. $c_{\mathbf{k}\alpha\sigma} = c_{\mathbf{k}+\mathbf{G}\alpha\sigma}$.

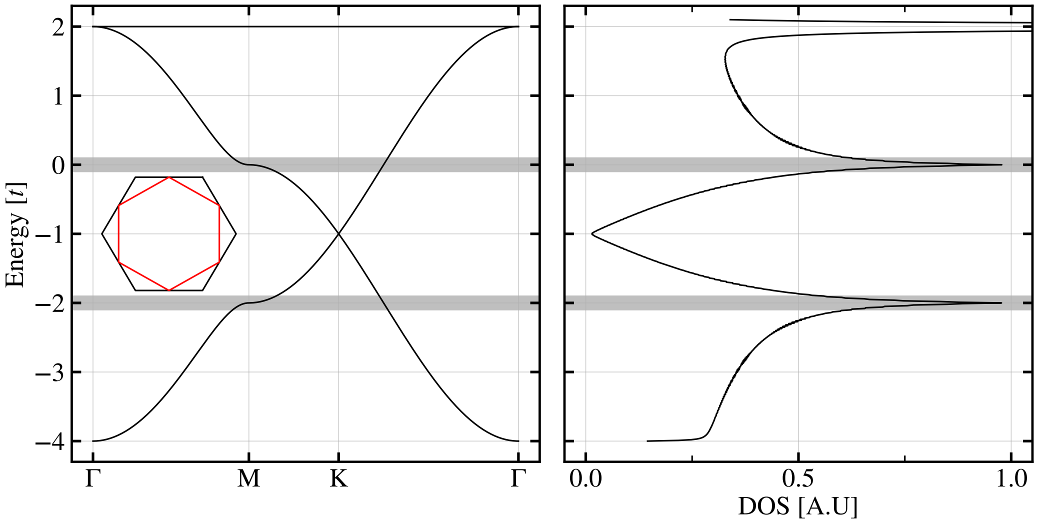

(a) **(b)**

Figure 3.3: **(a)** The band structure of kagome lattice. The inset shows the Fermi surface at the van Hove points. **(b)** The density of states at the different energies. The two gray regions marks the upper and lower van Hove points, as can be seen by the diverging density of states.

The tight-binding Hamiltonian can now be written in the momentum space basis

$$H_{TB} = -t \sum_{\mathbf{k}\alpha\sigma} \sum_{\beta\neq\alpha} \left(1 + e^{-2i\mathbf{k}\cdot\mathbf{a}_{\alpha\beta}}\right) c^\dagger_{\mathbf{k}\alpha\sigma} c_{\mathbf{k}\beta\sigma}, \tag{3.9}$$

where the sum over momenta is over the first Brillouin zone. All sums over momenta will have this property unless otherwise specified. This tight-binding Hamiltonian is block diagonal, meaning if we define a vector of the creation operators $\mathbf{c}^\dagger_{\mathbf{k}\sigma} = \left(c^\dagger_{\mathbf{k}A\sigma}, c^\dagger_{\mathbf{k}B\sigma}, c^\dagger_{\mathbf{k}C\sigma}\right)$, the Hamiltonian can be rewritten as

$$H_{TB} = \sum_{\mathbf{k}\sigma} \mathbf{c}^\dagger_{\mathbf{k}\sigma} h_{\mathbf{k}} \mathbf{c}_{\mathbf{k}\sigma}, \tag{3.10}$$

where $h_{\mathbf{k}}$ is

$$h_{\mathbf{k}} = -t \begin{pmatrix} 0 & 1 + e^{-2i\mathbf{k}\cdot\mathbf{a}_{AB}} & 1 + e^{-2i\mathbf{k}\cdot\mathbf{a}_{AC}} \\ 1 + e^{-2i\mathbf{k}\cdot\mathbf{a}_{BA}} & 0 & 1 + e^{-2i\mathbf{k}\cdot\mathbf{a}_{BC}} \\ 1 + e^{-2i\mathbf{k}\cdot\mathbf{a}_{CA}} & 1 + e^{-2i\mathbf{k}\cdot\mathbf{a}_{CB}} & 0 \end{pmatrix}, \tag{3.11}$$

The Hamiltonian can be diagonalized analytically yielding three energy bands

$$\epsilon_1(\mathbf{k}) = t + tA_{\mathbf{k}}, \qquad \epsilon_2(\mathbf{k}) = t - tA_{\mathbf{k}}, \qquad \epsilon_3(\mathbf{k}) = 2t, \tag{3.12}$$

where $A_{\mathbf{k}} = \sqrt{4\left[\cos^2(\mathbf{k}\cdot\mathbf{a}_{AC}) + \cos^2(\mathbf{k}\cdot\mathbf{a}_{AB}) + \cos^2(\mathbf{k}\cdot\mathbf{a}_{BC})\right] - 3}$ [3, 4]. The band structure is shown in Fig. 3.3a. The density of states $d(\omega)$ can be calculated using, $d(\omega) = \sum_{\mathbf{k}} A(\mathbf{k}, \omega)$, where $A(\mathbf{k}, \omega) = -2\Im[G^R(\omega, \mathbf{k})]$ is the spectral function, $G^R(\omega, \mathbf{k})$ is the retarded Greens function which for a non-interacting system is given by $G^R(\omega, \mathbf{k}) = (\omega - \xi_{\mathbf{k}} + i0^+)^{-1}$ where $\xi_{\mathbf{k}} = \epsilon(\mathbf{k}) - \mu$ is the dispersion, μ is the chemical potential and 0^+ is an infinitesimal small positive number. The density of state of the kagome lattice is shown in Fig. 3.3b. From the density of state three van Hove singularities, i.e. energies

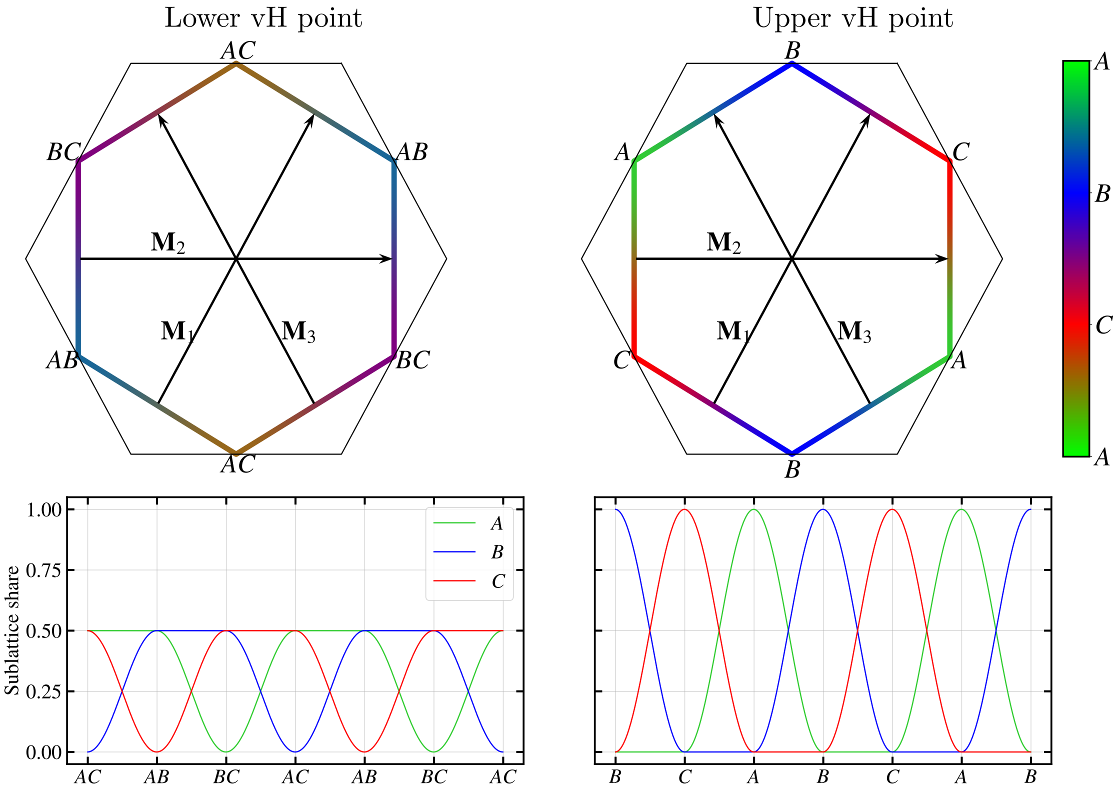

(a) **(b)**

Figure 3.4: The Fermi surface at the **(a)** lower and **(b)** upper van Hove (vH) points, with a plot of the weight of each sublattice around the Fermi surface, where the sites A, B and C are represented by the yellow, blue and red colors. The sublattice label(s) indicate which sublattices are present at the vertices of the Fermi surface. The Fermi surface nesting vectors are drawn, having $\mathbf{M}_1 = \mathbf{g}_1/2$, $\mathbf{M}_2 = \mathbf{g}_2/2$ and $\mathbf{M}_3 = -\mathbf{M}_1 - \mathbf{M}_2$, modulo reciprocal lattice vectors.

where the density of state diverges [5], are present in the kagome lattice. One comes from the completely flat band, which we will ignore, and the other two are marked in Fig. 3.3b by the gray shaded regions, and we will call them the upper and lower van Hove points.

The Fermi surface at the two van Hove points is shown in the inset on Fig. 3.3a. The Fermi surface forms a regular hexagon, where the vertices of the Fermi surface are at the M point of the first Brillouin zone. We can compare the Fermi surface at these points to the ARPES measurements of AV$_3$Sb$_5$ in Fig. 2.4. We here see that the vanadium bands close to the edge of the first Brillouin zone fits with the regular hexagon of the Fermi surface of the van Hove point. Since the Fermi surface forms a regular polygon with an even number of edges, we have to consider nesting effects. Nesting is defined as a non-zero wave vector $\mathbf{Q}$, called the nesting vector, satisfying the equation $\xi_{\mathbf{k}} = -\xi_{\mathbf{k}+\mathbf{Q}}$ for an ensemble of wave vectors $\mathbf{k}$ close to a Fermi wave vector [40]. Assuming all $\mathbf{k}$ are on the Fermi surface, we get the further condition, $\xi_{\mathbf{k}} = \xi_{\mathbf{k}+\mathbf{Q}} = 0$. As the only excitable states at low temperatures lie close to the Fermi surface, an excitation with this particular wave vector can excite more states than other wave vectors. Thus, an order modulated with a nesting vector is more probable to be found in the system than orders modulated by different wave vectors, and since the nesting vector is non-zero by construction, the orders enhanced by nesting effects break translational symmetry. The nesting vectors of the Fermi surface at the van Hove points are $\mathbf{M}_1 = \mathbf{g}_1/2$, $\mathbf{M}_2 = \mathbf{g}_2/2$ and $\mathbf{M}_3 = -\mathbf{M}_1 - \mathbf{M}_2$. The spatial modulation represented by the nesting vectors correspond to a doubling of the unit cell, along $\mathbf{t}_1$, $\mathbf{t}_2$ and $\mathbf{t}_2 - \mathbf{t}_1$ respectively. Conclusively, the Fermi surface at the van Hove points means, ordered phases breaking translational symmetry by doubling the size of the unit cell along either of the primitive lattice vectors are more probable to occur in the system.

However, electrons with a given momentum at the Fermi surface, do not have an equal probability of being measured at either sublattice [6, 7, 10, 41], as can be seen by the sublattice weights around the Fermi surface in Fig. 3.4. This means, that only certain orders will be enhanced from the nesting. Starting with the lower van Hove point, and taking an order with wave vector $\mathbf{Q} = \mathbf{M}_2$ as an example, the sublattice B is dominating at all parts of the two edges connected by $\mathbf{M}_2$, whereas A and C, changes weight. The means that a doubling of the unit cell in the direction of $\mathbf{t}_2$ by an order involving the operators $c^\dagger_{\mathbf{k}B} c_{\mathbf{k}+\mathbf{M}_2 B}$ is enhanced by nesting effects, as opposed to order involving $c^\dagger_{\mathbf{k}A} c_{\mathbf{k}+\mathbf{M}_2 A}$ or $c^\dagger_{\mathbf{k}C} c_{\mathbf{k}+\mathbf{M}_2 C}$. Similar arguments can be made for the other nesting vectors, such that $\mathbf{M}_1$ enhances orders with site A and $\mathbf{M}_3$ enhances orders with site C. Turning to the upper van Hove point, again considering orders with wave vector $\mathbf{Q} = \mathbf{M}_2$, we first see that the B site is absent from the entire edge, meaning any order involving this site will be unaffected by nesting. The other two sites do not dominate both parts of the Fermi surface connected by $\mathbf{M}_2$, instead if A dominates at momentum $\mathbf{k}$, C dominates at $\mathbf{k} + \mathbf{M}_2$ and vice versa. This means that bond orders involving sites A and C are enhanced most by nesting vector $\mathbf{M}_2$. Similar arguments yield that bond orders involving sites B and C are enhanced by $\mathbf{M}_1$ and bond orders involving sites A and B are enhanced by $\mathbf{M}_3$. Conclusively, at the lower van Hove point, site orders are enhanced by the nesting effects, connecting a site to each nesting vectors, whereas at the upper van Hove point, bond orders are enhanced by nesting effects, connecting a specific bond to each nesting vector.

The superlattice structure of the charge order in the kagome metals has a translational symmetry breaking, which matches the spatial modulation of the nesting vectors at the van Hove point. Furthermore, it is indicated that the van Hove points close to the Fermi energy of $\mathrm{AV_3Sb_5}$ are reminiscent of the upper van Hove point in the kagome band structure [10, 22]. This has lead the scientific community to believe the superlattice structure is formed by modulations of the bonds. The bond modulations enhanced by the nesting effects can combine into the Tri-Hexagonal or Star-of-David bond orders depicted in Fig. 2.7, and they are the only possible combination that conserves the symmetries of the D_6 point group. We will thus focus on these two ordered states, when searching for phases in Chapter 5.

Since we look for translational symmetry breaking phases with the primitive lattice vectors $\tilde{\mathbf{t}}_1 = 2\mathbf{t}_1$ and $\tilde{\mathbf{t}}_2 = 2\mathbf{t}_2$, we have to adjust the size of the reciprocal lattice. The new primitive vectors of the reciprocal lattice are $\mathbf{M}_1$ and $\mathbf{M}_2$, meaning the first Brillouin zone consists of all the momenta closer to Γ than any of the M points in the first Brillouin zone of the translational symmetry conserving system. We will call the first Brillouin zone defined by the primitive vectors $\mathbf{M}_1$ and $\mathbf{M}_2$ the reduced Brillouin zone (RBZ) and the first Brillouin zone defined by the primitive vectors in Eq. (3.3) for the full Brillouin zone (FBZ). Any sum over the full Brillouin zone can be rewritten in terms of sums over the reduced Brillouin zone

$$\sum_{\mathbf{k}\in\mathrm{FBZ}} f(\mathbf{k}) \longrightarrow \sum_{\mathbf{k}\in\mathrm{RBZ}} \left[f(\mathbf{k}) + f(\mathbf{k}+\mathbf{M}_1) + f(\mathbf{k}+\mathbf{M}_2) + f(\mathbf{k}+\mathbf{M}_3) \right]. \tag{3.13}$$

We now assume that the tight-binding has a reduced translational symmetry, matching a

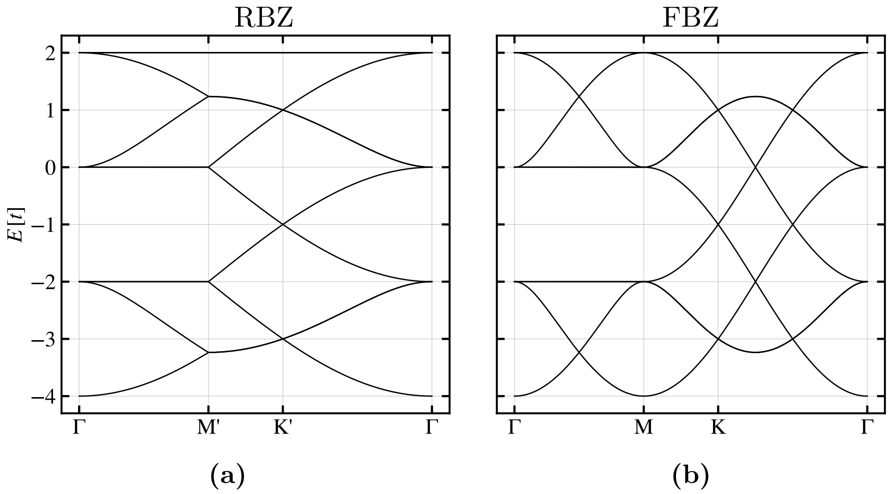

Figure 3.5: The band structure of the Hamiltonian in Eq. (3.14) following the high symmetry path of **(a)** the reduced Brillouin zone **(b)** the full Brillouin zone. The bands from the translational symmetry conserving Hamiltonian can be seen, along with the bands folded onto the path.

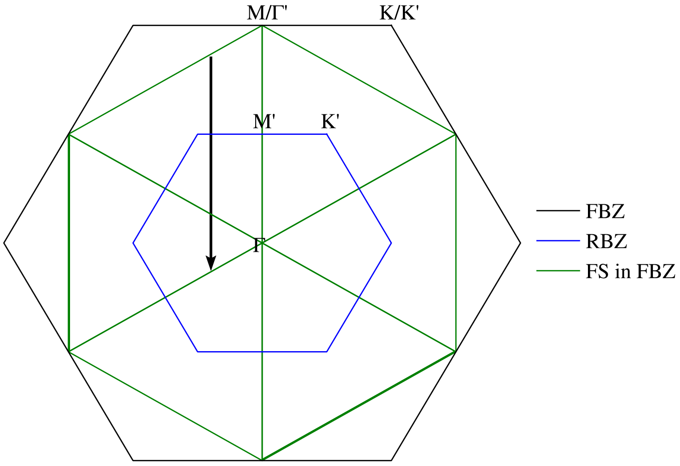

Figure 3.6: The Fermi surface (FS) in the full Brillouin zone. We have indicated the boundaries of the reduced Brillouin zone, as well as marked the different high symmetry points of the full Brillouin zone (reduced Brillouin zone) as the labels with (without) the apostrophe. The arrow indicates how the original contribution to the Fermi surface of the full Brillouin zone is translated into the reduced Brillouin zone.

$2a_0 \times 2a_0$ phase. This means we can rewrite the tight-binding Hamiltonian Eq. (3.10)

$$H_{TB} = \sum_{\mathbf{k}\in\mathrm{RBZ}} \mathbf{C}^{\dagger}_{\mathbf{k}\sigma}(h_{\mathbf{k}} \oplus h_{\mathbf{k}+\mathbf{M}_1} \oplus h_{\mathbf{k}+\mathbf{M}_2} \oplus h_{\mathbf{k}+\mathbf{M}_3})\mathbf{C}_{\mathbf{k}\sigma}, \tag{3.14}$$

where we have defined $\mathbf{C}^{\dagger}_{\mathbf{k}\sigma} = (\mathbf{c}^{\dagger}_{\mathbf{k}\sigma}, \mathbf{c}^{\dagger}_{\mathbf{k}+\mathbf{M}_1\sigma}, \mathbf{c}^{\dagger}_{\mathbf{k}+\mathbf{M}_2\sigma}, \mathbf{c}^{\dagger}_{\mathbf{k}+\mathbf{M}_3\sigma})$. The band structure of the tight-binding Hamiltonian along the high symmetry path in the reduced Brillouin zone and in the full Brillouin zone is plotted in Fig. 3.5. We will use the band structure in Fig. 3.5b as a benchmark to compare ordered states breaking translational symmetry with a $2a_0 \times 2a_0$ phase. The Fermi surface at the van Hove points is plotted in the full Brillouin zone in Fig. 3.6. In the plot we show how the Fermi surface from the first Brillouin zone, when we consider a translational symmetry conserving phase, is translated into the reduced Brillouin zone of a $2a_0 \times 2a_0$ phase. In ARPES experiments the spectral function is measured, which at the Fermi energy is non-zero for the occupied states, i.e. the states contributing to the Fermi surface. When we examine the spectral function for the orders states in Chapter 5, it will be compared to this Fermi surface.

Chapter 4

Mean field theory

A many-body system consists of many particles whose dynamics are influenced by all the other particles. To study such a system on the microscopic level one has to make assumptions about the correlations between the particles. One theoretical framework is mean field theory, which is based on the assumption that the fluctuations $\delta c^\dagger_\mu c_{\mu'} = c^\dagger_\mu c_{\mu'} - \left\langle c^\dagger_\mu c_{\mu'} \right\rangle$ of the operator $c^\dagger_\mu c_{\mu'}$ are small. This means, we can expand the Hamiltonian to first order in the fluctuations obtaining a problem consisting of independent particles, where the effective background potential is defined by the mean fields $\left\langle c^\dagger_\mu c_{\mu'} \right\rangle$. We start by considering the general interaction

$$H = \sum_{\mu\mu'\nu\nu'} V_{\mu\mu'\nu\nu'}\, c^\dagger_\mu c_{\mu'} c^\dagger_\nu c_{\nu'}. \tag{4.1}$$

Since electrons are indistinguishable particles, we have to consider all the possible ways to decouple the interaction, yielding three possible channels: The direct channel, where the interaction is expanded in the fluctuations of the operators of the form $c^\dagger_\mu c_{\mu'}$; the exchange channel, where the interaction is expanded in the fluctuations over an exchange of particles $c^\dagger_\mu c_{\nu'}$; and finally the Cooper channel, where the interaction is expanded in the fluctuations between two creation or two annihilation operators. The Cooper channel is important when considering particle hole symmetric orders like superconductivity, however, as this thesis is concerned with the normal state of AV$_3$Sb$_5$, we will ignore this channel. We now compute the expansions of the interaction and divide the terms from the direct channel, called the Hartree terms, from the terms from the exchange channel, called the Fock terms.

$$\begin{aligned}
V_{\mu\mu'\nu\nu'} c^\dagger_\mu c_{\mu'} c^\dagger_\nu c_{\nu'} &\approx V_{\mu\mu'\nu\nu'} \left(V^{\mathrm{H}}_{\mu\mu'\nu\nu'} - V^{\mathrm{F}}_{\mu\mu'\nu\nu'} \right) \\
V^{\mathrm{H}}_{\mu\mu'\nu\nu'} &= \left\langle c^\dagger_\mu c_{\mu'} \right\rangle c^\dagger_\nu c_{\nu'} + \left\langle c^\dagger_\nu c_{\nu'} \right\rangle c^\dagger_\mu c_{\mu'} \\
V^{\mathrm{F}}_{\mu\mu'\nu\nu'} &= \left\langle c^\dagger_\mu c_{\nu'} \right\rangle c^\dagger_\nu c_{\mu'} + \left\langle c^\dagger_\nu c_{\mu'} \right\rangle c^\dagger_\mu c_{\nu'}.
\end{aligned} \tag{4.2}$$

In the expressions above we have not included the constant terms from the first order expansion. These are added as corrections to the final energy

$$E_{\mathrm{crxn}} = -\left\langle c^\dagger_\mu c_{\mu'} \right\rangle \left\langle c^\dagger_\nu c_{\nu'} \right\rangle + \left\langle c^\dagger_\mu c_{\nu'} \right\rangle \left\langle c^\dagger_\nu c_{\mu'} \right\rangle, \tag{4.3}$$

which will be included in the mean field Hamiltonian when needed, and else kept as separate terms to be calculated later.

To construct the mean field Hamiltonian we need to find the mean fields $\left\langle c_\mu^\dagger c_\nu \right\rangle$. They are defined as the thermal average over the operators $c_\mu^\dagger c_\nu$

$$\left\langle c_\mu^\dagger c_\nu \right\rangle = \frac{\mathrm{Tr}\left[e^{-H_{\mathrm{MF}}/T} c_\mu^\dagger c_\nu\right]}{Z_{\mathrm{MF}}}, \tag{4.4}$$

where Z_{MF} is the partition function defined as $\mathrm{Tr}\left[e^{-H_{\mathrm{MF}}/T}\right]$ and T is the temperature. When using a self-consistency algorithm (see Section 4.3), it will be useful to express the mean fields in terms of the components of the eigenvectors. Defining the eigenbasis of the mean field Hamiltonian $|\psi_n\rangle$, such that $H_{\mathrm{MF}}|\psi_n\rangle = E_n|\psi_n\rangle$ where E_n is the eigenenergy and defining the μ component of the eigenvector $u_n(\mu) = \langle\psi_n|\mu\rangle$, we express the mean fields in terms of the components of the eigenvector

$$\left\langle c_\mu^\dagger c_\nu \right\rangle = \sum_n \left[u_n(\mu)\right]^* u_n(\nu) n_F(E_n), \tag{4.5}$$

where $n_F(E)$ is the Fermi function $n_F(E) = \left[e^{E/T}+1\right]^{-1}$.

4.1 Mean field decoupling of the interaction

We will now consider the particles in the tight-binding model as interacting electrons. We assume the interaction takes the form of an extended Hubbard model, where we introduce an on-site repulsion for electrons on the same lattice site, parameterized by U [42], and a nearest neighbor repulsion, parameterized by V. The interaction strengths will be assumed to be invariant of the lattice site(s), yielding the interaction Hamiltonian H'

$$H' = U\sum_{\mathbf{R}\alpha} \hat{n}_{\mathbf{R}\alpha\uparrow}\hat{n}_{\mathbf{R}\alpha\downarrow} + V\sum_{\substack{\mathbf{R}\alpha\\ \beta>\alpha}}\sum_{\sigma\sigma'}\left(\hat{n}_{\mathbf{R}\alpha\sigma}\hat{n}_{\mathbf{R}\beta\sigma'} + \hat{n}_{\mathbf{R}\alpha\sigma}\hat{n}_{\mathbf{R}-2\mathbf{a}_{\alpha\beta}\beta\sigma'}\right), \tag{4.6}$$

where $n_{\mathbf{R}\alpha\sigma} = c^\dagger_{\mathbf{R}\alpha\sigma}c_{\mathbf{R}\alpha\sigma}$ is the density operator and $\alpha < \beta$ is understood to ensure no double counting takes place, defining $A < B$ etc. Before writing the general mean field we introduce some new notation s. We set $s = +$ ($s = -$) when the two sites α and β are in the same (different) unit cell(s). This allows us to define the lattice vector $\mathbf{R}_s$ of the unit cell with the β site when the α site is in the unit cell at $\mathbf{R}$

$$\mathbf{R}_s \equiv \mathbf{R} + (s-1)\mathbf{a}_{\alpha\beta}. \tag{4.7}$$

With this additional index we can write the most general mean field

$$\Delta^{\alpha\sigma\beta\sigma'}_{\mathbf{R},s} = \left\langle c^\dagger_{\mathbf{R}\alpha\sigma} c_{\mathbf{R}_s\beta\sigma'}\right\rangle. \tag{4.8}$$

The s index is redundant when $\alpha = \beta$, as the only non-zero mean fields with particles on sites with the same sublattice are between particles in the same unit cell. We will interpret the mean fields will in terms of order parameters in Section 4.4.

The interactions are decoupled in terms of the mean fields using the unrestricted Hartree-Fock approximation from Eq. (4.2). We start by decoupling the on-site repulsion, writing the Hartree and Fock terms

$$H_U^{\mathrm{MF}} = U\sum_{\mathbf{R}\alpha}\sum_{\sigma}\left(\Delta^{\alpha\sigma\alpha\sigma}_{\mathbf{R},+}\hat{n}_{\mathbf{R}\alpha\bar{\sigma}} - \Delta^{\alpha\bar{\sigma}\alpha\sigma}_{\mathbf{R},+} c^\dagger_{\mathbf{R}\alpha\sigma}c_{\mathbf{R}\alpha\bar{\sigma}}\right), \tag{4.9}$$

where $\overline{\sigma} =\uparrow (\downarrow)$, when $\sigma =\downarrow (\uparrow)$. The nearest neighbor interaction is similarly decoupled. The decoupling allows us to compress the notation

$$H_V^{\mathrm{MF}} = V \sum_{\substack{\mathbf{R}\alpha \\ \beta\neq\alpha}} \sum_{s\sigma\sigma'} \left(\Delta^{\alpha\sigma\alpha\sigma}_{\mathbf{R},+} \hat{n}_{\mathbf{R}_s\beta\sigma'} - \Delta^{\alpha\sigma\beta\sigma'}_{\mathbf{R},+} c^{\dagger}_{\mathbf{R}_s\beta\sigma'} c_{\mathbf{R}\alpha\sigma} \right). \tag{4.10}$$

The mean field Hamiltonian is found by combining the two mean field decoupled interactions and the tight-binding Hamiltonian from Section 3.2.

$$\begin{aligned} H_{\mathrm{MF}} = \sum_{\mathbf{R}\alpha\sigma} \Bigg\{ & -t \sum_{s,\beta\neq\alpha} c^{\dagger}_{\mathbf{R}\alpha\sigma} c_{\mathbf{R}_s\beta\sigma} + U \left(\Delta^{\alpha\sigma\alpha\sigma}_{\mathbf{R},+} \hat{n}_{\mathbf{R}\alpha\overline{\sigma}} - \Delta^{\alpha\sigma\alpha\overline{\sigma}}_{\mathbf{R},+} c^{\dagger}_{\mathbf{R}\alpha\sigma} c_{\mathbf{R}\alpha\overline{\sigma}} \right) \\ & + V \sum_{\beta\neq\alpha} \sum_{\sigma',s} \left(\Delta^{\alpha\sigma\alpha\sigma}_{\mathbf{R},+} \hat{n}_{\mathbf{R}_s\beta\sigma'} - \Delta^{\alpha\sigma\beta\sigma'}_{\mathbf{R},s} c^{\dagger}_{\mathbf{R}_s\beta\sigma'} c_{\mathbf{R}\alpha\sigma} \right) \Bigg\}, \end{aligned} \tag{4.11}$$

with the correction to the free energy

$$\begin{aligned} E_{\mathrm{crxn}} = & - V \sum_{\substack{\mathbf{R}\alpha \\ \beta>\alpha}} \sum_{\sigma\sigma' s} \left(\Delta^{\alpha\sigma\alpha\sigma}_{\mathbf{R},+} \Delta^{\beta\sigma'\beta\sigma'}_{\mathbf{R}_s,+} - \Delta^{\alpha\sigma\beta\sigma'}_{\mathbf{R},s} \Delta^{\beta\sigma'\alpha\sigma}_{\mathbf{R}_s,s} \right) \\ & - U \sum_{\mathbf{R}\alpha} \left(\Delta^{\alpha\uparrow\alpha\uparrow}_{\mathbf{R},+} \Delta^{\alpha\downarrow\alpha\downarrow}_{\mathbf{R},+} - \Delta^{\alpha\downarrow\alpha\uparrow}_{\mathbf{R},+} \Delta^{\alpha\uparrow\alpha\downarrow}_{\mathbf{R},+} \right). \end{aligned} \tag{4.12}$$

4.2 Mean field Hamiltonian in momentum space basis

We will similarly make a change of basis and consider the interaction in momentum space. To do this we assume translational symmetry breaks in accordance with the nesting vectors presented in Section 3.2, meaning the mean fields has the property

$$\Delta^{\alpha\sigma\beta\varsigma}_{\mathbf{R},s} = \Delta^{\alpha\sigma\beta\varsigma}_{\mathbf{R}+\mathbf{T},s}, \quad \mathbf{T} = 2\mathbf{t}_1 + 2\mathbf{t}_2. \tag{4.13}$$

This property allows the mean fields to either not break translational symmetry, or break translational symmetry in either one lattice direction yielding a $2a_0$ phase or break translational symmetry in both lattice directions yielding a $2a_0 \times 2a_0$ phase.

We transform the mean fields into momentum space by inserting Eq. (3.8) in Eq. (4.8), obtaining

$$\Delta^{\alpha\sigma\beta\sigma'}_{\mathbf{R},s} = \sum_{\mathbf{q}} e^{i\mathbf{q}\cdot\mathbf{R}} \sum_{\mathbf{k}} \frac{e^{i(s-1)(\mathbf{q}+\mathbf{k})\cdot\mathbf{a}_{\alpha\beta}}}{N} \left\langle c^{\dagger}_{\mathbf{k}\alpha\sigma} c_{\mathbf{k}+\mathbf{q}\beta\sigma'} \right\rangle. \tag{4.14}$$

Comparing this with the definition of the Fourier transform, we obtain an expression for the Fourier transform of the mean fields

$$\Delta^{\alpha\sigma\beta\sigma'}_{\mathbf{q},s} = \sum_{\mathbf{k}} \frac{e^{i(s-1)(\mathbf{k}+\mathbf{q})\cdot\mathbf{a}_{\alpha\beta}}}{\sqrt{N}} \left\langle c^{\dagger}_{\mathbf{k}\alpha\sigma} c_{\mathbf{k}+\mathbf{q}\beta\sigma'} \right\rangle. \tag{4.15}$$

We can rewrite the constraint on the system imposed in Eq. (4.13) in terms of the mean fields in the momentum space basis

$$\sum_{\mathbf{q}} e^{i\mathbf{q}\cdot\mathbf{R}} \left(1 - e^{i\mathbf{q}\cdot\mathbf{T}}\right) \Delta^{\alpha\sigma\beta\sigma'}_{\mathbf{q},s} = 0. \tag{4.16}$$

As this has to be true for any lattice vector $\mathbf{R}$, the equation must hold for every term in the sum, meaning, either $\Delta_{\mathbf{q}}$ is zero or $\mathbf{q} \cdot \mathbf{T} = 2\pi n$. This yields four momenta in the first Brillouin zone: $\mathbf{0}$, $\mathbf{M}_1$, $\mathbf{M}_2$ and $\mathbf{M}_3$, where $\Delta_{\mathbf{q}}$ can be non-zero.

We are now ready to construct the mean field Hamiltonian in momentum space, starting by transforming Eq. (4.6), into momentum space

$$H' = \frac{U}{N} \sum_{\mathbf{q}\alpha} \hat{n}_{\mathbf{q}\alpha\uparrow} \hat{n}_{-\mathbf{q}\alpha\downarrow} + \frac{V}{N} \sum_{\substack{\mathbf{q}\alpha, \\ \beta>\alpha}} \sum_{\sigma\sigma'} \left(\hat{n}_{\mathbf{q}\alpha\sigma} \hat{n}_{-\mathbf{q}\beta\sigma'} + \hat{n}_{\mathbf{q}\alpha\sigma} \hat{n}_{-\mathbf{q}\beta\sigma'} e^{2i\mathbf{q}\cdot\mathbf{a}_{\alpha\beta}} \right), \tag{4.17}$$

where $\hat{n}_{\mathbf{q}\alpha\sigma} = \sum_{\mathbf{k}} c^{\dagger}_{\mathbf{k}\alpha\sigma} c_{\mathbf{k}+\mathbf{q}\alpha\sigma}$. Using the general mean field approximation given in Eq. (4.2), we mean field decouple the Hubbard interaction.

$$H_U^{\mathrm{MF}} = \frac{U}{\sqrt{N}} \sum_{\mathbf{kq}\alpha\sigma} \left(\Delta^{\alpha\bar{\sigma}\alpha\bar{\sigma}}_{\mathbf{q},+} c^{\dagger}_{\mathbf{k}\alpha\sigma} c_{\mathbf{k}+\mathbf{q}\alpha\sigma} - \Delta^{\alpha\sigma\alpha\bar{\sigma}}_{\mathbf{q},+} c^{\dagger}_{\mathbf{k}\alpha\bar{\sigma}} c_{\mathbf{k}+\mathbf{q}\alpha\sigma} \right), \tag{4.18}$$

similarly, the nearest neighbor interaction is mean field decoupled

$$\begin{aligned} H_V^{\mathrm{MF}} = \frac{V}{\sqrt{N}} \sum_{\substack{\mathbf{kq}\alpha\sigma\sigma' \\ \beta\neq\alpha}} \Big[& \left(1 + e^{2i\mathbf{q}\cdot\mathbf{a}_{\alpha\beta}}\right) \Delta^{\beta\sigma'\beta\sigma'}_{\mathbf{q},+} c^{\dagger}_{\mathbf{k}\alpha\sigma} c_{\mathbf{k}+\mathbf{q}\alpha\sigma} \\ & - \left(\Delta^{\alpha\sigma\beta\sigma'}_{\mathbf{q},+} + \Delta^{\alpha\sigma\beta\sigma'}_{\mathbf{q},-} e^{2i\mathbf{k}\cdot\mathbf{a}_{\alpha\beta}} \right) c^{\dagger}_{\mathbf{k}\beta\sigma'} c_{\mathbf{k}+\mathbf{q}\alpha\sigma} \Big], \end{aligned} \tag{4.19}$$

with a step by step derivation given in Appendix A.

We can now construct the mean field Hamiltonian in the momentum space basis

$$H_{\mathrm{MF}} = \sum_{\mathbf{k}\sigma} \mathbf{c}^{\dagger}_{\mathbf{k}\sigma} h_{\mathbf{k}} \mathbf{c}_{\mathbf{k}\sigma} + H_U^{\mathrm{MF}} + H_V^{\mathrm{MF}}. \tag{4.20}$$

This Hamiltonian is block diagonal, meaning we can rewrite the Hamiltonian as

$$H_{\mathrm{MF}} = \sum_{\mathbf{k}\in\mathrm{RBZ}} \left(\mathbf{C}^{\dagger}_{\mathbf{k}\uparrow}, \mathbf{C}^{\dagger}_{\mathbf{k}\downarrow} \right) H_{\mathbf{k}} \begin{pmatrix} \mathbf{C}_{\mathbf{k}\uparrow} \\ \mathbf{C}_{\mathbf{k}\downarrow} \end{pmatrix}, \tag{4.21}$$

where $H_{\mathbf{k}}$ is the Hamiltonian for $\mathbf{k}$ in the reduced Brillouin zone, written in the basis $(\mathbf{C}^{\dagger}_{\mathbf{k}\uparrow}, \mathbf{C}^{\dagger}_{\mathbf{k}\downarrow})$. The exact expressions of the interacting part of the Hamiltonian is derived in Appendix A. The correction to the free energy from the on-site repulsion is found

$$E^U_{\mathrm{crxn}} = -U \sum_{\mathbf{q}\alpha} \left(\Delta^{\alpha\uparrow\alpha\uparrow}_{\mathbf{q},+} \Delta^{\alpha\downarrow\alpha\downarrow}_{\mathbf{q},+} - \Delta^{\alpha\downarrow\alpha\uparrow}_{\mathbf{q},+} \Delta^{\alpha\uparrow\alpha\downarrow}_{\mathbf{q},+} \right), \tag{4.22}$$

and the correction to the free energy from the nearest neighbor interaction is

$$E^V_{\mathrm{crxn}} = -V \sum_{\substack{\mathbf{q}\sigma\sigma' \\ \alpha,\beta>\alpha}} \sum_{s} \left[e^{i(1-s)\mathbf{q}\cdot\mathbf{a}_{\alpha\beta}} \Delta^{\beta\sigma'\beta\sigma'}_{\mathbf{q},+} \Delta^{\alpha\sigma\alpha\sigma}_{\mathbf{q},+} - e^{i(1-s)\mathbf{q}\cdot\mathbf{a}_{\alpha\beta}} \Delta^{\alpha\sigma\beta\sigma'}_{\mathbf{q},s} \Delta^{\beta\sigma'\alpha\sigma}_{\mathbf{q},s} \right]. \tag{4.23}$$

The expressions are also derived in Appendix A.

4.3 Self-consistency algorithm

To solve the mean field Hamiltonian numerically, we implement a self-consistency algorithm. The foundation of this method, lies in the fact that a self-consistent solution minimizes the free energy. We follow the proof given in Ref. [43], starting with the mean field Hamiltonian, where the mean fields put in to the Hamiltonian are defined as $\Delta_{\mu\nu}$, and minimize the free energy $F = -T\ln(Z_{\text{MF}})$, with the respect to a specific mean field $\Delta_{\kappa\lambda}$

$$\begin{aligned} 0 = \frac{\delta F}{\delta \Delta_{\kappa\lambda}} &= \frac{-T}{Z_{\text{MF}}} \frac{\delta}{\delta \Delta_{\kappa\lambda}} \operatorname{Tr}\left[e^{-H_{\text{MF}}/T}\right] \\ &= \sum_{\nu\nu'} \left(V_{\kappa\lambda\nu\nu'} + V_{\nu\nu'\kappa\lambda} - V_{\kappa\nu'\nu\lambda} - V_{\nu\lambda\kappa\nu'}\right)\left(\left\langle c_{\nu}^{\dagger} c_{\nu}\right\rangle - \Delta_{\nu\nu'}\right). \end{aligned} \tag{4.24}$$

As this has to be true for any pair (κ, λ), we obtain the self-consistency condition $\left\langle c_{\nu}^{\dagger} c_{\nu}\right\rangle = \Delta_{\nu\nu'}$ for all pairs of (ν, ν'), which means that the mean fields used in the Hamiltonian are equal to the mean fields calculated from the eigenstates of the Hamiltonian.

We will consider the system in the grand canonical ensemble, which means only the average particle density n_{target} is known, thus introducing the chemical potential μ, such that $H \to H - \mu$. By choosing different target densities, we can examine the system at different points in the band structure.

We now give a description of the steps of a self-consistent algorithm. For a state to be a solution to the algorithm, we will require that the mean fields fulfills the self-consistency condition and that the system has the desired average density n_{target}. As the particle density is controlled both by the mean fields and the chemical potential, we also update the value of the chemical potential. We will start from an initial configuration of the mean fields and an initial chemical potential, and follow the steps

1. Calculate the correction to the energy E_{crxn} from the input mean field Δ_{in}.
2. Calculate the average density $\overline{n}$ from the mean fields, see Eq. (4.25)
3. Calculate the mean field Hamiltonian from the input mean fields, and solve the eigenvalue problem $H_{\text{MF}}\left|\psi_n\right\rangle = E_n\left|\psi_n\right\rangle$.
4. Calculate the new mean fields Δ_{new} using the states obtained from the eigenvalue problem and the chemical potential μ_{in}, see Eq. (4.5).
5. Check if all mean fields have converged, which numerically means the difference between the new and input mean fields is smaller than a cut-off value ϵ, and if the system has the desired total density, i.e. $|\overline{n} - n_{\text{target}}| < \epsilon_n$, where ϵ_n is the cut-off value for the densities.
   (a) If the system has converged, the solution are the current mean fields.
   (b) If the system has not converged, but the algorithm has gone through a fixed number of iterations (in this thesis 10,000), the algorithm is stopped, and the system has not converged.
   (c) Else update the mean fields and the chemical potential with weights w_Δ and w_μ, such that the updated mean fields are $\Delta_{\text{up}} = (1 - w_\Delta)\Delta_{\text{in}} + w_\Delta \Delta_{\text{new}}$, and the updated chemical potential is $\mu_{\text{up}} = \mu_{\text{in}} + w_\mu(n_{\text{target}} - \overline{n})$, where μ_{in} is the chemical potential used at the start of the iteration. The algorithm is then repeated with the updated mean fields and chemical potential as inputs.

Ideally the result of the algorithm would not depend on the input parameters and always find the global energy minimum, thus we could keep the cut-off values at essentially 0. Numerical precision and the constraints on the running time of the algorithm forces a lower bound on the cut-off values. In this thesis we set $\epsilon = \epsilon_n = 10^{-8}$.

The weights are another layer of parameters influencing the solution of the algorithm. If the weights are too small the algorithm converges slowly, such that a potentially ordered state is missed due to the threshold of 10,000 iterations. On the contrary, when weights are too large, energy minima can be missed by the algorithm. Furthermore, one risks that the algorithm runs in a loop between different states above the convergence threshold, and the algorithm never yields a solution. In this thesis we use $w_\Delta = w_\mu = \frac{1}{5}$, and on rare occasions the change the weights, to test if the different input parameters yield a different solution with a lower free energy.

The input parameter with the largest impact on results are the original mean fields put in to the Hamiltonian in the first iteration. Some energy minima are narrow, i.e. the solutions are rarely obtained if the original mean fields are not close to the solution. Hence, if the global energy minimum cannot be found with the initialization used in the algorithm the self-consistent solution is not the actual ordered phase, instead a meta stable state. To mitigate the issue we will initialize with different configurations of the mean fields, and the solution with the lowest free energy, i.e. the ground state, is the ordered state at this point in (U, V)-space. However, the risk of missing the actual global energy minimum can never be avoided.

In Eqs. (4.11) and (4.21) we have expressed the Hamiltonian in the real space basis and momentum space basis, respectively. While the Hamiltonian can be written more intuitively in the real space basis, it comes with some computational problems. First, the time to solve the eigenvalue problem grows cubic with the system size, meaning larger systems are not realistically computable. Furthermore, with larger systems domains are likely to occur yielding an inconclusive solution. Conversely, smaller systems are prone to finite size effects, which also impact the quality of the results. Finally, due to periodic boundary conditions the mean fields can only break translational symmetry in specific ways, allowed by the boundary conditions.

In the momentum space basis, we limit the possibilities of how the translational symmetry can be broken when we imposed the constraint Eq. (4.13), however, since the Hamiltonian is block diagonal in the momentum space basis, the time to solve the eigenvalue problem grows linear with system size, making larger systems more computationally feasible. Furthermore, due to the assumptions on translational symmetry breaking, the states cannot form domains.

4.4 Order parameters

The mean fields can be combined into order parameters, which quantify if the mean field state has a particular order. We can define the phases of the system from the values of the order parameters, especially how the order parameters differ from their values in the disordered state. The expressions of the order parameters is written in real space basis, as the physical interpretation of the parameters is more clearly seen in this basis. The order parameters in momentum space basis can be obtained by Fourier transformation. We define the vector $\boldsymbol{\phi}^\dagger_{\mathbf{R}\alpha} = (c^\dagger_{\mathbf{R}\alpha\uparrow}, c^\dagger_{\mathbf{R}\alpha\downarrow})$, to more elegantly define the order parameters.

Using this notation, the density order parameter is defined as

$$n_{\mathbf{R}\alpha} \equiv \frac{1}{2}\Re\left\langle \boldsymbol{\phi}^{\dagger}_{\mathbf{R}\alpha}\sigma_0\boldsymbol{\phi}_{\mathbf{R}\alpha}\right\rangle, \tag{4.25}$$

where σ_0 is the identity operator in spin space. This order parameter represents the local electron density on site α in the unit cell at $\mathbf{R}$, divided by the number of spin states. Next we consider the spin density order parameter,

$$s^{i}_{\mathbf{R}\alpha} \equiv \frac{1}{2}\Re\left\langle \boldsymbol{\phi}^{\dagger}_{\mathbf{R}\alpha}\sigma_i\boldsymbol{\phi}_{\mathbf{R}\alpha}\right\rangle, \tag{4.26}$$

where σ_i is the Pauli-i matrix.

To define the bond order parameter properly, we consider the term in the mean field Hamiltonian (Eq. (4.11)) with the operators $c^{\dagger}_{\mathbf{R}_s\beta\sigma'}c_{\mathbf{R}\alpha\sigma}$. The effective hopping strength between the two sites is the coefficient of this term $t + V\Delta^{\alpha\sigma\beta\sigma'}_{\mathbf{R}s}$, meaning the real part of the $V\Delta^{\alpha\sigma\beta\sigma'}_{\mathbf{R}s}$ modifies the hopping strength t. By defining the bond order parameter as

$$\eta_{\mathbf{R}s\alpha\beta} \equiv \frac{1}{2}\Re\left\langle \boldsymbol{\phi}^{\dagger}_{\mathbf{R}\alpha}\sigma_0\boldsymbol{\phi}_{\mathbf{R}_s\beta}\right\rangle, \tag{4.27}$$

we can measure how easily electrons on sites α and β in the unit cells at respectively $\mathbf{R}$ and $\mathbf{R}_s$ can hop to the other site. A positive value of the bond order parameter, means the effective hopping strength is larger than the disordered state, translating into a stronger bond between the two sites. We similarly define the spin bond order parameter

$$\chi^{i}_{\mathbf{R}s\alpha\beta} \equiv \frac{1}{2}\Re\left\langle \boldsymbol{\phi}^{\dagger}_{\mathbf{R}\alpha}\sigma_i\boldsymbol{\phi}_{\mathbf{R}_s\beta}\right\rangle, \tag{4.28}$$

which measures if one spin direction can hop more easily between sites α and β in the unit cells at $\mathbf{R}$ and $\mathbf{R}_s$ than the opposite spin direction.

We will derive the current density order parameter from the continuity equation, considering the site α in the unit cell with lattice vector $\mathbf{R}$

$$\sum_{\beta\neq\alpha,s} \hat{\jmath}_{\mathbf{R}s\alpha\beta} = -\frac{\partial \hat{n}_{\mathbf{R}\alpha}}{\partial t}, \tag{4.29}$$

where $\hat{\jmath}_{\mathbf{R}s\alpha\beta}$ is the current operator for the current flowing from site α to site β in the unit cells at $\mathbf{R}$ and $\mathbf{R}_s$ respectively, and $\hat{n}_{\mathbf{R}\alpha} = (\hat{n}_{\mathbf{R}\alpha\uparrow} + \hat{n}_{\mathbf{R}\alpha\downarrow})/2$. From Heisenberg's equation of motion we find the temporal derivative of the density operator

$$\sum_{\beta\neq\alpha,s} \hat{\jmath}_{\mathbf{R}s\alpha\beta} = i[\hat{n}_{\mathbf{R}\alpha}, H]. \tag{4.30}$$

As the interactions are density-density interactions, they will commute with the density operator, hence, we only consider the tight-binding contribution to the Hamiltonian. Furthermore, all terms where $c_{\mathbf{R}\alpha\sigma}$ and its conjugate are absent will also commute with the density operator of the site examined, leaving the remaining terms of the Hamiltonian

$$\sum_{\beta\neq\alpha,s} \hat{\jmath}_{\mathbf{R}s\alpha\beta} = \frac{-it}{2}\sum_{\sigma}\sum_{\beta\neq\alpha,s}\left[c^{\dagger}_{\mathbf{R}\alpha\sigma}c_{\mathbf{R}\alpha\sigma}, c^{\dagger}_{\mathbf{R}\alpha\sigma}c_{\mathbf{R}_s\beta\sigma} + c^{\dagger}_{\mathbf{R}_s\beta\sigma}c_{\mathbf{R}\alpha\sigma}\right]. \tag{4.31}$$

Using anti-commutator relations, we can obtain the general result for the commutation relation for two fermionic creation and annihilation operators c_a and c_b: $\left[c^{\dagger}_a c_a, c^{\dagger}_b c_a\right] =$

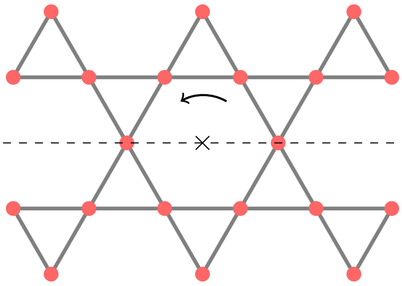

Figure 4.1: Schematic drawing of the kagome lattice. The generating symmetry operations are indicated, with the arrow representing the C_6 rotation around the axis marked by × and the dashed line indicating the median of the mirror plane.

$-c_b^\dagger c_a$ and $\left[c_a^\dagger c_a, c_a^\dagger c_b\right] = c_a^\dagger c_b$. Furthermore, as this has to be true for any pair site of the lattice, we can equate the parts being summed over

$$\hat{\jmath}_{\mathbf{R}s\alpha\beta} = \frac{-it}{2} \sum_\sigma \left(c^\dagger_{\mathbf{R}\alpha\sigma} c_{\mathbf{R}_s\beta\sigma} - c^\dagger_{\mathbf{R}_s\beta\sigma} c_{\mathbf{R}\alpha\sigma} \right). \tag{4.32}$$

Taking the mean field average of this operator we find the current order parameter

$$j_{\mathbf{R}s\alpha\beta} \equiv \Im \left\langle \boldsymbol{\phi}^\dagger_{\mathbf{R}\alpha} \sigma_0 \boldsymbol{\phi}_{\mathbf{R}_s\beta} \right\rangle . \tag{4.33}$$

Similarly, we can define the spin current order parameter

$$\vartheta^i_{\mathbf{R}s\alpha\beta} \equiv \Im \left\langle \boldsymbol{\phi}^\dagger_{\mathbf{R}\alpha} \sigma_i \boldsymbol{\phi}_{\mathbf{R}_s\beta} \right\rangle , \tag{4.34}$$

which is non-zero if the direction of the current is opposite for particles of opposite spin.

4.5 Candidate phases

In this section, we will introduce the phases either found in the phase diagrams, or phases that have previously been reported to exist in the kagome lattice at the upper or lower van Hove point in Refs. [6, 7]. We will also discuss what symmetries the phases break. The generating symmetry operations of the point group D_6 are schematically drawn on a section of the kagome lattice in disordered state in Fig. 4.1

When grouping different states together into a single phases we have chosen to focus on what order parameter is broken in the system. Further subdivision has focused on whether translational symmetry has been broken. This makes some phases cover a wide range of different possibilities especially with regard to rotational symmetry. This is done, as we are primarily interested in the translational symmetry breaking phases relevant to AV_3Sb_5. The candidate phases are summarized in Table 4.1, with a list of the symmetries of the phase.

Disordered

The disordered phase is, where the density is the same for all sites, all bonds have equal strengths and where the spin density, spin bond, current and spin current order parameters are zero everywhere in the system.

Phase	T	C_6	σ	$\mathcal{T}$	Phase	T	C_6	σ	$\mathcal{T}$
Disordered	O	C_6	O	O	CBO	(X)	(X)	(X)	O
UCFM	O	(C_2)	(X)	X	TrH	X	C_6	O	O
FM	O	C_6	O	X	SoD	X	C_6	O	O
SDW	X	(X)	(X)	X	SBO	(X)	(X)	(X)	X
CDW	X	(X)	(X)	O	iCDW	(X)	(X)	(X)	X
UC CDW	O	C_2	(X)	O	iSDW	(X)	(X)	(X)	O

Table 4.1: An overview of the different phases, and whether they break translational symmetry T, six-fold rotational symmetry C_6, mirror symmetry σ or time reversal symmetry $\mathcal{T}$. O indicates the symmetry is conserved; X indicates the symmetry is broken; C_n indicates the order has n-fold rotational symmetry, and (X) indicates the symmetry can be broken.

Unit-cell ferromagnet (UCFM)

A unit-cell ferromagnet is a phase, where the magnetic moments have the same distribution in all unit cells. This phase breaks time reversal symmetry, and can reduce the point group to C_2 i.e. only conserve two-fold rotational symmetry of the symmetries of D_6. We have schematically drawn to variations of the UCFM in Figs. 4.2a and 4.2b. The first has a combined magnetic moment of the unit cell, and the spins of the different sites do not lie in the same plane or have the same magnitude. This phase has the point group C_2. The latter has no overall magnetic moment in the unit cell, the spins have the same magnitude and lie in the same plane. In effect, this phase is a compromise to the magnetic frustration of the Ising spin model on the kagome lattice discussed in Chapter 1. This variation has the D_6 point group.

Ferromagnet (FM)

A ferromagnet is a phase, where the magnetic moment of all sites are aligned, have the same non-zero magnitude. It is thus a subcategory of the UCFM. An example is schematically drawn in Fig. 4.2c. This phase breaks time reversal symmetry, but conserves the symmetries of the point group and translational symmetries.

Spin density wave (SDW)

We will use the term spin density wave for a generic phase, where the distribution of the magnetic moments enlarge the unit-cell, thus breaking translational symmetry. The spin bond order parameter can be non-zero in this phase as well, as the uneven distribution of magnetic moments across the system makes hopping strengths of certain spins likely to be larger than others. All the symmetries of the point group can be broken, and time reversal symmetry is broken due to the non-zero spin order.

Charge density wave (CDW)

A charge density wave refers to phases where the distribution of charges breaks the translational symmetry. The bond order parameter can be non-zero for a similar reason as the spin bond order could be non-zero for the SDW. This phase does not break time reversal symmetry, and the all the symmetries of the D_6 point group can be broken.

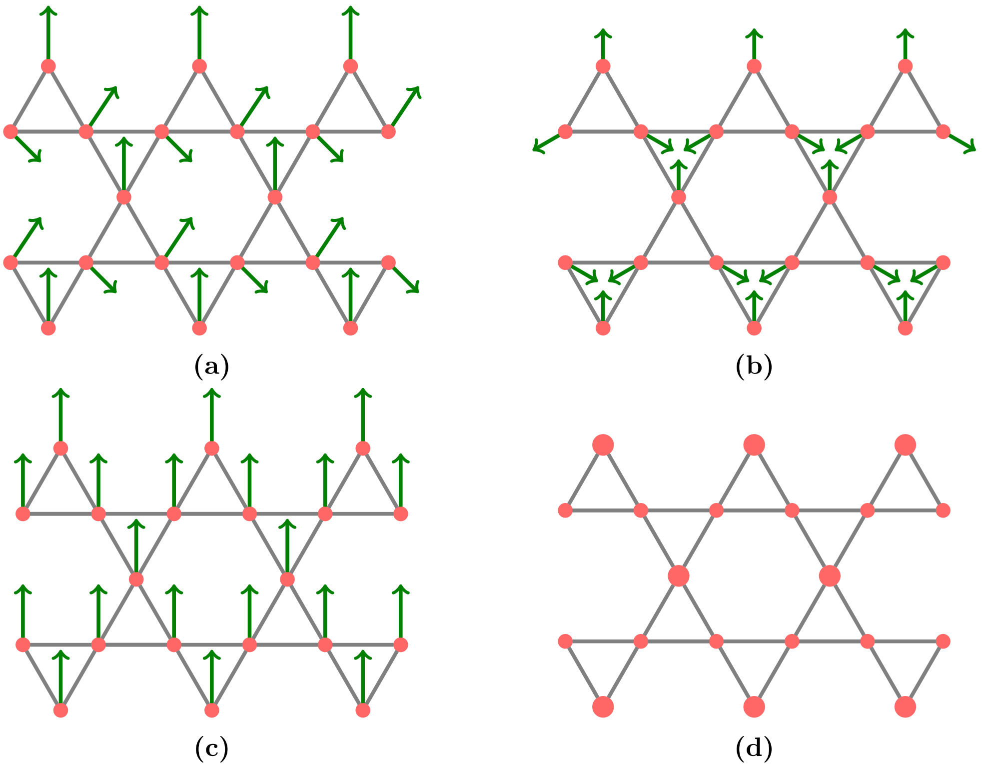
(a)

(b)

(c)

(d)

Figure 4.2: Schematic drawings exemplifying **(a)**, **(b)** UCFM, **(c)** FM, and **(d)** UC CDW. The size of the red dots represents the charge accumulation on the site, and the green arrows represents the directions of the spin of the site. The example drawing in **(a)** do not have all spins in the same plane, and has a combined magnetic moment of the unit cell, **(b)** has no overall magnetic moment.

Unit-cell charge density wave (UC CDW)

A unit-cell charge density wave distributes the charges unevenly inside the unit cell, where all unit cells have the same distribution. This phase conserves time reversal symmetry and translational symmetry, but it reduces the six-fold rotational symmetry to a two-fold rotational symmetry, and it can break the mirror symmetry. An example of a UC CDW, which conserves the mirror symmetry is schematically drawn in Fig. 4.2d.

Charge bond order (CBO)

For charge bond ordered phases the bonds between sites are not of equal strengths, but the charges remain evenly distributed throughout the system. This phase does not break time reversal symmetry, and can break any combination of translational, rotational symmetry and mirror symmetry, but have to break at least one of them.

Tri-Hexagonal (TrH) and Star-of-David (SoD)

These two phases are examples of CBOs, and are schematically drawn in Fig. 2.7. They have been separated from the other CBOs, as these phases have the same modulation of the bond order parameter as the proposed candidates for the charge bond order in AV_3Sb_5 [28]. The phases break translational symmetry, yielding a new unit cell of size $2a_0 \times 2a_0$, and the phases has the same point group as the disordered state.

Spin bond order (SBO)

With a spin bond ordered phase we mean a phase with a non-zero spin bond order parameter. SBO breaks time reversal symmetry, and this phase can break any combination of translational, rotational symmetry and mirror symmetry.

Imaginary charge density wave (iCDW)

Phases with a non-zero current order parameter are imaginary charge density waves. These phases break time reversal symmetry and can break translational and any symmetry of the point group of the disordered state. Two examples of iCDWs are schematically drawn in Fig. 2.10, which conserve the rotational symmetry, one conserves translational symmetry and both break mirror symmetry. The ordered states match the candidates to the loop current phase proposed in Refs. [17, 29].

Imaginary spin density wave (iSDW)

Similarly to iCDW, an imaginary spin density wave is a phase with a non-zero spin current. An imaginary spin density wave does not break time reversal symmetry, as particles of opposite spin has the opposite momentum, but it can break translational symmetry, rotational symmetry.

Chapter 5

Results

In this section we present the results of the self-consistency algorithm from Section 4.3, and we examine the most interesting phases with regard to the newly discovered kagome metals more closely.

To examine the orders, we plot the reconstructed band structure of the ordered phase and compare it to the band structure of the non-interacting system in Fig. 3.5b. If the band structure is heavily reconstructed around the Fermi energy, i.e. a large gap has opened around the Fermi energy or the overall shape of the band structure has changed significantly, the electronic states are correlated to such a degree that the Hartree-Fock approximation is no longer valid, and thus the phase obtained is not describing the physical system. We can furthermore calculate the spectral function at the Fermi energy over the full Brillouin zone. Experiments like ARPES measures the spectral weight at the Fermi energy, and this thus yields a prediction of experimental results.

To discuss the obtained phase diagrams at the different points in the band structure, we compare the results of the self-consistency algorithm with two previous studies: A study using the singular-modal functional renormalization group (SMFRG) method (see ref. [6]) and a functional renormalization group (FRG) study (see Ref. [7]). Both methods are based on renormalization group theory, which only works in the disordered state. When the system enters the ordered state a divergence in the respective susceptibility stops the analysis. This have two important consequences: The method cannot reveal if any of the symmetries of the point group are broken, and it cannot find coexisting orders. A different study using Jastrow-Slater wave-functions has recently been published (see Ref. [23]), however, as the results from the study matches poorly with the results obtained here and in the SMFRG and FRG studies, we will not compare our results to this study.

In the following sections we present the result of the self-consistency algorithm at different target densities. For all phase diagrams we consider a system of 12 unit cells in both lattice directions, yielding 432 sites for the real space basis and 36 momenta in the reduced Brillouin zone. We will consider the system at a temperature of $0.01t$ unless otherwise specified.

5.1 At the upper van Hove point

We first study the upper van Hove point, where $n_{\text{target}} = 5/12$. At this filling the algorithm was studied considering the Hmiltonian in both the real space basis and momentum space basis. The algorithm was initialized with the random, Tri-Hexagonal and a Star-of-David

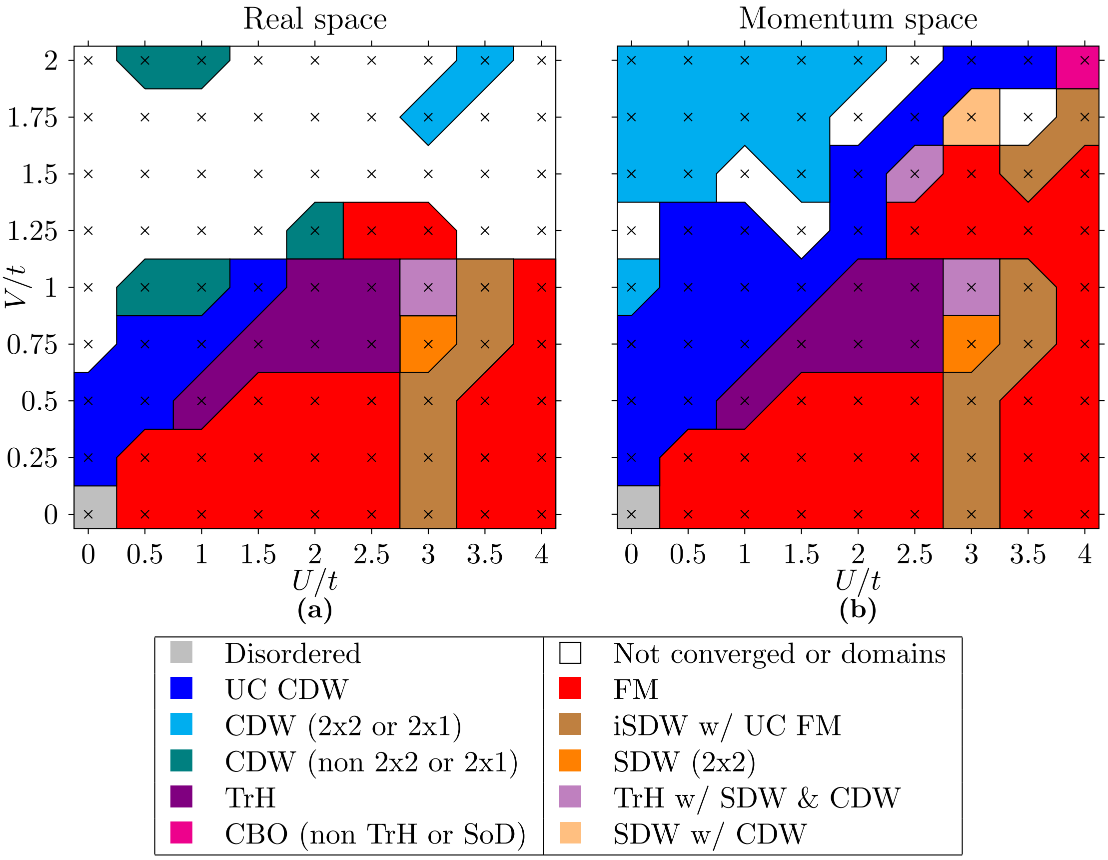

(a) **(b)**

Figure 5.1: Phase diagrams at the van Hove point where $n_{\text{target}} = 5/12$ in (U, V)-space using the **(a)** momentum space and **(b)** real space basis of the Hamiltonian in the self-consistency algorithm. The × symbol marks the points in (U, V)-space tested in the algorithm, and the color codes of the phases are indicated in the table below. Both variations of the algorithm were initialized with the random, Tri-Hexagonal and Star-of-David configurations, and the momentum space variation was further initialized with the coexisting Tri-Hexagonal and FM and two coexisting Tri-Hexagonal and iCDW configurations.

configurations in both bases. The algorithm was further initialized with a coexisting Tri-Hexagonal and FM phase and two coexisting Tri-Hexagonal and iCDW phases when the Hamiltonian was written in the momentum space basis. The iCDW configurations, which the system was initialized with, are the same as the proposed iCDWs schematically drawn in Fig. 2.10. The phase diagrams obtained form the self-consistency algorithm are shown in Fig. 5.1.

The two phase diagrams yields similar results, when the algorithm using the Hamiltonian in the real space basis converges to a phase the momentum space code cannot find (i.e. a modulation containing more than two unit cells in either lattice direction) or does not converge.

The phases of most interest to us are the phases containing the Tri-Hexagonal bond order. We see a large region, covering several of the tested points in (U, V)-space with this bond configuration around the point $(U, V) = (2t, 0.75t)$. This phase is only found when initializing with the Tri-Hexagonal configuration, meaning the minimum in the free energy might be narrow i.e. the algorithm only converges to this order if the initial mean

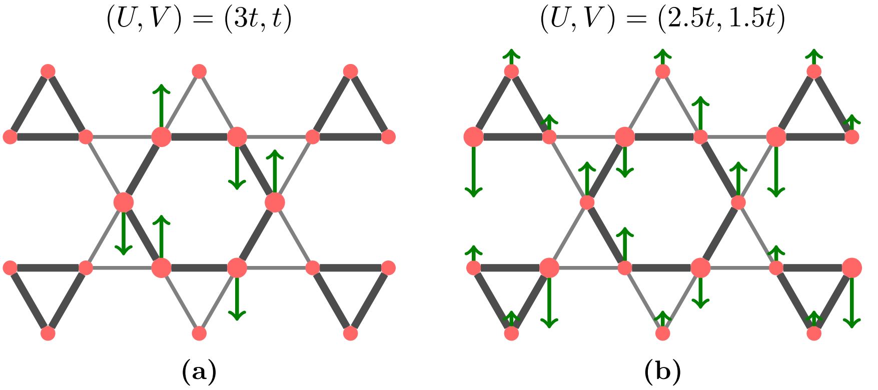

Figure 5.2: The coexisting Tri-Hexagonal and SDW found when $U = 3t$, $V = 1t$.

fields have a similar configuration. When initializing with the Star-of-David configuration, the algorithm converges to a Star-of-David; however, this state has a higher free energy, eg. for $U = 1.5t$ and $V = 0.75t$, $E_{\mathrm{SoD}} - E_{\mathrm{TrH}} \approx 0.005t$. We also note that previous studies have only found the Tri-Hexagonal phase when including phonons [23], where we have here found that the phase can be driven solely by the nesting effects associated with the electronic states.

Furthermore, at the two points $(3t, t)$ and $(2.5t, 1.5t)$ in (U, V)-space, the self-consistent solution is a coexisting Tri-Hexagonal, CDW and SDW phase. The order at $(3t, t)$, is found when initializing with a Tri-Hexagonal configuration of the mean fields, thus the bare Tri-Hexagonal order is not likely to be a self-consistent solution at this point. The two orders are schematically drawn in Fig. 5.2. As can be seen the order state found at $(2.5t, 1.5t)$ breaks translational symmetry, time reversal symmetry and the six-fold rotational symmetry. Only the two-fold rotational symmetry and mirror symmetry are conserved yielding the point group D_2. Conversely, the ordered state found at $(3t, t)$ conserves all the symmetries of the D_6 point group, intriguingly this means we have found an order, which has the same symmetries expected as the kagome metals, in the charge ordered state.

Comparing the remaining phase diagram to the previous renormalization group studies, we see some overlap between our results. The large ferromagnetic phase when $U \geq 3V$, matches well with both studies, however the SMFRG analysis only finds it for $U < 2.5t$. The coexisting iSDW and UCFM has the spin configuration seen in Fig. 4.2b, which is similar to the anti-ferromagnetic phase found in the SMFRG analysis at $U \approx 2.5t$ and $V < 0.5t$. The exact location of the phase in (U, V)-space, and how large V can be when seeing this phase differs between the two studies. The FRG study does not find any CDW phases for the interaction strengths we are considering; however, the UC CDW phase found for $U, V < 0.5t$ in the SMFRG study, matches well with the UC CDW phase found here. The phase found using mean field theory covers a larger portion of (U, V)-space; however, in large parts of this region the SMFRG study finds superconducting phases, which our analysis cannot obtain. Furthermore, where the SMFRG study finds UC CDW around $(U, V) = (0.5t, 2t)$, we find a translational symmetry breaking CDW. Finally, over a large region in (U, V)-space the SMFRG method finds a translational symmetry breaking CBO, including the regions where we find a Tri-Hexagonal phase. While the SMFRG study cannot tell us if the Tri-Hexagonal order is the ground state, it does match well with our result.

We will inspect the Tri-Hexagonal order more closely, as it is a proposed candidate for the

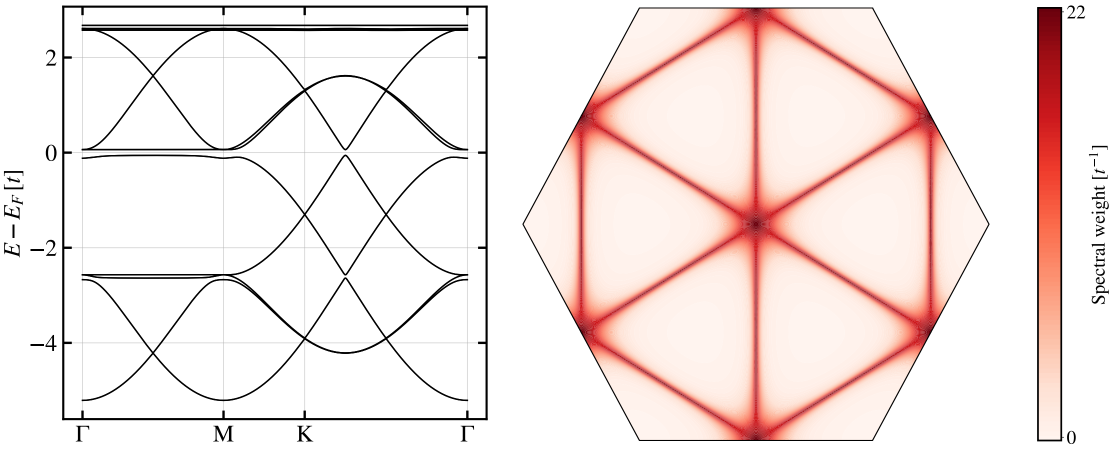

(a) **(b)**

Figure 5.3: **(a)** The reconstructed band structure of the Tri-Hexagonal phase taken along the high symmetry path of the full Brillouin zone. **(b)** The spectral function in the first Brillouin zone for the Tri-Hexagonal phase at the Fermi energy. A weak response is seen at the Fermi surface when the material is not in an ordered phase. The values of the mean fields are taken for $(U,V)=(2t,t)$

charge order in AV_3Sb_5. The reconstructed band structure is plotted in Fig. 5.3a. We see a gap opening at the Fermi energy, which can be explained by the ordered state lifting of a degeneracy. This change in the band structure further means the state is band insulating as no states can be excited with an infinitesimal higher energy at the Fermi level. As the band structure has not been heavily reconstructed, we can conclude that the Hartree-Fock approximation is a good approximation at the examined interaction strength. We furthermore plot the spectral function in Fig. 5.3b. We see a weak response compared to Fig. 5.9b, as can be seen on the intensity scales. This is caused by the gap opening at the Fermi energy.

We do a similar investigation of the coexisting Tri-Hexagonal, SDW and CDW, since it breaks the symmetries which are seen broken in the kagome metals. In Fig. 5.4a we plot the reconstructed band structure of the order state. The band structure has the same overall structure as the Tri-Hexagonal phase seen in Fig. 5.3a, with a similar gap at the Fermi energy. Furthermore, the plot of the spectral function in Fig. 5.3b, where a weak response is seen at the Fermi surface of the non-interacting Hamiltonian.

The mean fields calculations so far have ensured that the on-site part and the hopping part of the nearest neighbor interaction are the same. This implicit assumption is not necessarily true, so we allow for the two contributions to the Hamiltonian to be characterized by different strengths, meaning the mean field decoupled nearest neighbor interaction in real space is

$$H_V=\sum_{\beta\neq\alpha}\sum_{\sigma\sigma' s}\left(V\Delta^{\alpha\sigma\alpha\sigma}_{\mathbf{R},+}n_{\mathbf{R}_s\beta\sigma'}-V'\Delta^{\alpha\sigma\beta\sigma'}_{\mathbf{R},s}c^{\dagger}_{\mathbf{R}_s\beta\sigma'}c_{\mathbf{R}\alpha\sigma}\right). \tag{5.1}$$

With the new interaction, we can again follow the self-consistency algorithm to obtain the most energetically favored phases. We choose three different values of U: 0, $2t$ and $3.5t$. For these values we can test whether a bond ordering regime exist for low magnetic strengths, how the Tri-Hexagonal phase found when $V=V'$ behaves when allowing for $V\neq V'$, and finally, this allows us to see if the unrestricted Hartree-Fock analysis supports

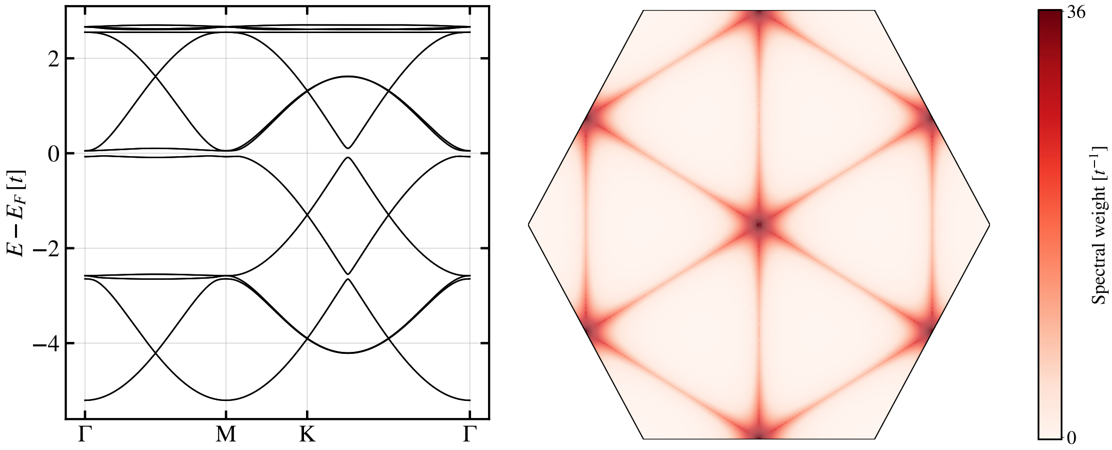

(a) **(b)**

Figure 5.4: **(a)** The reconstructed band structure of the coexisting Tri-Hexagonal, SDW and CDW phase taken along the high symmetry path of the full Brillouin zone. **(b)** The spectral function in the first Brillouin zone for the coexisting Tri-Hexagonal, SDW and CDW phase at the Fermi energy. A weak response is seen at the Fermi surface of the non-interacting Hamiltonian. The values of the mean fields are taken for $(U, V) = (3t, t)$

the findings in Ref. [6], where a CBO was found for $U = 3.5t$. The three phase diagrams were obtained in the momentum space basis, and all points were initialized with random, Tri-Hexagonal and Star-of-David configurations. They are shown in Fig. 5.5.

We will again focus on the phases most interesting for the new kagome metals. We see a bond ordering regime in the phase diagram where $U = 0$. A bond ordering phase is expected here as modulations in density and spin are limited by the small values of U and V compared to V'. We furthermore find a bond ordering regime for $U = 2t$ when $V' \geq 0.75t$ and $V \leq t$. This phase is an extension of the Tri-Hexagonal phase found in Fig. 5.1. The parts of (V, V')-space where $V' > V$ are expected to favor bond ordered phase, due to the larger impact of the bond order parameter in the Hamiltonian and in the correction to the total energy, however when $(V, V') = (t, 0.75t)$ the algorithm still converges to a Tri-Hexagonal state, meaning the phase is robust against changes to the interaction strengths.

Finally, we consider the phase diagram for $U = 3.5$. Our results show a CBO phase when $V' \approx 2t$ and $V \leq t$, however this phase is not of the same form as the Tri-Hexagonal or the Star-of-David, instead the ordered states break rotational symmetry. The rest of the phase diagram is dominated by magnetic phase, with other coexisting order. This result does not match the finding of the SMFRG study well.

5.2 Above the upper van Hove point

As discussed in Section 2.2, AV_3Sb_5 has van Hove points below the Fermi energy. Hence, we want to examine how stable the phases obtained for the upper van Hove points are against a small change in average density of the system. We will here consider the target density $n_{\text{target}} = 5/12 + 0.02$. The Fermi surface at the appropriate chemical potential is shown in Fig. 5.6 in the full Brillouin zone. The corners of the regular hexagon has been rounded off. Naively one would assume the nesting effects would be suppressed compared to $n_{\text{target}} = 5/12$, as fewer momenta $\mathbf{k}$ satisfy the nesting conditions for any particu-

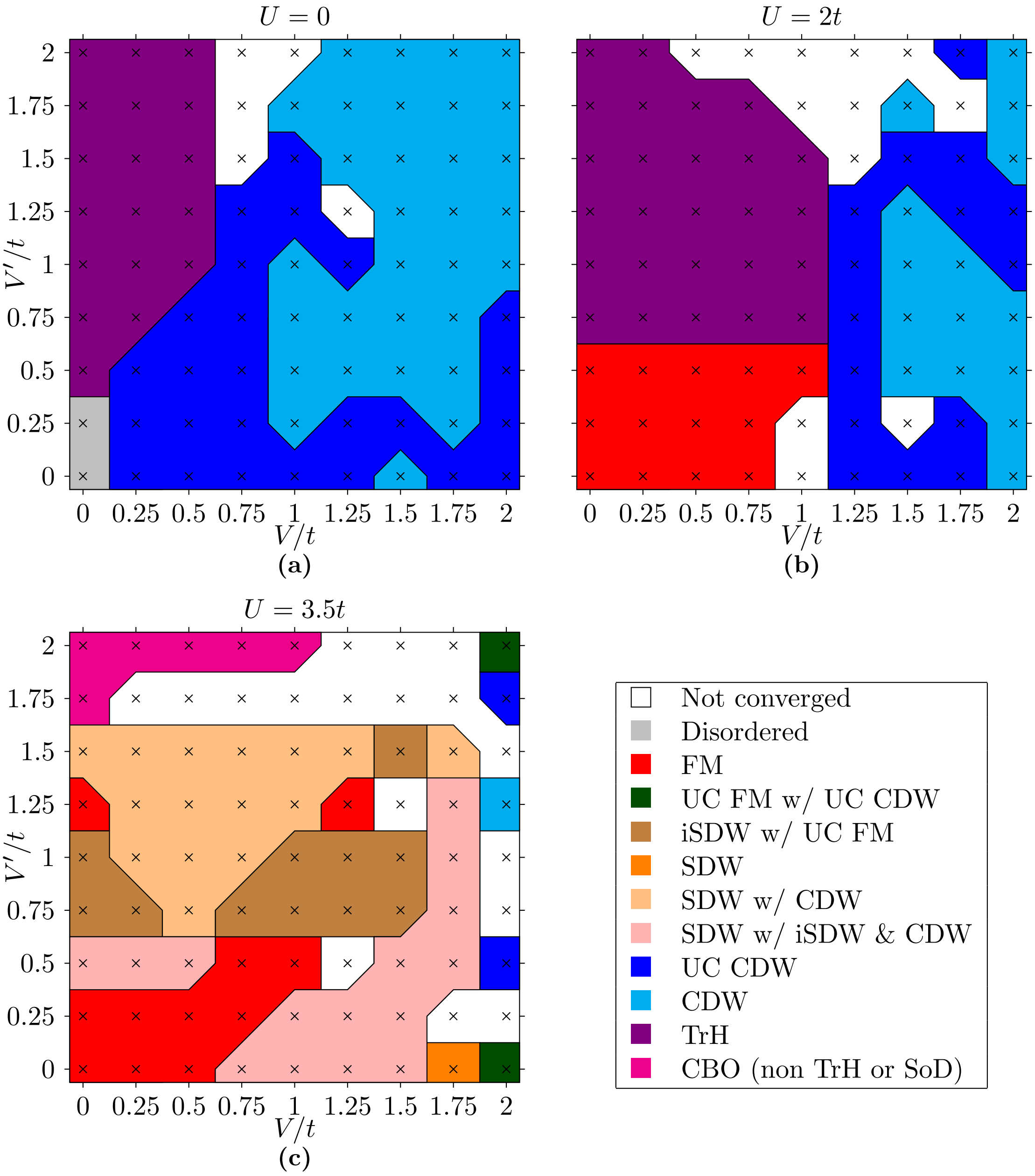

Figure 5.5: Phase diagrams at the upper van Hove point ($n_{\text{target}} = 5/12$) in the (V, V')-space, when **(a)** $U = 0$, **(b)** $U = 2t$ and **(c)** $U = 3.5t$. The × symbol marks the points in (V, V')-space tested in the algorithm, and the color codes of the phases are given in table to the lower right. All three cases are initialized with the random, Tri-Hexagonal and Star-of-David configurations.

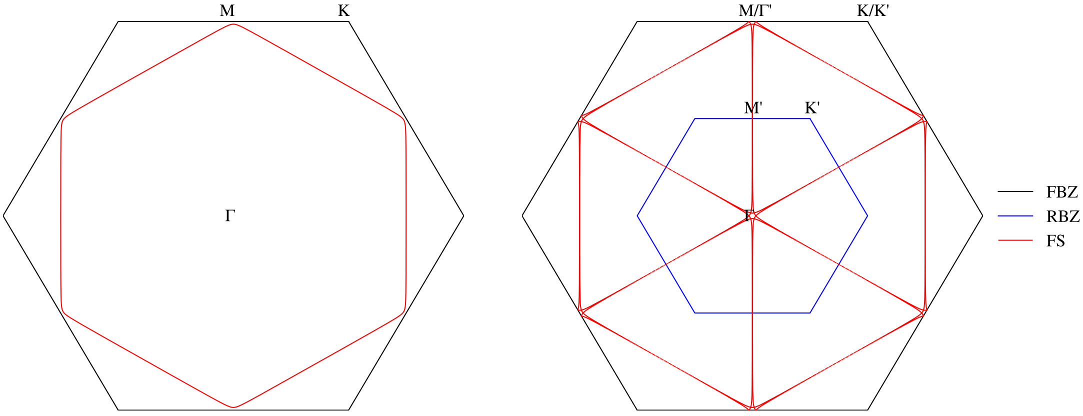

(a) **(b)**

Figure 5.6: The Fermi surface (FS) in the full Brillouin zone (FBZ) for the tight-binding model with the average density $\overline{n} = 5/12 + 0.02$, using the Hamiltonian assuming **(a)** conservation **(b)** breaking of translational symmetry. The high symmetry points of the first Brillouin zone are labelled, and in **(b)** are the boundaries of the reduced Brillouin zone indicated with the high symmetry points of that zone.

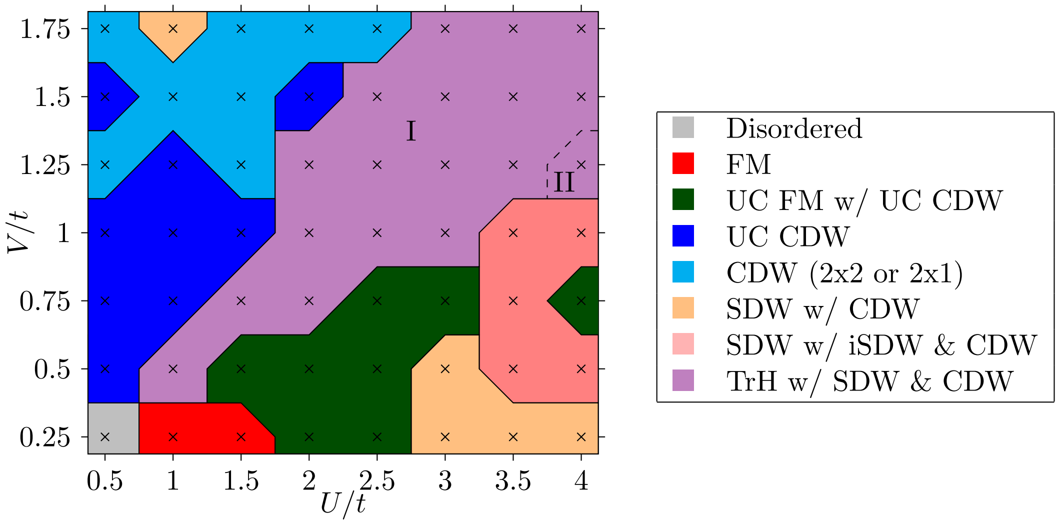

Figure 5.7: Phase Diagram above the upper van Hove point ($n_{\text{target}} = 5/12 + 0.02$) using the momentum space code. The × symbol marks the points in (U, V)-space tested in the algorithm, and the color codes of the different phases are given in the table to the right. The algorithm was initialized with random, Tri-Hexagonal, Star-of-David, coexisting Tri-Hexagonal and iCDW and coexisting Tri-Hexagonal and FM configurations.

lar nesting vector. We initialize the algorithm with the random, Tri-Hexagonal, Star-of David, coexisting Tri-Hexagonal and FM configurations and two coexisting Tri-Hexagonal and iCDWs configurations, where the currents resemble the two current configurations in Fig. 2.10. The phase diagram obtained from the momentum space code is given in Fig. 5.7.

The most interesting phase in the phase diagram is the large region with a coexisting Tri-Hexagonal, SDW and iCDW, which is found when $U \approx 2V$. We see two variations of the ordered state, found in the regions marked by the regions I and II, respectively. The

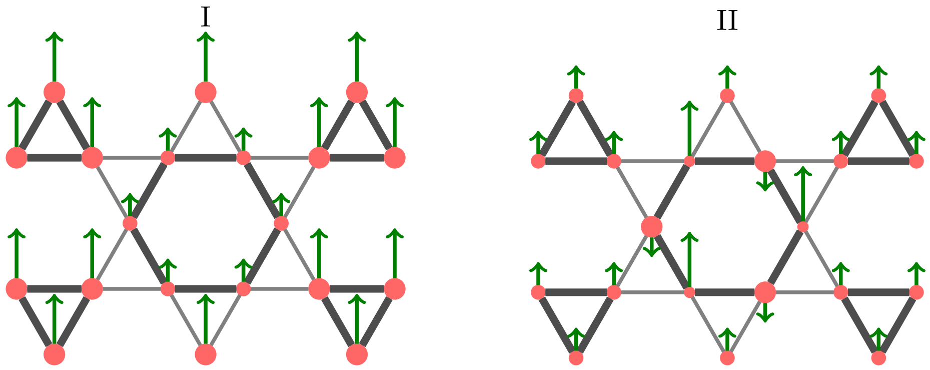

(a) **(b)**

Figure 5.8: The two coexisting Tri-Hexagonal, SDW and CDW ordered states found above the van Hove point. **(a)** and **(b)** is found in the regions I and II in Fig. 5.7, respectively. We note that while the order in **(a)** has conserved the symmetries of the D_6 point group, the order in **(b)** have broken rotational symmetry, such that it has a C_3 rotational symmetry, yielding the point group D_3.

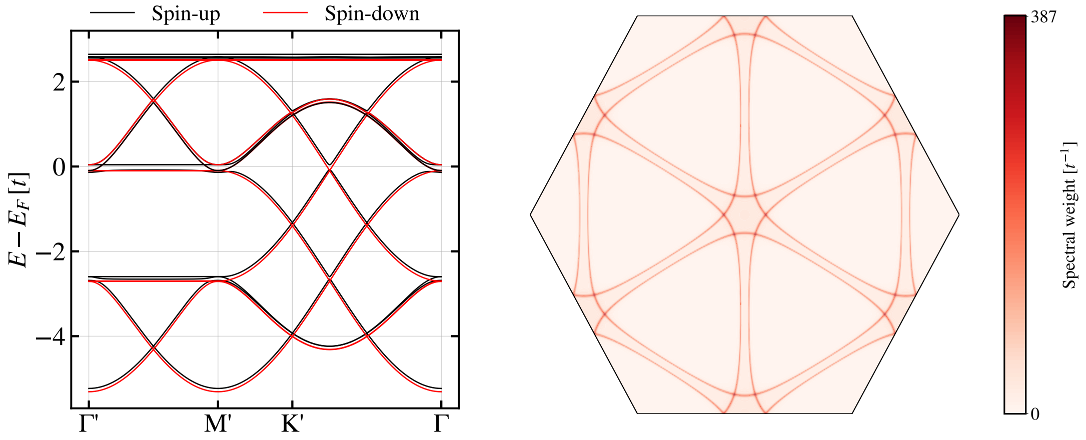

(a) **(b)**

Figure 5.9: **(a)** The band structure for the coexisting Tri-Hexagonal and SDW. Specific values taken for $U = 2t$, $V = t$. The red (black) lines represent the band structure of the spin-up (spin-down) electrons. **(b)** The spectral function of the coexisting Tri-Hexagonal and SDW at the Fermi energy. Values taken when $U = 2t$, $V = t$.

two orders are schematically drawn in Fig. 5.8. The ordered states break translational symmetry, creating a new unit cell of size $2a_0 \times 2a_0$, and time reversal symmetry. The order found in region II break the six-fold rotational symmetry, only having a three-fold rotational symmetry, leaving the state with the point group D_3. The ordered state in region I conserves the six-fold rotational symmetry, thus this phase has the same point group as the disordered state.

We can compare the phases studied here to the phase diagram at the same in target density in the FRG study (see Ref. [7]). First the FRG analysis does not find the bond ordered phase for any part of (U, V)-space that we examine here. The FRG study finds a ferromagnetic phase covering the region where $U \geq 2V$. This covers a much larger than the ferromagnetic phase found for $U \approx 1t$ and $V = 0.25t$. The FRG paper finds a superconducting phase for $V > 2U$, which our method cannot obtain. Furthermore, for large

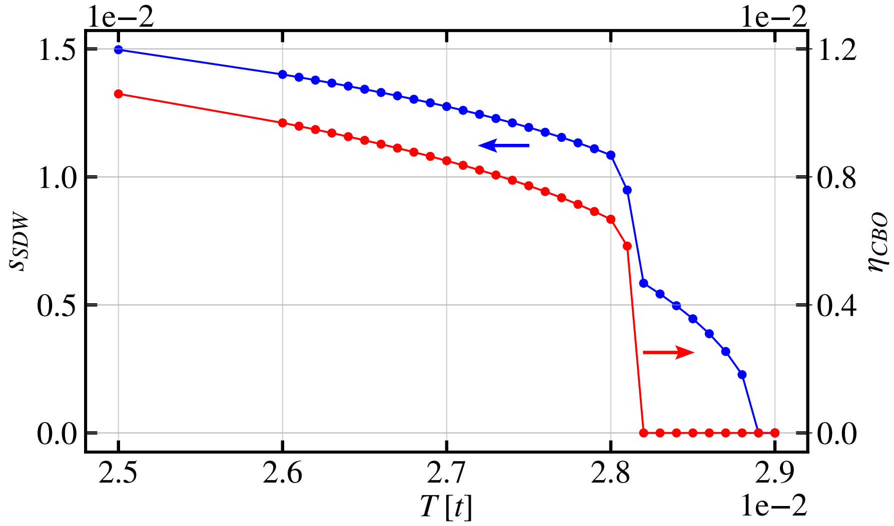

Figure 5.10: The temperature dependence of the bond order parameter associated with the charge bond order and of the spin order parameter associated with the spin density wave. A second order phase transition for a ferromagnetic phase is seen at $0.0289t$ and a first order phase transitions is seen at $0.0281t$ introducing the Tri-Hexagonal order and changing the ferromagnetic phase to a SDW. The plot is shown for $(U, V) = (2t, t)$.

parts of the (U, V)-space considered in this work, the FRG analysis could not determine the order precisely, as the critical ordering scales were too small.

We now examine the coexisting Tri-Hexagonal, SDW and CDW phase from region I. We plot the band structure of the ordered state in Fig. 5.9a. The degeneracy between spin up and spin down electrons is lifted for most parts of the band structure, and the gap is especially prevalent around the Fermi energy. The charge order further lifts a degeneracy at the Fermi energy. Due to the lifting of the degeneracy between spin-up and spin-down electrons, we now have bands crossing at the Fermi energy, meaning the phase is no longer band insulating. As the bands are not heavily reconstructed, only opening small gaps, we can consider the Hartree-Fock approximation to be valid for the ordered phase. We similarly plot the spectral function calculated at the Fermi energy for this state in Fig. 5.9b. Compared to the Fermi surface of the disordered state, the Fermi sea has expanded. Furthermore, the Fermi surface no longer appears to have straight lines instead bending inwards between the M points. We also note the absolute intensity of the spectral weight, which is much larger than the spectral weight of the two phases found at the upper van Hove point.

As the time reversal symmetry breaking happens either at the same temperature or at a lower temperature than the translational symmetry breaking in the kagome metals [27, 33], we want to consider which order develops first. To do this we plot the temperature dependence of a bond order parameter associated with the translational symmetry breaking and the magnitude of the spin vector associated with the spin density wave averaged over the sites in Fig. 5.10 for $(U, V) = (2t, t)$. We see two separate phase transitions. First at $T_{\text{FM}} = 0.0289t$, a second order phase transition introduces a ferromagnetic order. We note that this matches the result FRG study, where a ferromagnet is found at this point in (U, V)-space. At $T_{\text{CBO}} = 0.0281t$ a first order phase transition introduces the bond order and changes the magnetic order to break translational symmetry. To translate this temperature into measurable units, we estimate the value of $t = 0.5\,\text{eV}$ based on the minimal tight-binding model discussed in Chapter 6. The difference between the two critical temperatures are $\Delta T_C = 5\,\mathrm{K}$. Using a different point in (U, V)-space ($U = 3t$ and $V = 1.25t$), we obtain $\Delta T_C = 25\,\mathrm{K}$. This result does not match the sequence at which the two orders emerge in $\mathrm{AV_3Sb_5}$.

We, furthermore estimate the effective magnetic field felt by the electrons from the energy difference between the spin-up and spin-down particles at the Fermi level, using the relation $B_{\text{eff}} = \Delta E/\mu_B$. Considering the case where $(U, V) = (2t, t)$ and $T = 0.01t$ and assuming $t = 0.5\,\mathrm{eV}$, we obtain an effective magnetic field of $B_{\text{eff}} = 0.1\,\mathrm{G}$. This magnetic field can be compared to the effective magnetic field responsible for the time reversal symmetry breaking, which is estimated at $B_{\text{eff}} = 0.3\,\mathrm{G}$ [17]. As can be seen the two orders of magnitude matches well, which means we cannot exclude the coexisting Tri-Hexagonal, SDW and CDW depicted in Fig. 5.8a from being responsible for the time reversal symmetry broken phase.

5.3 At the lower van Hove point

We also construct the phase diagram for the lower van Hove point ($n_{\text{target}} = 1/4$). As discussed in Section 3.2, the nesting effects at the lower van Hove point enhance site orders doubling the unit cell. As we are still primarily interested in the charge bond ordered phases proposed for $\mathrm{AV_3Sb_5}$, we initialize with random, Tri-Hexagonal and Star-of-David configurations. We use the algorithm with the momentum space basis, showing the phase diagram in Fig. 5.11.

This phase diagram has three regimes. When $V > U$, we obtain a charge modulating phase, primarily seeing modulations inside the unit cell. Furthermore, when $U \geq V$, we see a ferromagnetic phase, and finally for $U \approx 4t$ and $V \approx 2t$, we see the coexisting phase

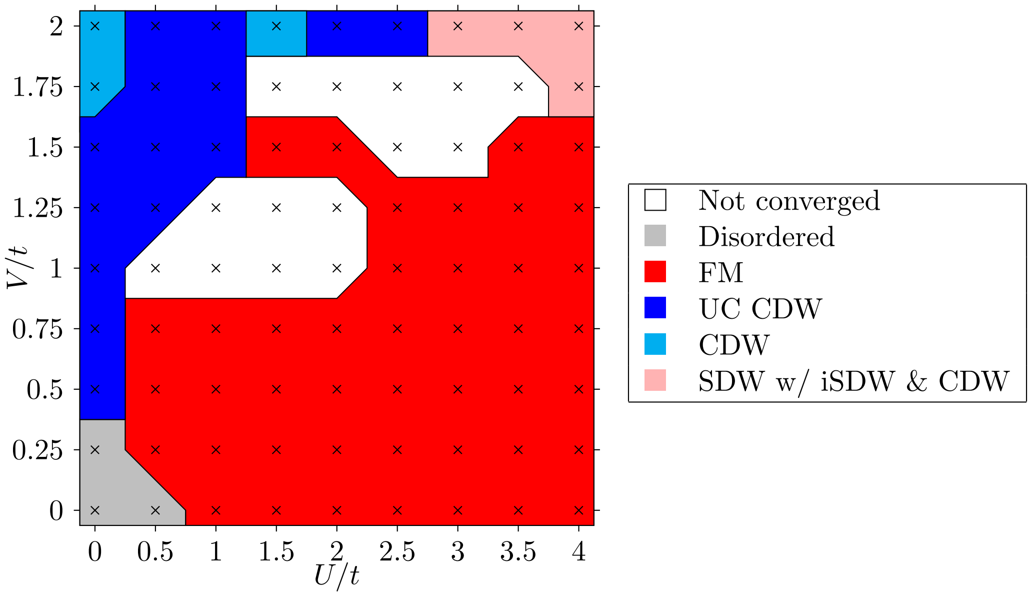

Figure 5.11: Phase Diagram at the lower van Hove point ($n_{\text{target}} = 1/4$) using momentum space code. The × symbol marks the points in (U, V)-space tested in the algorithm, and the color codes of the different phases are given in the table to the right. The algorithm was initialized with the random, Tri-Hexagonal and Star-of-David configurations.

containing SDW, iSDW and CDW. The limited number of points in (U, V)-space, where a translational symmetry breaking phase is found, could indicate that the initializations used in the algorithm are not covering the necessary configurations to obtain the global energy minimum for many points in (U, V)-space.

5.4 Summary of the results

We here give a short summary of the results obtained in this chapter.

- In the phase diagram at the upper van Hove point we find a Tri-Hexagonal phase. This phase has a lower free energy than the Star-of-David configuration making the Tri-Hexagonal phase the ground state. Furthermore, the phase is robust against changes to interaction strengths. The band structure of the Tri-Hexagonal phase reveals a small gap opening at the Fermi surface leaving the ordered state a band-insulator.

- At the upper van Hove point we further find two different coexisting Tri-Hexagonal, SDW and CDW phase orders. The variant found at $(U, V) = (3t, t)$ conserves the six-fold rotational symmetry and the mirror symmetries, while breaking translational symmetry and time reversal symmetry. Hence, the phase has the same symmetries as the kagome metals in the charge ordered phase. A gap has opened at the Fermi energy leaving the state a band-insulator.

- In the phase diagram above the upper van Hove point, we again find two different coexisting Tri-Hexagonal, SDW and CDW phase orders, none of them the same as the orders found at the upper van Hove point. The phase found in the region I, conserves the six-fold rotational symmetry and the mirror symmetries, while breaking translational symmetry and time reversal symmetry. Hence, the phase has the same symmetries as the kagome metals in the charge ordered phase. From the band structure we see a degeneracy lifted between the spin-up and the spin-down particles, which results in band crossings at the Fermi level, thus this phase is no t band insulating.

Chapter 6

Seven band model

So far, we have studied the pristine two-dimensional kagome lattice only considering electrons hopping between nearest neighbor sites. While this model is applicable to the recently discovered kagome materials, it does not capture the specific intricacies of the material. To obtain a more materially specific model, one can from DFT calculations construct minimal tight-binding models, which captures most of the important physics of the model, without the large computational costs of using the entire DFT calculated band structure. The minimal tight-binding model includes multiple orbitals and hopping strengths between sites that are not nearest neighbors. The limitations of a minimal model comes from the choices made regarding the "important physics." This can limit its applicability to our purpose, which is to use it as the base model for an unrestricted Hartree-Fock mean field analysis.

Y. Gu *et al.* introduced two minimal tight-binding models based on DFT calculations of $\mathrm{CsV_3Sb_5}$ in Ref. [15]. Their models use d orbitals from the vanadium sites and p orbitals from the in-plane antimony sites, meaning the models are kept in two dimensions, making the code more efficient and viable as a basis of a self-consistency algorithm. The models were used to study the spin orbit coupling of the materials and if any edge state show gapless excitations.

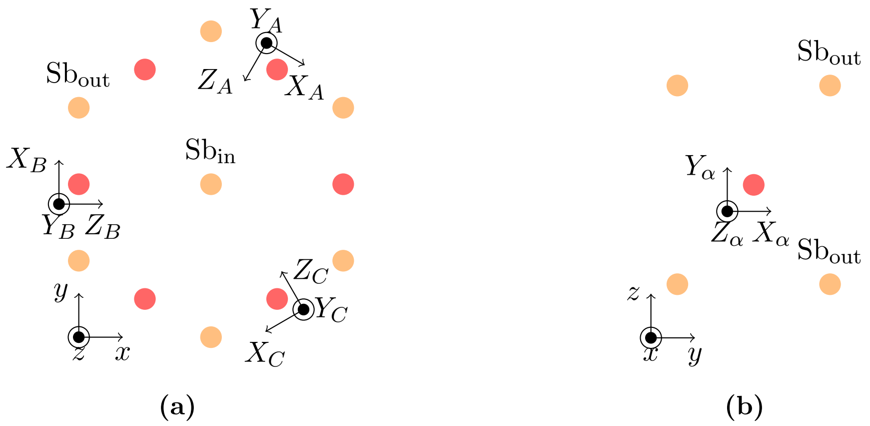

Figure 6.1: Schematic drawings showing the transformation to the local coordinate system (X, Y, Z) from the global coordinate system (x, y, z), showing **(a)** the kagome plane **(b)** the plane perpendicular to the kagome plane. Furthermore, the sublattice label is given for the local coordinate systems, associated with the site in **(a)**, where the local coordinate system in **(b)** is the same for all sites. Out-of-plane and in-plane antimony sites are labelled.

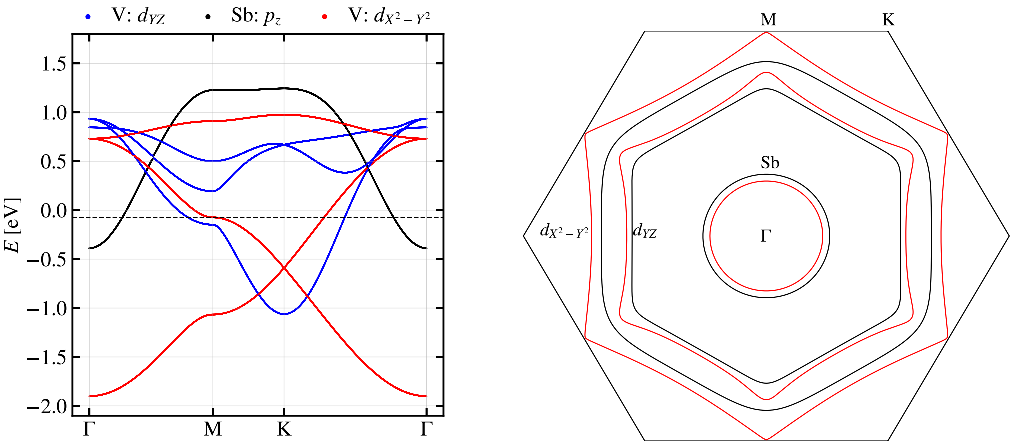

(a) **(b)**

Figure 6.2: **(a)** The band structure of the seven band model. The red, blue, black bands shows the contributions from the vanadium $d_{X^2-Y^2}$, vanadium d_{YZ} and antimony p_z orbitals respectively. The red line closely resembles the dispersion of the dispersion of the kagome lattice. The dashed line indicates the Fermi energy chosen in this thesis. **(b)** The Fermi surface of the seven band model. The black line represents the choice of the authors of the model, and the red line shows our choice of the Fermi surface. The contribution of the different orbitals are labelled together with the high symmetry points of the kagome lattice.

To construct the tight-binding models, the authors transform the system into a local coordinate system (X, Y, Z) for each site, such that the crystal appears the same for all vanadium sites. The coordinate transformation is sketched in Fig. 6.1. Y is the out-of-plane direction, Z is the direction to the nearest in-plane antimony site and X is the direction in-plane between the out-of-plane antimony sites. With this local coordinate system, the nearest antimony sites create a distorted octahedral, such that the orbitals can be written in ascending order in terms of energy as $d_{X^2-Y^2}$, d_{YZ}, d_{XZ}, d_{XY} and d_{Z^2}. The authors find that the orbitals associated with the two van Hove points near the Fermi surface is associated with the $d_{X^2-Y^2}$ and d_{YZ} orbitals in the local coordinate system. Furthermore, the electron pocket around the Γ point comes from the antimony p_z orbital. The authors choose these three orbitals to base the minimal tight-binding model yielding seven bands in total. To obtain the parameters of the model including up to 5$^{\text{th}}$ nearest neighbor hoppings, the tight-binding model is fitted to the DFT calculations. The tight-binding Hamiltonian has the structure

$$H = \begin{pmatrix} H_{X^2-Y^2} & 0 & 0 \\ 0 & H_{\mathrm{Sb}} & V \\ 0 & V^\dagger & H_{YZ} \end{pmatrix}, \tag{6.1}$$

where H_{Sb} is a number, $H_{X^2-Y^2}$ and H_{YZ} are three by three matrices in sublattice space, and V is a one by three matrix. We write the expressions for each entry in the Hamiltonian in Appendix B. The band structure is shown in Fig. 6.2a. As wanted the two van Hove points at M below the Fermi energy are captured well within this model as is the electron pocket around Γ from the antimony p_z orbital. We also compare the Fermi surface of the seven band model plotted in Fig. 6.2b comparing to ARPES results from Ref. [9, 10]. We notice that Fermi surface from the $d_{X^2-Y^2}$ does not resemble any of data seen in ARPES. However, by changing the chemical potential, we get the concave Fermi surface from experiments. Furthermore, the contribution to the Fermi surface from the d_{YZ} orbital in the model does not seem to have any connection to the ARPES data.

6.1 Modifications to the interaction Hamiltonian

As we have now introduced multiple orbitals on each site, we have to consider Coulomb repulsion between the electrons in different orbitals. We introduce some notation letting κ represent both site and the orbital on the site and let $\overline{\kappa}$ represent the other orbital on the same site. We follow Olés (Ref. [44]), and consider three contributions. A density-density interaction, parametrized by U'

$$H_{U'} = \frac{U'}{2} \sum_{\mathbf{R}\kappa\sigma\sigma'} n_{\mathbf{R}\kappa\sigma} n_{\mathbf{R}\overline{\kappa}\sigma'}, \tag{6.2}$$

where the factor of 1/2 is to account for double counting of the orbitals. Hund's coupling

$$H_J = -\frac{J}{2} \sum_{\mathbf{R}\kappa\sigma\sigma'} c^{\dagger}_{\mathbf{R}\kappa\sigma} c_{\mathbf{R}\kappa\sigma'} c^{\dagger}_{\mathbf{R}\overline{\kappa}\sigma'} c_{\mathbf{R}\overline{\kappa}\sigma}, \tag{6.3}$$

where 1/2 is similarly introduced to account for double counting. The pair wise coupling

$$H_{J'} = J' \sum_{\mathbf{R}\kappa} c^{\dagger}_{\mathbf{R}\kappa\uparrow} c_{\mathbf{R}\overline{\kappa}\uparrow} c^{\dagger}_{\mathbf{R}\kappa\downarrow} c_{\mathbf{R}\overline{\kappa}\downarrow}. \tag{6.4}$$

We will set $J = J' = U/r$, where $r \geq 2$. We set $U' = U - 2J$. In this way $U \geq U' \geq 0$ and $U \geq J$, meaning the strongest repulsion comes from interactions in the same orbital, which matches Hund's rules. We choose to write the Hamiltonian in the momentum space basis, as the algorithm is more efficient in this basis. We thus Fourier transform the interactions into momentum space and mean field decouple them

$$H_{U'} = \frac{U'}{\sqrt{N}} \sum_{\mathbf{qk}} \sum_{\kappa\sigma\sigma'} (\Delta^{\kappa\sigma\kappa\sigma}_{\mathbf{q}+} c^{\dagger}_{\mathbf{k}\overline{\kappa}\sigma'} c_{\mathbf{k}+\mathbf{q}\overline{\kappa}\sigma'} - \Delta^{\kappa\sigma\overline{\kappa}\sigma'}_{\mathbf{q}+} c^{\dagger}_{\mathbf{k}\overline{\kappa}\sigma'} c_{\mathbf{k}+\mathbf{q}\kappa\sigma}) \tag{6.5}$$

$$H_J = -\frac{J}{\sqrt{N}} \sum_{\mathbf{qk}} \sum_{\kappa\sigma\sigma'} (\Delta^{\kappa\sigma\kappa\sigma'}_{\mathbf{q}+} c^{\dagger}_{\mathbf{k}\overline{\kappa}\sigma'} c_{\mathbf{k}+\mathbf{q}\overline{\kappa}\sigma} - \Delta^{\kappa\sigma\overline{\kappa}\sigma}_{\mathbf{q}+} c^{\dagger}_{\mathbf{k}\overline{\kappa}\sigma'} c_{\mathbf{k}+\mathbf{q}\kappa\sigma'}) \tag{6.6}$$

$$H_{J'} = \frac{J'}{\sqrt{N}} \sum_{\mathbf{qk}} \sum_{\kappa\sigma} (\Delta^{\kappa\sigma\overline{\kappa}\sigma}_{\mathbf{q}+} c^{\dagger}_{\mathbf{k}\kappa\overline{\sigma}} c_{\mathbf{k}+\mathbf{q}\overline{\kappa}\,\overline{\sigma}} - \Delta^{\kappa\sigma\overline{\kappa\sigma}}_{\mathbf{q}+} c^{\dagger}_{\mathbf{k}\kappa\overline{\sigma}} c_{\mathbf{k}+\mathbf{q}\overline{\kappa}\sigma}). \tag{6.7}$$

Similarly, the correction to the total energies are calculated

$$E^{\text{crxn}}_{U'} = -\frac{U'}{2} \sum_{\mathbf{q}\kappa\sigma\sigma'} \left(\Delta^{\kappa\sigma\kappa\sigma}_{\mathbf{q}+} \Delta^{\overline{\kappa}\sigma'\overline{\kappa}\sigma'}_{\mathbf{q}+} - \Delta^{\kappa\sigma\overline{\kappa}\sigma'}_{\mathbf{q}+} \Delta^{\overline{\kappa}\sigma'\kappa\sigma}_{\mathbf{q}+} \right) \tag{6.8}$$

$$E^{\text{crxn}}_{J} = \frac{J}{2} \sum_{\mathbf{q}\kappa\sigma\sigma'} \left(\Delta^{\kappa\sigma\kappa\sigma'}_{\mathbf{q}+} \Delta^{\overline{\kappa}\sigma'\overline{\kappa}\sigma}_{\mathbf{q}+} - \Delta^{\kappa\sigma\overline{\kappa}\sigma}_{\mathbf{q}+} \Delta^{\overline{\kappa}\sigma'\kappa\sigma'}_{\mathbf{q}+} \right) \tag{6.9}$$

$$E^{\text{crxn}}_{J'} = -J' \sum_{\mathbf{q}\kappa\sigma} (\Delta^{\kappa\sigma\overline{\kappa}\sigma}_{\mathbf{q}+} \Delta^{\kappa\overline{\sigma}\,\overline{\kappa}\,\overline{\sigma}}_{\mathbf{q}+} - \Delta^{\kappa\sigma\overline{\kappa}\,\overline{\sigma}}_{\mathbf{q}+} \Delta^{\kappa\overline{\sigma}\,\overline{\kappa}\sigma}_{\mathbf{q}+}). \tag{6.10}$$

The detailed calculations are written in Appendix C.

Finally, we discuss the interactions with electrons on the antimony p_z orbital. Since the contribution to the Fermi surface of the antimony orbital seems to change little when

AV_3Sb_5 enters the charge bond ordering phase [18], will we try to limit the effect of the interactions on the antimony orbital. Hence, we do not allow for nearest neighbor interactions between the vanadium sites and the antimony sites or between different antimony sites. Regarding the Hubbard interaction, we define a U_{Sb}, such that the strength of the Hubbard interaction on the antimony p_z orbital is given by $U_{\text{Sb}} \equiv \lambda U$. This allows us to tune the strength of magnetic moments on the antimony sites. As the p orbital on the antimony sites are not localized as sharply as the d orbitals on the vanadium sites [14], we only consider $0 \leq \lambda \leq 1$.

The system is in the grand canonical ensemble, and we only know the average density of electrons over all types of orbitals, meaning we have one common chemical potential.

6.2 Candidate phases

The candidate phases introduced in Section 4.5, will with small changes to their definitions, be applicable for the seven band model. Most importantly any ordered phase not breaking translational symmetry, will have to deviate for each orbital. As an example, we will consider a state ferromagnetic if all spins from the same orbital has the same magnitude and direction. Thus, if the spins of the antimony p_z orbital and the vanadium $d_{X^2-Y^2}$ orbital point in different directions, we will still consider it a ferromagnetic state if the spins of the vanadium $d_{X^2-Y^2}$ orbitals point in the same direction. This choice is made, as the electrons on the p_z orbital in the non-interacting case are only coupled to the electrons on the vanadium sites, through the tunneling between the antimony p_z orbital and the vanadium d_{YZ} orbital.

6.3 Results

We consider a system of 12 by 12 unit cells, yielding 36 momenta in the reduced Brillouin zone, and the system has a temperature of $T = 0.005\,\text{eV}$. We initialize with the random, Tri-Hexagonal, Star-of-David, coexisting FM w/ iSDW and iCDW, shown in Fig. 6.4, coexisting Tri-Hexagonal and FM and coexisting Tri-Hexagonal and iCDW configurations, where the currents resemble the configurations in Fig. 2.10. The algorithm is examined with two values of U_{Sb}: $U_{\text{Sb}} = 0$ and $U_{\text{Sb}} = U/2$. The resulting phase diagrams are seen in Fig. 6.3.

The two phase diagrams have similar overall regimes, so we will deal with them at the same time. First, when $V < 1\,\text{eV}$, we have a disordered phase, where the only structure is a relocation of charges between the different orbitals. For $U_{\text{Sb}} = U/2$ the phase is further limited, by $U < 1\,\text{eV}$. A ferromagnetic phase appears for when $U \geq 1\,\text{eV}$, as magnetic moments on the antimony sites lowers the free energy here and redistributing of charges has a smaller effect compared to the case where $U_{\text{Sb}} = 0$

When $U \lesssim 1\,\text{eV}$, $V \gtrsim 1\,\text{eV}$ we see charge density wave orders breaking translational symmetry, similar to the results from the three band model. We get a co-existing UC CDW and a UCFM when $U \geq 1.5\,\text{eV}$ and $V \approx 1.25\,\text{eV}$. This phase covers a larger area of (U, V)-space when $U_{\text{Sb}} = 0$ compared to $U_{\text{Sb}} = U/2$. Furthermore, we obtain a coexisting CDW and SDW phase when $U \gtrsim 1.5\,\text{eV}$ and $V \gtrsim 1.5\,\text{eV}$. Finally, when $U = 2.25\,\text{eV}$, $V = 0.75\,\text{eV}$ and $U_{\text{Sb}} = \frac{1}{2}$, and for $U_{\text{Sb}} = 0$ in the regions around $V = 0.75\,\text{eV}$ and $U = 1.5\,\text{eV}$ and around $U = 2.5\,\text{eV}$ and $V = 1\,\text{eV}$ a coexisting FM, iSDW and iCDW is found. The phase is schematically drawn in Fig. 6.4. It contains loop currents between the

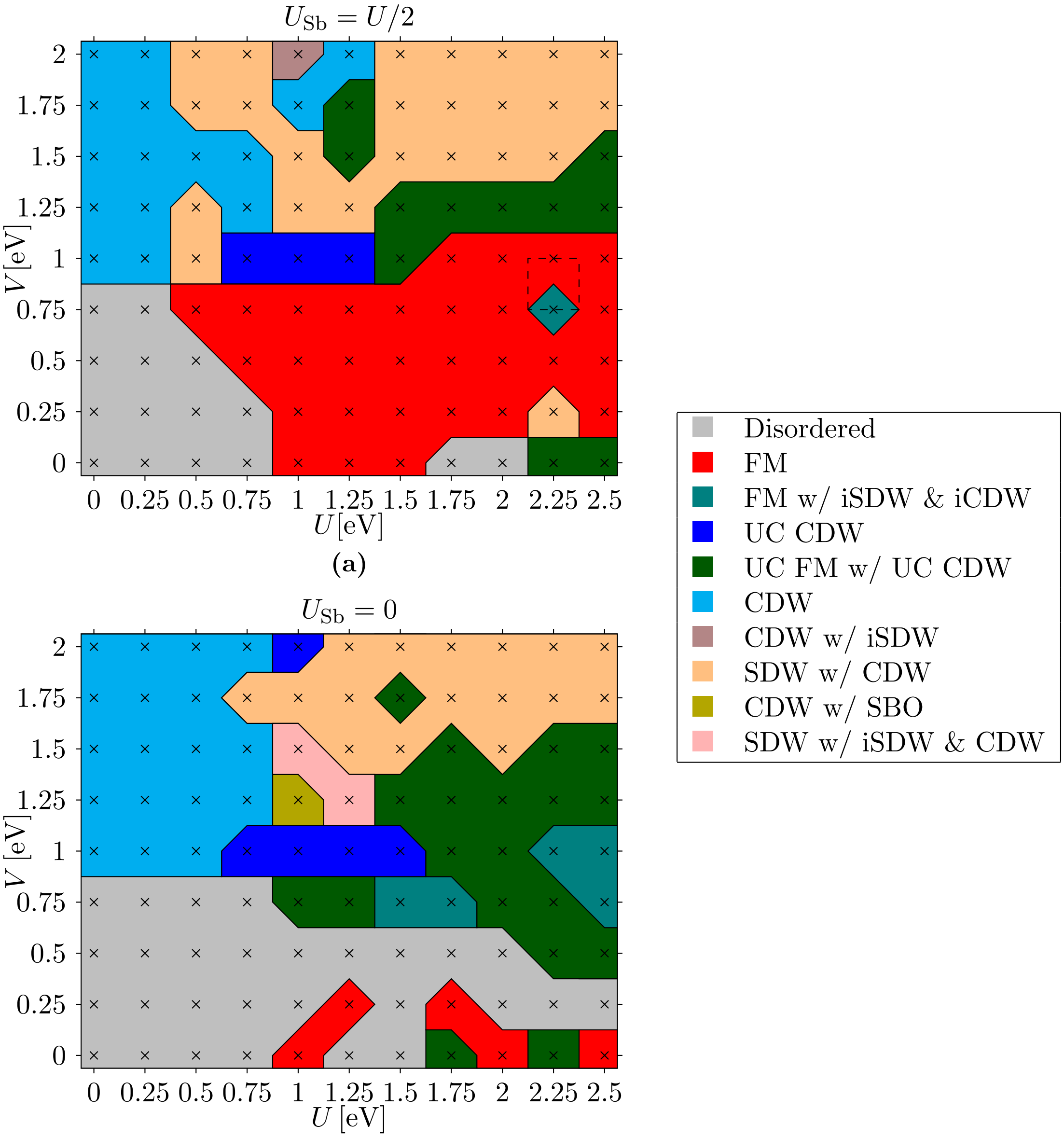

(b)

Figure 6.3: Phase Diagram for the seven band model with **(a)** $U_{\mathrm{Sb}} = U/2$ and **(b)** $U_{\mathrm{Sb}} = 0$ using the self-consistency algorithm. The color codes of the phases is seen in the table to the right and the × symbol marks the points in (U, V)-space tested with the algorithm.

vanadium sites, which has the same spatial modulation as the proposal for loop currents in kagome metals from Ref. [17].

The loop currents in this phase comes from electrons in the vanadium d_{YZ} orbitals moving between the different sites, which can explain, why they are not seen in the pristine kagome lattice, as the contribution to the band structure from the d_{YZ} orbital does not have a similar dispersion as the band structure of the pristine kagome lattice found in Section 3.2. Apart from time reversal symmetry, the order breaks mirror symmetry, hence the point group of the ordered phase is C_6. In Fig. 6.5 we check how robust the phase is against changes in the interaction strengths. Small variations in U, V and U_{Sb} changes the solution of the self-consistency algorithm. This lack of robustness indicates that either

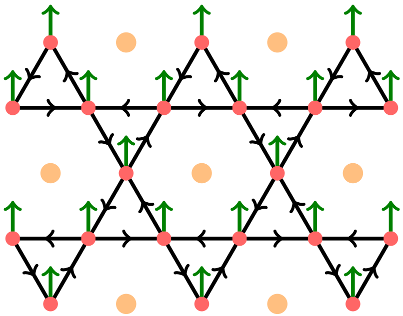

Figure 6.4: Schematic drawing of the coexisting FM, iSDW and iCDW, for $U_{\mathrm{Sb}} = 0$. For the case when $U_{\mathrm{Sb}} = U/2$, is identical to this case, except a magnetic moment appears on the antimony sites. This moment is much larger than the moments on the vanadium sites.

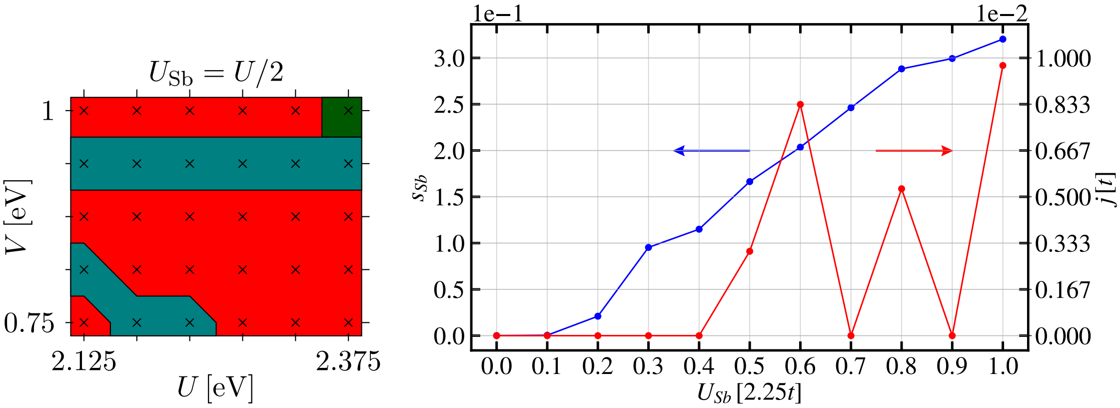

(a) **(b)**

Figure 6.5: **(a)** The phase diagram at the zoomed in area marked in Fig. 6.3, with $U_{\mathrm{Sb}} = U/2$. The color codes of the phases are similarly found in Fig. 6.3 **(b)** A plot of the size of the magnetic moment of the antimony site (blue curve), and the current in the system (red curve).

the state is susceptible to small changes of the interaction strength, and small deviations from the end state are enough to converge to a different solution, or the state is meta stable, i.e. the true ground state of the system has not been found.

We plot the reconstructed band structure of the loop current phase in Fig. 6.6a. We notice that a relative shift in energy between the bands have taken place compared to the band structure of the non-interacting tight-binding model. This relative shift means the van Hove points of the vanadium $d_{X^2-Y^2}$ or d_{YZ} orbitals are no longer close to the Fermi energy. Furthermore, the density of the antimony orbital has increased due to the shift down in energy. This can also be seen on the spectral function plotted in Fig. 6.6b. Compared with the Fermi surface of the disordered state, we see that the contribution from the antimony orbital has a larger radius, indicating more occupied states. Similarly, the contributions form the vanadium orbitals are closer to the K points of the first Brillouin zone indicating a lower occupation compared to the disordered state. This means that the system does not model an ordered state of the kagome metals, and we can not use the result to make direct conclusions on the materials. A relative shift in energy between the bands is seen for other points in (U, V)-space and for both values of $U_{\mathrm{Sb}} = U/2$. Thus, the issue seen here is not specific to the phase, but rather a general problem related to

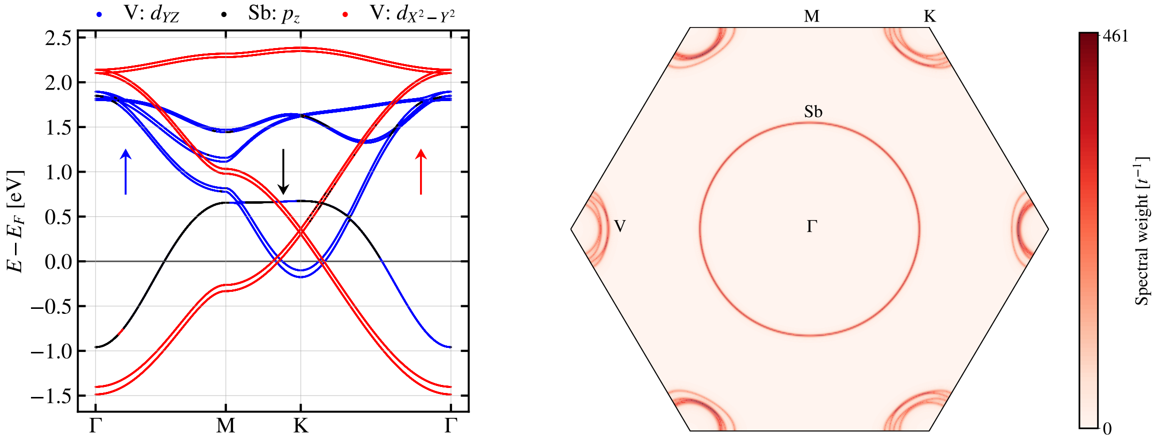

(a) **(b)**

Figure 6.6: **(a)** The reconstructed band structure of the coexisting FM, iSDW and iCDW phase plotted along the high symmetry path of the first Brillouin zone where the color code of the different orbitals is shown. The Fermi energy is marked by the black line. The arrows indicate the relative shift in energy between the bands compared to the disordered state. **(b)** The spectral function calculated at the Fermi energy, revealing the Fermi surface. The high symmetry points are labelled, and the dominant orbital of the contributions to the Fermi surface are labelled. As the order conserves translational symmetry, we only plot the contributions from the mean fields with momentum $\mathbf{0}$. The data is taken for $U = 1.75\,\mathrm{eV}$, $V = 0.75\,\mathrm{eV}$ and $U_{\mathrm{Sb}} = 0$.

how the system is modelled.

Chapter 7

Conclusion and outlook

In the thesis we have implemented a tight-binding model for the kagome lattice and found the band structure. From the band structure we argued, why nesting effects at the upper van Hove point are likely to enhance charge bond orders breaking translational symmetry such that the new unit cell has a size of $2a_0 \times 2a_0$. We further introduced interactions to the tight-binding Hamiltonian in the form of an on site Hubbard interaction and a nearest neighbor repulsion. Using mean field theory the interactions were decoupled to yield an effective two-operator Hamiltonian, that could be solved numerically. We implemented a self-consistency algorithm to solve the mean field Hamiltonian and obtained phase diagram for systems at various average densities. For the upper van Hove point, we found that the Tri-Hexagonal and Star-of-David bond orders were stable solutions of the self-consistency algorithm. Furthermore, we found that the Tri-Hexagonal phase had a lower free energy compared to the Star-of-David order, and that the Tri-Hexagonal phase were the ground state in a region in (U, V)-space. Moreover, we find a coexisting Tri-Hexagonal and SDW phase when looking for phases above the upper van Hove point. This phase breaks time reversal and translational symmetry as has been reported in the new kagome metals [17, 31]

We further implemented a materially specific minimal tight binding based on $\mathrm{CsV_3Sb_5}$ presented in Ref. [15]. First we adjusted the Fermi level of the model to better fit the Fermi surface found by ARPES experiments. We then implemented the Hubbard-Hund model for the interactions between orbitals. These interactions were mean field decoupled and implemented in the self-consistent algorithm. Phase diagrams were obtained at the van Hove point for two different Hubbard interaction strengths on the antimony sites. In the phase diagrams we found a phase with loop currents following a previously proposed current pattern [17]. The phase had coexisting magnetic moments on the sites and spin current and no bond order. The state was found to be susceptible to variations in the interaction strengths, which could hint at the phase being a meta stable solution to the self-consistency algorithm. Furthermore, the phase was found to have reconstructed bands where a relative shift had occurred between the antimony orbital and the vanadium orbitals, meaning the ordered state no longer had a Fermi surface resembling the kagome metals.

With this work we have added evidence to the argument that the Tri-Hexagonal bond order configuration is the ground state for the translational symmetry breaking found in $\mathrm{AV_3Sb_5}$. We find that the order can be driven solely by the electronic states and the nesting effects, which is a counter example to previous studies where phonons were a vital ingredient to observe the ordered state [23].

The work presented in this thesis cannot help us draw any conclusions about how time reversal symmetry is broken in the kagome metals. Where the effective magnetic field found for the coexisting Tri-Hexagonal, SDW and CDW phase at $n_{\text{target}} = 5/12 + 0.02$ of $0.1\,\mathrm{G}$ matches the order of magnitude of magnetic fields found in the new kagome metals [17]. However, the critical temperature of the time reversal symmetry breaking is higher than the critical temperature of the bond order. The loop current phase found in the seven band model have a relative shift in the energy between the bands associated with the different orbitals, meaning the results cannot be applied directly to the time reversal symmetry breaking order in the kagome metals. However, the mere presence of loop currents emerging from a minimal tight-binding model fitted to $\mathrm{CsV_3Sb_5}$, means that loop currents, as an explanation for time reversal symmetry breaking, cannot be ruled out.

It is by now on experimentally solid ground that the charge bond ordered phase in the new kagome metals breaks time reversal symmetry, thus a possible step to move the theoretical work forward is to understand how time reversal symmetry is broken. Here the minimal tight binding model is a place to expand upon the findings presented in this thesis. Modifications to the model should address the problem of the charges concentrating on the antimony site. One possibility is to consider a grand canonical ensemble where the average electron density on each atom is known, effectively yielding two chemical potentials, which would ensure the bands have the correct structure relative to each other. Such an attempt was made in this project; however, the algorithm converged for limited values in (U, V)-space, meaning no conclusions could be made from the results. Another approach is to expand upon the work done by Y. Gu *et. al.* in Ref. [15] and make a revision of the minimal tight-binding model with a greater emphasis on a Fermi surface matching the results of the ARPES experiments more closely.

Another path is to reconsider the pristine kagome lattice, and introduce multiple kagome layers to study the out of plane modulation of the charge order in a layered kagome lattice. Regarding experiments a revisit of the experiments ruling out magnetic moments on the vanadium sites could be needed, due to the phases found on the kagome lattice in this study. Furthermore, for both theorists and experimentalists, how the charge bond order influences superconductivity is an unsolved question, which could be as step towards finding the exotic phenomena proposed for the kagome metals $\mathrm{AV_3Sb_5}$.

Bibliography

[1] I. Syozi. Statistics of Kagome Lattice. *Progress of Theoretical Physics*, 6(3):306–308, June 1951. ISSN 0033-068X, 1347-4081. doi: 10.1143/ptp/6.3.306. URL `https://academic.oup.com/ptp/article-lookup/doi/10.1143/ptp/6.3.306`.

[2] Yi Zhou, Kazushi Kanoda, and Tai-Kai Ng. Quantum spin liquid states. *Rev. Mod. Phys.*, 89(2):025003, April 2017. ISSN 0034-6861, 1539-0756. doi: 10.1103/RevModPhys.89.025003. URL `http://link.aps.org/doi/10.1103/RevModPhys.89.025003`.

[3] Jun Wen, Andreas Rüegg, C.-C. Joseph Wang, and Gregory A. Fiete. Interaction-driven topological insulators on the kagome and the decorated honeycomb lattices. *Phys. Rev. B*, 82(7):075125, August 2010. ISSN 1098-0121, 1550-235X. doi: 10.1103/PhysRevB.82.075125. URL `https://link.aps.org/doi/10.1103/PhysRevB.82.075125`.

[4] H.-M. Guo and M. Franz. Topological insulator on the kagome lattice. *Phys. Rev. B*, 80(11):113102, September 2009. ISSN 1098-0121, 1550-235X. doi: 10.1103/PhysRevB.80.113102. URL `https://link.aps.org/doi/10.1103/PhysRevB.80.113102`.

[5] Léon Van Hove. The Occurrence of Singularities in the Elastic Frequency Distribution of a Crystal. *Phys. Rev.*, 89(6):1189–1193, March 1953. ISSN 0031-899X. doi: 10.1103/PhysRev.89.1189. URL `https://link.aps.org/doi/10.1103/PhysRev.89.1189`.

[6] Wan-Sheng Wang, Zheng-Zhao Li, Yuan-Yuan Xiang, and Qiang-Hua Wang. Competing electronic orders on kagome lattices at van Hove filling. *Phys. Rev. B*, 87(11):115135, March 2013. ISSN 1098-0121, 1550-235X. doi: 10.1103/PhysRevB.87.115135. URL `https://link.aps.org/doi/10.1103/PhysRevB.87.115135`.

[7] Maximilian L. Kiesel, Christian Platt, and Ronny Thomale. Unconventional Fermi Surface Instabilities in the Kagome Hubbard Model. *Phys. Rev. Lett.*, 110(12):126405, March 2013. ISSN 0031-9007, 1079-7114. doi: 10.1103/PhysRevLett.110.126405. URL `https://link.aps.org/doi/10.1103/PhysRevLett.110.126405`.

[8] Brenden R. Ortiz, Lídia C. Gomes, Jennifer R. Morey, Michal Winiarski, Mitchell Bordelon, John S. Mangum, Iain W. H. Oswald, Jose A. Rodriguez-Rivera, James R. Neilson, Stephen D. Wilson, Elif Ertekin, Tyrel M. McQueen, and Eric S. Toberer. New kagome prototype materials: discovery of KV_3Sb_5, RbV_3Sb_5 , and CsV_3Sb_5. *Phys. Rev. Materials*, 3(9):094407, September 2019. ISSN 2475-9953. doi: 10.1103/PhysRevMaterials.3.094407. URL `https://link.aps.org/doi/10.1103/PhysRevMaterials.3.094407`.

[9] Brenden R. Ortiz, Samuel M. L. Teicher, Yong Hu, Julia L. Zuo, Paul M. Sarte, Emily C. Schueller, A. M. Milinda Abeykoon, Matthew J. Krogstad, Stephan Rosenkranz, Raymond Osborn, Ram Seshadri, Leon Balents, Junfeng He, and Stephen D. Wilson. $\mathrm{CsV_3Sb_5}$: A $\mathbb{Z}_2$ Topological Kagome Metal with a Superconducting Ground State. *Phys. Rev. Lett.*, 125(24):247002, December 2020. ISSN 0031-9007, 1079-7114. doi: 10.1103/PhysRevLett.125.247002. URL `https://link.aps.org/doi/10.1103/PhysRevLett.125.247002`.

[10] Mingu Kang, Shiang Fang, Jeong-Kyu Kim, Brenden R. Ortiz, Sae Hee Ryu, Jimin Kim, Jonggyu Yoo, Giorgio Sangiovanni, Domenico Di Sante, Byeong-Gyu Park, Chris Jozwiak, Aaron Bostwick, Eli Rotenberg, Efthimios Kaxiras, Stephen D. Wilson, Jae-Hoon Park, and Riccardo Comin. Twofold van Hove singularity and origin of charge order in topological kagome superconductor $\mathrm{CsV_3Sb_5}$. *Nat. Phys.*, 18(3): 301–308, March 2022. ISSN 1745-2473, 1745-2481. doi: 10.1038/s41567-021-01451-5. URL `https://www.nature.com/articles/s41567-021-01451-5`.

[11] Qiangwei Yin, Zhijun Tu, Chunsheng Gong, Yang Fu, Shaohua Yan, and Hechang Lei. Superconductivity and Normal-State Properties of Kagome Metal $\mathrm{RbV_3Sb_5}$ Single Crystals. *Chinese Phys. Lett.*, 38(3):037403, March 2021. ISSN 0256-307X, 1741-3540. doi: 10.1088/0256-307X/38/3/037403. URL `https://iopscience.iop.org/article/10.1088/0256-307X/38/3/037403`.

[12] Brenden R. Ortiz, Paul M. Sarte, Eric M. Kenney, Michael J. Graf, Samuel M. L. Teicher, Ram Seshadri, and Stephen D. Wilson. Superconductivity in the $\mathbb{Z}_2$ kagome metal $\mathrm{KV_3Sb_5}$. *Phys. Rev. Materials*, 5(3):034801, March 2021. ISSN 2475-9953. doi: 10.1103/PhysRevMaterials.5.034801. URL `https://link.aps.org/doi/10.1103/PhysRevMaterials.5.034801`.

[13] Morten H. Christensen, Turan Birol, Brian M. Andersen, and Rafael M. Fernandes. Theory of the charge density wave in $\mathrm{AV_3Sb_5}$ kagome metals. *Phys. Rev. B*, 104(21): 214513, December 2021. ISSN 2469-9950, 2469-9969. doi: 10.1103/PhysRevB.104.214513. URL `https://link.aps.org/doi/10.1103/PhysRevB.104.214513`.

[14] Domenico Di Sante, Bongjae Kim, Werner Hanke, Cesare Franchini, Ronny Thomale, and Giorgio Sangiovanni. Electronic correlations and universal long-range scaling in kagome metals. 2022. doi: 10.48550/ARXIV.2203.05038. URL `https://arxiv.org/abs/2203.05038`. Publisher: arXiv Version Number: 1.

[15] Yuhao Gu, Yi Zhang, Xilin Feng, Kun Jiang, and Jiangping Hu. Gapless excitations inside the fully gapped kagome superconductors $\mathrm{AV_3Sb_5}$. *Phys. Rev. B*, 105(10): L100502, March 2022. ISSN 2469-9950, 2469-9969. doi: 10.1103/PhysRevB.105.L100502. URL `https://link.aps.org/doi/10.1103/PhysRevB.105.L100502`.

[16] Yu-Xiao Jiang, Jia-Xin Yin, M. Michael Denner, Nana Shumiya, Brenden R. Ortiz, Gang Xu, Zurab Guguchia, Junyi He, Md Shafayat Hossain, Xiaoxiong Liu, Jacob Ruff, Linus Kautzsch, Songtian S. Zhang, Guoqing Chang, Ilya Belopolski, Qi Zhang, Tyler A. Cochran, Daniel Multer, Maksim Litskevich, Zi-Jia Cheng, Xian P. Yang, Ziqiang Wang, Ronny Thomale, Titus Neupert, Stephen D. Wilson, and M. Zahid Hasan. Unconventional chiral charge order in kagome superconductor KV3Sb5. *Nat. Mater.*, 20(10):1353–1357, October 2021. ISSN 1476-1122, 1476-4660. doi: 10.1038/s41563-021-01034-y. URL `https://www.nature.com/articles/s41563-021-01034-y`.

[17] C. Mielke, D. Das, J.-X. Yin, H. Liu, R. Gupta, Y.-X. Jiang, M. Medarde, X. Wu, H. C. Lei, J. Chang, Pengcheng Dai, Q. Si, H. Miao, R. Thomale, T. Neupert, Y. Shi, R. Khasanov, M. Z. Hasan, H. Luetkens, and Z. Guguchia. Time-reversal symmetry-breaking charge order in a kagome superconductor. *Nature*, 602(7896):245–250, February 2022. ISSN 0028-0836, 1476-4687. doi: 10.1038/s41586-021-04327-z. URL `https://www.nature.com/articles/s41586-021-04327-z`.

[18] Brenden R. Ortiz, Samuel M. L. Teicher, Linus Kautzsch, Paul M. Sarte, Noah Ratcliff, John Harter, Jacob P. C. Ruff, Ram Seshadri, and Stephen D. Wilson. Fermi Surface Mapping and the Nature of Charge-Density-Wave Order in the Kagome Superconductor CsV_3sb_5. *Phys. Rev. X*, 11(4):041030, November 2021. ISSN 2160-3308. doi: 10.1103/PhysRevX.11.041030. URL `https://link.aps.org/doi/10.1103/PhysRevX.11.041030`.

[19] Hengxin Tan, Yizhou Liu, Ziqiang Wang, and Binghai Yan. Charge Density Waves and Electronic Properties of Superconducting Kagome Metals. *Phys. Rev. Lett.*, 127 (4):046401, July 2021. ISSN 0031-9007, 1079-7114. doi: 10.1103/PhysRevLett.127.046401. URL `https://link.aps.org/doi/10.1103/PhysRevLett.127.046401`.

[20] He Zhao, Hong Li, Brenden R. Ortiz, Samuel M. L. Teicher, Takamori Park, Mengxing Ye, Ziqiang Wang, Leon Balents, Stephen D. Wilson, and Ilija Zeljkovic. Cascade of correlated electron states in the kagome superconductor CsV_3Sb_5. *Nature*, 599(7884):216–221, November 2021. ISSN 0028-0836, 1476-4687. doi: 10.1038/s41586-021-03946-w. URL `https://www.nature.com/articles/s41586-021-03946-w`.

[21] Nana Shumiya, Md. Shafayat Hossain, Jia-Xin Yin, Yu-Xiao Jiang, Brenden R. Ortiz, Hongxiong Liu, Youguo Shi, Qiangwei Yin, Hechang Lei, Songtian S. Zhang, Guoqing Chang, Qi Zhang, Tyler A. Cochran, Daniel Multer, Maksim Litskevich, Zi-Jia Cheng, Xian P. Yang, Zurab Guguchia, Stephen D. Wilson, and M. Zahid Hasan. Intrinsic nature of chiral charge order in the kagome superconductor RbV_3Sb_5. *Phys. Rev. B*, 104(3):035131, July 2021. ISSN 2469-9950, 2469-9969. doi: 10.1103/PhysRevB.104.035131. URL `https://link.aps.org/doi/10.1103/PhysRevB.104.035131`.

[22] Soohyun Cho, Haiyang Ma, Wei Xia, Yichen Yang, Zhengtai Liu, Zhe Huang, Zhicheng Jiang, Xiangle Lu, Jishan Liu, Zhonghao Liu, Jun Li, Jinghui Wang, Yi Liu, Jinfeng Jia, Yanfeng Guo, Jianpeng Liu, and Dawei Shen. Emergence of New van Hove Singularities in the Charge Density Wave State of a Topological Kagome Metal RbV_3Sb_5. *Phys. Rev. Lett.*, 127(23):236401, December 2021. ISSN 0031-9007, 1079-7114. doi: 10.1103/PhysRevLett.127.236401. URL `https://link.aps.org/doi/10.1103/PhysRevLett.127.236401`.

[23] Francesco Ferrari, Federico Becca, and Roser Valentí. Charge-density waves in kagome-lattice extended Hubbard models at the van Hove filling. *arXiv:2204.10328 [cond-mat]*, April 2022. URL `http://arxiv.org/abs/2204.10328`. arXiv: 2204.10328.

[24] Z. Guguchia, C. Mielke, D. Das, R. Gupta, J. X. Yin, H. Liu, Q. Yin, M. H. Christensen, Z. Tu, C. Gong, N. Shumiya, Ts. Gamsakhurdashvili, M. Elender, Pengcheng Dai, A. Amato, Y. Shi, H. C. Lei, R. M. Fernandes, M. Z. Hasan, H. Luetkens, and R. Khasanov. Tunable nodal kagome superconductivity in charge ordered RbV_3Sb_5. 2022. doi: 10.48550/ARXIV.2202.07713. URL `https://arxiv.org/abs/2202.07713`. Publisher: arXiv Version Number: 1.

[25] Hong Li, He Zhao, Brenden R. Ortiz, Takamori Park, Mengxing Ye, Leon Balents, Ziqiang Wang, Stephen D. Wilson, and Ilija Zeljkovic. Rotation symmetry breaking in the normal state of a kagome superconductor KV_3Sb_5. *Nat. Phys.*, 18(3):265–270, March 2022. ISSN 1745-2473, 1745-2481. doi: 10.1038/s41567-021-01479-7. URL `https://www.nature.com/articles/s41567-021-01479-7`.

[26] Haoxiang Li, Yu-Xiao Jiang, J. X. Yin, Sangmoon Yoon, Andrew R. Lupini, Y. Pai, C. Nelson, A. Said, Y. M. Yang, Q. W. Yin, C. S. Gong, Z. J. Tu, H. C. Lei, Binghai Yan, Ziqiang Wang, M. Z. Hasan, H. N. Lee, and H. Miao. Spatial symmetry constraint of charge-ordered kagome superconductor CsV_3Sb_5. *arXiv:2109.03418 [cond-mat]*, September 2021. URL `http://arxiv.org/abs/2109.03418`. arXiv: 2109.03418.

[27] Li Yu, Chennan Wang, Yuhang Zhang, Mathias Sander, Shunli Ni, Zouyouwei Lu, Sheng Ma, Zhengguo Wang, Zhen Zhao, Hui Chen, Kun Jiang, Yan Zhang, Haitao Yang, Fang Zhou, Xiaoli Dong, Steven L. Johnson, Michael J. Graf, Jiangping Hu, Hong-Jun Gao, and Zhongxian Zhao. Evidence of a hidden flux phase in the topological kagome metal CsV_3Sb_5. *arXiv:2107.10714 [cond-mat]*, July 2021. URL `http://arxiv.org/abs/2107.10714`. arXiv: 2107.10714.

[28] Noah Ratcliff, Lily Hallett, Brenden R. Ortiz, Stephen D. Wilson, and John W. Harter. Coherent phonon spectroscopy and interlayer modulation of charge density wave order in the kagome metal CsV_3Sb_5. *Phys. Rev. Materials*, 5(11):L111801, November 2021. ISSN 2475-9953. doi: 10.1103/PhysRevMaterials.5.L111801. URL `https://link.aps.org/doi/10.1103/PhysRevMaterials.5.L111801`.

[29] Takamori Park, Mengxing Ye, and Leon Balents. Electronic instabilities of kagome metals: Saddle points and Landau theory. *Phys. Rev. B*, 104(3):035142, July 2021. ISSN 2469-9950, 2469-9969. doi: 10.1103/PhysRevB.104.035142. URL `https://link.aps.org/doi/10.1103/PhysRevB.104.035142`.

[30] H. Miao, H. X. Li, W. R. Meier, A. Huon, H. N. Lee, A. Said, H. C. Lei, B. R. Ortiz, S. D. Wilson, J. X. Yin, M. Z. Hasan, Ziqiang Wang, Hengxin Tan, and Binghai Yan. Geometry of the charge density wave in the kagome metal AV_3sb_5. *Phys. Rev. B*, 104 (19):195132, November 2021. ISSN 2469-9950, 2469-9969. doi: 10.1103/PhysRevB.104.195132. URL `https://link.aps.org/doi/10.1103/PhysRevB.104.195132`.

[31] Yishuai Xu, Zhuoliang Ni, Yizhou Liu, Brenden R. Ortiz, Stephen D. Wilson, Binghai Yan, Leon Balents, and Liang Wu. Universal three-state nematicity and magneto-optical Kerr effect in the charge density waves in AV_3Sb_5 (A=Cs, Rb, K). *arXiv:2204.10116 [cond-mat]*, April 2022. URL `http://arxiv.org/abs/2204.10116`. arXiv: 2204.10116.

[32] Shangfei Wu, Brenden R. Ortiz, Hengxin Tan, Stephen D. Wilson, Binghai Yan, Turan Birol, and Girsh Blumberg. Charge density wave order in the kagome metal AV_3Sb_5 (A = Cs , Rb , K). *Phys. Rev. B*, 105(15):155106, April 2022. ISSN 2469-9950, 2469-9969. doi: 10.1103/PhysRevB.105.155106. URL `https://link.aps.org/doi/10.1103/PhysRevB.105.155106`.

[33] Rustem Khasanov, Debarchan Das, Ritu Gupta, Charles Mielke, Matthias Elender, Qiangwei Yin, Zhijun Tu, Chunsheng Gong, Hechang Lei, Ethan Ritz, Rafael M. Fernandes, Turan Birol, Zurab Guguchia, and Hubertus Luetkens. Charge order

breaks time-reversal symmetry in CsV_3Sb_5. 2022. doi: 10.48550/ARXIV.2203.12317. URL `https://arxiv.org/abs/2203.12317`. Publisher: arXiv Version Number: 1.

[34] Eric M Kenney, Brenden R Ortiz, Chennan Wang, Stephen D Wilson, and Michael J Graf. Absence of local moments in the kagome metal KV_3Sb_5 as determined by muon spin spectroscopy. *J. Phys.: Condens. Matter*, 33(23):235801, June 2021. ISSN 0953-8984, 1361-648X. doi: 10.1088/1361-648X/abe8f9. URL `https://iopscience.iop.org/article/10.1088/1361-648X/abe8f9`.

[35] Haoxiang Li, T. T. Zhang, T. Yilmaz, Y. Y. Pai, C. E. Marvinney, A. Said, Q. W. Yin, C. S. Gong, Z. J. Tu, E. Vescovo, C. S. Nelson, R. G. Moore, S. Murakami, H. C. Lei, H. N. Lee, B. J. Lawrie, and H. Miao. Observation of Unconventional Charge Density Wave without Acoustic Phonon Anomaly in Kagome Superconductors A V 3 Sb 5 (A = Rb , Cs). *Phys. Rev. X*, 11(3):031050, September 2021. ISSN 2160-3308. doi: 10.1103/PhysRevX.11.031050. URL `https://link.aps.org/doi/10.1103/PhysRevX.11.031050`.

[36] David Vanderbilt. *Berry Phases in Electronic Structure Theory: Electric Polarization, Orbital Magnetization and Topological Insulators.* Cambridge University Press, 1 edition, October 2018. ISBN 978-1-316-66220-5 978-1-107-15765-1. doi: 10.1017/9781316662205. URL `https://www.cambridge.org/core/product/identifier/9781316662205/type/book`.

[37] Kun Jiang, Tao Wu, Jia-Xin Yin, Zhenyu Wang, M. Zahid Hasan, Stephen D. Wilson, Xianhui Chen, and Jiangping Hu. Kagome superconductors AV_3Sb_5 (A=K, Rb, Cs). 2021. doi: 10.48550/ARXIV.2109.10809. URL `https://arxiv.org/abs/2109.10809`. Publisher: arXiv Version Number: 1.

[38] Tomonari Mizoguchi and Masafumi Udagawa. Flat-band engineering in tight-binding models: Beyond the nearest-neighbor hopping. *Phys. Rev. B*, 99(23):235118, June 2019. ISSN 2469-9950, 2469-9969. doi: 10.1103/PhysRevB.99.235118. URL `https://link.aps.org/doi/10.1103/PhysRevB.99.235118`.

[39] Michael Hermele, Ying Ran, Patrick A. Lee, and Xiao-Gang Wen. Properties of an algebraic spin liquid on the kagome lattice. *Phys. Rev. B*, 77(22):224413, June 2008. ISSN 1098-0121, 1550-235X. doi: 10.1103/PhysRevB.77.224413. URL `https://link.aps.org/doi/10.1103/PhysRevB.77.224413`.

[40] Thierry Giamarchi, Anibal Iucci, and Christophe Berthod. *Introduction to Many Body Physics.* University of Geneva, 2013. URL `https://giamarchi.unige.ch/wp-content/php_code/people/thierry.giamarchi/pdf/many-body.pdf`.

[41] Maximilian L. Kiesel and Ronny Thomale. Sublattice interference in the kagome Hubbard model. *Phys. Rev. B*, 86(12):121105, September 2012. ISSN 1098-0121, 1550-235X. doi: 10.1103/PhysRevB.86.121105. URL `https://link.aps.org/doi/10.1103/PhysRevB.86.121105`.

[42] John Hubbard. Electron correlations in narrow energy bands. *Proc. R. Soc. Lond. A*, 276(1365):238–257, November 1963. ISSN 0080-4630, 2053-9169. doi: 10.1098/rspa.1963.0204. URL `https://royalsocietypublishing.org/doi/10.1098/rspa.1963.0204`.

[43] Henrik Bruus and Karsten Flensberg. *Many-body quantum theory in condensed matter physics: an introduction*. Oxford graduate texts. Oxford University Press, Oxford ; New York, 2004. ISBN 978-0-19-856633-5. OCLC: ocm56694794.

[44] A. M. Oleś. Antiferromagnetism and correlation of electrons in transition metals. *Phys. Rev. B*, 28(1):327–339, July 1983. ISSN 0163-1829. doi: 10.1103/PhysRevB.28.327. URL `https://link.aps.org/doi/10.1103/PhysRevB.28.327`.

Appendix A

Mean field decoupling for 3 band model

We can relate this field to its complex conjugate

$$\begin{aligned}\left(\Delta^{\alpha\sigma\beta\sigma'}_{\mathbf{q},s}\right)^* &= \sum_{\mathbf{k}} e^{-i(s-1)(\mathbf{k}+\mathbf{q})\cdot\mathbf{a}_{\alpha\beta}} \left\langle c^\dagger_{\mathbf{k}+\mathbf{q}\beta\sigma'} c_{\mathbf{k}\alpha\sigma}\right\rangle = \sum_{\mathbf{k}} e^{i(s-1)\mathbf{k}\cdot\mathbf{a}_{\beta\alpha}} \left\langle c^\dagger_{\mathbf{k}\beta\sigma'} c_{\mathbf{k}+\mathbf{q}\alpha\sigma}\right\rangle \\ &= e^{i(1-s)\mathbf{q}\cdot\mathbf{a}_{\beta\alpha}} \Delta^{\beta\sigma'\alpha\sigma}_{\mathbf{q},s}\end{aligned} \tag{A.1}$$

We can also see what evaluate $\Delta^{\alpha\sigma\beta\sigma'}_{\mathbf{q}+\mathbf{G},s}$. First we note that $\Delta^{\alpha\sigma\beta\varsigma}_{\mathbf{q}+\mathbf{G},+} = \Delta^{\alpha\sigma\beta\sigma}_{\mathbf{q},+}$ as can be seen from the gauge we have chosen. If we instead consider the case where $s = -$

$$\Delta^{\alpha\sigma\beta\sigma'}_{\mathbf{q}+\mathbf{G},-} = \sum_{\mathbf{k}} e^{-2i(\mathbf{k}+\mathbf{q}+\mathbf{G})\cdot\mathbf{a}_{\alpha\beta}} \left\langle c^\dagger_{\mathbf{k}\alpha\sigma} c_{\mathbf{k}+\mathbf{q}\beta\sigma'}\right\rangle = e^{-i\mathbf{G}\cdot 2\mathbf{a}_{\alpha\beta}} \Delta^{\alpha\sigma\beta\sigma}_{\mathbf{q},-}, \tag{A.2}$$

however as the $2\mathbf{a}_{\alpha\beta}$ is a lattice vector, we can conclude in general that $\Delta^{\alpha\sigma\beta\sigma'}_{\mathbf{q}+\mathbf{G},s} = \Delta^{\alpha\sigma\beta\sigma'}_{\mathbf{q},s}$.

We use this expression to write the Hubbard interaction in the Mean field approximation,

$$H_U^{\mathrm{MF}} = \frac{U}{N} \sum_{\mathbf{q}\mathbf{k}\mathbf{k}'} \sum_{\alpha\sigma} \left(c^\dagger_{\mathbf{k}\alpha\sigma} c_{\mathbf{k}+\mathbf{q}\alpha\sigma} \left\langle c^\dagger_{\mathbf{k}'\alpha\bar{\sigma}} c_{\mathbf{k}'-\mathbf{q}\alpha\bar{\sigma}} \right\rangle - c^\dagger_{\mathbf{k}\alpha\sigma} c_{\mathbf{k}'-\mathbf{q}\beta\bar{\sigma}} \left\langle c^\dagger_{\mathbf{k}'\alpha\bar{\sigma}} c_{\mathbf{k}+\mathbf{q}\alpha\sigma} \right\rangle \right), \tag{A.3}$$

where we have compacted the notation to a sum over spins, which is allowed due to the summation over $\mathbf{q}$. We will split the Hamiltonian into its two parts, such that the terms diagonal in spin are grouped together $H_U^{\mathrm{MF}} = \frac{U}{\sqrt{N}} \sum_\sigma H_U^{\sigma\sigma} - H_U^{\sigma\bar{\sigma}}$. Starting with the term diagonal in spin, this can rewritten in terms of the mean fields

$$H_U^{\sigma\sigma} = \sum_{\mathbf{k}\mathbf{q}\alpha} \Delta^{\alpha\bar{\sigma}\alpha\bar{\sigma}}_{-\mathbf{q},+} c^\dagger_{\mathbf{k}\alpha\sigma} c_{\mathbf{k}+\mathbf{q}\alpha\sigma} = \sum_{\mathbf{k}\mathbf{q}\alpha\sigma} \Delta^{\alpha\bar{\sigma}\alpha\bar{\sigma}}_{\mathbf{q},+} c^\dagger_{\mathbf{k}\alpha\sigma} c_{\mathbf{k}+\mathbf{q}\alpha\sigma}, \tag{A.4}$$

where we used $\Delta^{\alpha\sigma\beta\sigma'}_{-\mathbf{q},+} = \Delta^{\alpha\sigma\beta\sigma'}_{\mathbf{q},+}$. We will now impose the constraint that only certain mean fields are allowed under the assumption that phases breaks translational symmetry at most by 2 by 2 unit cells, and write out the sum over $\mathbf{q}$ more explicitly

$$H_U^{\sigma\sigma} = \sum_{\mathbf{k}\alpha} \left[\Delta^{\alpha\bar{\sigma}\alpha\bar{\sigma}}_{\mathbf{0},+} c^\dagger_{\mathbf{k}\alpha\sigma} c_{\mathbf{k}\alpha\sigma} + \sum_j \Delta^{\alpha\bar{\sigma}\alpha\bar{\sigma}}_{\mathbf{M}_j,+} c^\dagger_{\mathbf{k}\alpha\sigma} c_{\mathbf{k}+\mathbf{M}_j\alpha\sigma} \right] \tag{A.5}$$

We will now only consider the reduced Brillouin zone, hence splitting the sum over $\mathbf{k}$ up as described in Eq. (3.13)

$$H_U^{\sigma\sigma} = \sum_{\mathbf{k}\in\mathrm{RBZ},\alpha} \left[\Delta_{\mathbf{0},+}^{\alpha\overline{\sigma}\alpha\overline{\sigma}} \left(c_{\mathbf{k}\alpha\sigma}^{\dagger} c_{\mathbf{k}\alpha\sigma} + \sum_i c_{\mathbf{k}+\mathbf{M}_i\alpha\sigma}^{\dagger} c_{\mathbf{k}+\mathbf{M}_i\alpha\sigma} \right) + \right. \tag{A.6}$$
$$\left. \sum_j \Delta_{\mathbf{M}_j,+}^{\alpha\overline{\sigma}\alpha\overline{\sigma}} \left(c_{\mathbf{k}\alpha\sigma}^{\dagger} c_{\mathbf{k}+\mathbf{M}_j\alpha\sigma} + c_{\mathbf{k}+\mathbf{M}_j\alpha\sigma}^{\dagger} c_{\mathbf{k}\alpha\sigma} + \sum_{i\neq j} c_{\mathbf{k}+\mathbf{M}_i\alpha\sigma}^{\dagger} c_{\mathbf{k}+\mathbf{M}_l\alpha\sigma} \right) \right],$$

with $\mathbf{M}_l = -\mathbf{M}_i - \mathbf{M}_j$.We thus have the explicit terms for the Hamiltonian in the basis which we use.
We can now do the same procedure with the term from the mean field Hubbard interaction not diagonal in spin. First we will make a change in the index letting $\mathbf{q} \to \mathbf{k}' - \mathbf{k} - \mathbf{q}$, which enables us to use write it in terms of the mean fields

$$H_U^{\sigma\overline{\sigma}} = \sum_{\mathbf{kq}\alpha} \Delta_{\mathbf{q}+}^{\alpha\overline{\sigma}\alpha\sigma} c_{\mathbf{k}\alpha\sigma}^{\dagger} c_{\mathbf{k}+\mathbf{q}\alpha\overline{\sigma}}, \tag{A.7}$$

where we again used $\Delta_{-\mathbf{q},+}^{\alpha\sigma\beta\sigma'} = \Delta_{\mathbf{q},+}^{\alpha\sigma\beta\sigma'}$. We now write out the sum over $\mathbf{q}$ using that only specific momenta are allowed, and write the sum over $\mathbf{k}$ out using Eq. (3.13), thus obtaining this part of the Hamiltonian in the basis

$$H_U^{\sigma\overline{\sigma}} = \sum_{\mathbf{k}\in\mathrm{RBZ},\alpha} \left[\Delta_{\mathbf{0},+}^{\alpha\overline{\sigma}\alpha\sigma} \left(c_{\mathbf{k}\alpha\overline{\sigma}}^{\dagger} c_{\mathbf{k}\alpha\overline{\sigma}} + \sum_i c_{\mathbf{k}+\mathbf{M}_i\alpha\sigma}^{\dagger} c_{\mathbf{k}+\mathbf{M}_i\alpha\overline{\sigma}} \right) + \right.$$
$$\left. \sum_j \Delta_{\mathbf{M}_j,+}^{\alpha\overline{\sigma}\alpha\sigma} \left(c_{\mathbf{k}\alpha\overline{\sigma}}^{\dagger} c_{\mathbf{k}+\mathbf{M}_j\alpha\sigma} + c_{\mathbf{k}+\mathbf{M}_j\alpha\sigma}^{\dagger} c_{\mathbf{k}\alpha\overline{\sigma}} + \sum_{i\neq j} c_{\mathbf{k}+\mathbf{M}_i\alpha\sigma}^{\dagger} c_{\mathbf{k}+\mathbf{M}_l\alpha\overline{\sigma}} \right) \right]. \tag{A.8}$$

We now turn to the nearest neighbor interaction. We start by using the mean field decoupling given in Eq. (4.2)

$$H_V^{\mathrm{MF}} = \frac{V}{N} \sum_{\mathbf{qk}'} \sum_{\substack{\alpha\sigma\sigma' \\ \beta\neq\alpha}} \left(1 + e^{2i\mathbf{q}\cdot\mathbf{a}_{\alpha\beta}}\right) \left(c_{\mathbf{k}\alpha\sigma}^{\dagger} c_{\mathbf{k}+\mathbf{q}\alpha\sigma} \left\langle c_{\mathbf{k}'\beta\sigma'}^{\dagger} c_{\mathbf{k}'-\mathbf{q}\beta\sigma'} \right\rangle - c_{\mathbf{k}'\beta\sigma'}^{\dagger} c_{\mathbf{k}+\mathbf{q}\alpha\sigma} \left\langle c_{\mathbf{k}\alpha\sigma}^{\dagger} c_{\mathbf{k}'-\mathbf{q}\beta\sigma'} \right\rangle \right). \tag{A.9}$$

We again split this up into two parts. We will again split it up into the two components, an Hatree part H_V^{H} and a Fock part H_V^{F}, such that $H_V^{\mathrm{MF}} = \frac{V}{\sqrt{N}} \sum_{\substack{\alpha\sigma\sigma' \\ \beta\neq\alpha}} (H_V^{\mathrm{H}} - H_V^{\mathrm{F}})$. Starting with the on site terms, writing it in terms of the mean fields

$$H_V^{\mathrm{H}} = \sum_{\mathbf{kq}} \left(1 + e^{2i\mathbf{q}\cdot\mathbf{a}_{\alpha\beta}}\right) \Delta_{\mathbf{q},+}^{\beta\sigma'\beta\sigma'} c_{\mathbf{k}\alpha\sigma}^{\dagger} c_{\mathbf{k}+\mathbf{q}\alpha\sigma}. \tag{A.10}$$

Now writing out the sum over $\mathbf{q}$ and $\mathbf{k}$ into their respective parts, yield the on site part of the mean field decoupled nearest neighbour interaction in the basis we use

$$H_V^{\mathrm{H}} = \sum_{\mathbf{k}\in\mathrm{RBZ}} \left[2\Delta_{\mathbf{0}}^{\beta\sigma'\beta\sigma'} \left(c_{\mathbf{k}\alpha\sigma}^{\dagger} c_{\mathbf{k}\alpha\sigma} + \sum_i c_{\mathbf{k}+\mathbf{M}_i\alpha\sigma}^{\dagger} c_{\mathbf{k}+\mathbf{M}_i\alpha\sigma} \right) + \right. \tag{A.11}$$
$$\left. \sum_j \left(1 + e^{2i\mathbf{M}_j\cdot\mathbf{a}_{\alpha\beta}}\right) \Delta_{\mathbf{M}_j}^{\beta\sigma'\beta\sigma'} \left(c_{\mathbf{k}\beta}^{\dagger} c_{\mathbf{k}+\mathbf{M}_j\alpha\sigma} + c_{\mathbf{k}+\mathbf{M}_j\alpha\sigma}^{\dagger} c_{\mathbf{k}\alpha\sigma} + \sum_{i\neq j} c_{\mathbf{k}+\mathbf{M}_i\alpha\sigma}^{\dagger} c_{\mathbf{k}+\mathbf{M}_l\alpha\sigma} \right) \right].$$

The Fock terms of the nearest neighbour interaction need the transformation $\mathbf{q} \to \mathbf{q}+\mathbf{k}'-\mathbf{k}$, before we can write it in terms of the mean fields. Then we obtain

$$H_V^{\mathrm{F}} = \frac{1}{\sqrt{N}} \sum_{\mathbf{kqk}'} \left(1 + e^{-2i(\mathbf{k}-\mathbf{q}-\mathbf{k}')\cdot\mathbf{a}_{\alpha\beta}}\right) c^\dagger_{\mathbf{k}'\beta\sigma'} c_{\mathbf{k}'+\mathbf{q}\alpha\sigma} \left\langle c^\dagger_{\mathbf{k}\alpha\sigma} c_{\mathbf{k}-\mathbf{q}\beta\sigma'} \right\rangle . \tag{A.12}$$

We can now use the definition of the mean fields Eq. (4.15) to rewrite this expression using the mean fields

$$H_V^{\mathrm{F}} = \sum_{\mathbf{kq}} \left(\Delta^{\alpha\sigma\beta\sigma'}_{\mathbf{q},+} + \Delta^{\alpha\sigma\beta\sigma'}_{-\mathbf{q},-} e^{2i\mathbf{k}\cdot\mathbf{a}_{\alpha\beta}}\right) c^\dagger_{\mathbf{k}\beta\sigma'} c_{\mathbf{k}+\mathbf{q}\alpha\sigma} \tag{A.13}$$

We now write out the sum over $\mathbf{k}$ into its four parts, and we write out the sum over $\mathbf{q}$, using, that $\Delta^{\alpha\sigma\beta\sigma'}_{-\mathbf{q},-} = \Delta^{\alpha\sigma\beta\sigma'}_{\mathbf{G}-\mathbf{q},-}$ for any reciprocal lattice vector. The Fock terms become

$$\begin{aligned} H_V^{\mathrm{F}} = \sum_{\mathbf{k}\in\mathrm{RBZ}} \Bigg\{ & \left(\Delta^{\alpha\sigma\beta\sigma'}_{\mathbf{0},+} + e^{2i\mathbf{k}\cdot\mathbf{a}_{\alpha\beta}} \Delta^{\alpha\sigma\beta\sigma'}_{\mathbf{0},-}\right) c^\dagger_{\mathbf{k}\beta\sigma'} c_{\mathbf{k}\alpha\sigma} \\ & + \sum_i \left(\Delta^{\alpha\sigma\beta\sigma'}_{\mathbf{0}+} + e^{2i(\mathbf{k}+\mathbf{M}_i)\cdot\mathbf{a}_{\alpha\beta}} \Delta^{\alpha\sigma\beta\sigma'}_{\mathbf{0}-}\right) c^\dagger_{\mathbf{k}+\mathbf{M}_i\beta\sigma'} c_{\mathbf{k}+\mathbf{M}_i\alpha\sigma} \\ & + \sum_j \Bigg[\left(\Delta^{\alpha\sigma\beta\sigma'}_{\mathbf{M}_j+} + e^{2i\mathbf{k}\cdot\mathbf{a}_{\alpha\beta}} \Delta^{\alpha\sigma\beta\sigma'}_{\mathbf{M}_j-}\right) c^\dagger_{\mathbf{k}\beta\sigma'} c_{\mathbf{k}+\mathbf{M}_j\alpha\sigma} \\ & + \left(\Delta^{\alpha\sigma\beta\sigma'}_{\mathbf{M}_j+} + e^{2i(\mathbf{k}+\mathbf{M}_j)\cdot\mathbf{a}_{\alpha\beta}} \Delta^{\alpha\sigma\beta\sigma'}_{\mathbf{M}_j-}\right) c^\dagger_{\mathbf{k}+\mathbf{M}_j\beta\sigma'} c_{\mathbf{k}\alpha\sigma} \\ & + \sum_{i\neq j} \left(\Delta^{\alpha\sigma\beta\sigma'}_{\mathbf{M}_j+} + e^{2i(\mathbf{k}+\mathbf{M}_i)\cdot\mathbf{a}_{\alpha\beta}} \Delta^{\alpha\sigma\beta\sigma'}_{\mathbf{M}_j-}\right) c^\dagger_{\mathbf{k}+\mathbf{M}_i\beta\sigma'} c_{\mathbf{k}+\mathbf{M}_l\alpha\sigma} \Bigg] \Bigg\} . \end{aligned} \tag{A.14}$$

Now combining eqs. (BLA) we now have the mean field part of the Hamiltonian. We will now consider the correction to the energies from the mean field decoupling. Starting with the correction from the Hubbard interaction

$$E^U_{\mathrm{crxn}} = -\frac{U}{N} \sum_{\mathbf{kk}'\mathbf{q}\alpha} \left(\left\langle c^\dagger_{\mathbf{k}'\alpha\downarrow} c_{\mathbf{k}'-\mathbf{q}\alpha\downarrow} \right\rangle \left\langle c^\dagger_{\mathbf{k}\alpha\uparrow} c_{\mathbf{k}+\mathbf{q}\alpha\uparrow} \right\rangle - \left\langle c^\dagger_{\mathbf{k}'\alpha\downarrow} c_{\mathbf{k}+\mathbf{q}\alpha\uparrow} \right\rangle \left\langle c^\dagger_{\mathbf{k}\alpha\uparrow} c_{\mathbf{k}'-\mathbf{q}\alpha\downarrow} \right\rangle \right) \tag{A.15}$$

Where the first term is easily rewritten in terms of the mean fields, the second term need a reindexing first. Letting $\mathbf{q} \to \mathbf{k}' - \mathbf{k} + \mathbf{q}$ for the second term in the sum only we rewrite this as

$$E^U_{\mathrm{crxn}} = -U \sum_{\mathbf{q}\alpha} \left(\Delta^{\alpha\uparrow\alpha\uparrow}_{\mathbf{q},+} \Delta^{\alpha\downarrow\alpha\downarrow}_{-\mathbf{q},+} - \Delta^{\alpha\downarrow\alpha\uparrow}_{\mathbf{q},+} \Delta^{\alpha\uparrow\alpha\downarrow}_{-\mathbf{q},+} \right) = -U \sum_{\mathbf{q}\alpha} \left(\Delta^{\alpha\uparrow\alpha\uparrow}_{\mathbf{q},+} \Delta^{\alpha\downarrow\alpha\downarrow}_{\mathbf{q},+} - \Delta^{\alpha\downarrow\alpha\uparrow}_{\mathbf{q},+} \Delta^{\alpha\uparrow\alpha\downarrow}_{\mathbf{q},+} \right) , \tag{A.16}$$

where we in the last term made use of the fact that $2\mathbf{q}$ is a reciprocal lattice vector, thus Eq. (A.2) could be used.

The correction from the nearest neighbour interaction can also be written up

$$\begin{aligned} E^V_{\mathrm{crxn}} = -V \sum_{\substack{\mathbf{kk}'\mathbf{q} \\ \alpha\sigma\sigma' \\ \beta>\alpha}} \left(1 + e^{2i\mathbf{q}\cdot\mathbf{a}_{\alpha\beta}}\right) \Big(& \left\langle c^\dagger_{\mathbf{k}'\beta\sigma'} c_{\mathbf{k}'-\mathbf{q}\beta\sigma} \right\rangle \left\langle c^\dagger_{\mathbf{k}\alpha\sigma} c_{\mathbf{k}+\mathbf{q}\alpha\sigma} \right\rangle \\ & - \left\langle c^\dagger_{\mathbf{k}'\beta\sigma'} c_{\mathbf{k}+\mathbf{q}\alpha\sigma} \right\rangle \left\langle c^\dagger_{\mathbf{k}\alpha\sigma} c_{\mathbf{k}'-\mathbf{q}\beta\sigma'} \right\rangle \Big) . \end{aligned} \tag{A.17}$$

The two first terms are again written out as sums mean fields directly, whereas the second term need the same reindexing as before.

$$\begin{aligned}
E^V_{\text{crxn}} &= -V \sum_{\substack{\mathbf{q}\sigma\sigma' \\ \alpha\beta>\alpha}} \Bigg[\left(1 + e^{2i\mathbf{q}\cdot\mathbf{a}_{\alpha\beta}}\right) \Delta^{\beta\sigma'\beta\sigma'}_{\mathbf{q},+} \Delta^{\alpha\sigma\alpha\sigma}_{\mathbf{q},+} - \Delta^{\alpha\sigma\beta\sigma'}_{\mathbf{q},+} \Delta^{\beta\sigma'\alpha\sigma}_{\mathbf{q},+} \\
&\qquad - \sum_{\mathbf{k}\mathbf{k}'} e^{-2i(\mathbf{q}+\mathbf{k}')\cdot\mathbf{a}_{\beta\alpha}} e^{-2i\mathbf{k}\cdot\mathbf{a}_{\alpha\beta}} \left\langle c^\dagger_{\mathbf{k}'\beta\sigma'} c_{\mathbf{k}'+\mathbf{q}\alpha\sigma} \right\rangle \left\langle c^\dagger_{\mathbf{k}\alpha\sigma} c_{\mathbf{k}-\mathbf{q}\beta\sigma'} \right\rangle \Bigg] \qquad \text{(A.18)} \\
&= -V \sum_{\substack{\mathbf{q}\sigma\sigma' \\ \alpha\beta>\alpha}} \left[\left(1 + e^{2i\mathbf{q}\cdot\mathbf{a}_{\alpha\beta}}\right) \Delta^{\beta\sigma'\beta\sigma'}_{\mathbf{q},+} \Delta^{\alpha\sigma\alpha\sigma}_{\mathbf{q},+} - \Delta^{\alpha\sigma\beta\sigma'}_{\mathbf{q},+} \Delta^{\beta\sigma'\alpha\sigma}_{\mathbf{q},+} - e^{2i\mathbf{q}\cdot\mathbf{a}_{\alpha\beta}} \Delta^{\beta\sigma'\alpha\sigma}_{\mathbf{q},-} \Delta^{\alpha\sigma\beta\sigma}_{\mathbf{q},-} \right].
\end{aligned}$$

Appendix B

Seven band model

We recall the overall structure of the tight-binding Hamiltonian of the seven band model

$$H = \begin{pmatrix} H_{X^2-Y^2} & 0 & 0 \\ 0 & H_{\mathrm{Sb}} & V \\ 0 & V^\dagger & H_{YZ} \end{pmatrix}, \tag{B.1}$$

The Hamiltonian is written in the basis

$$\mathbf{c}^\dagger_{\mathbf{k}\sigma} = \left(c^\dagger_{\mathbf{k}A\,X^2-Y^2\sigma}, c^\dagger_{\mathbf{k}B\,X^2-Y^2\sigma}, c^\dagger_{\mathbf{k}C\,X^2-Y^2\sigma}, c^\dagger_{\mathbf{k}\mathrm{Sb}\sigma}, c^\dagger_{\mathbf{k}A\,YZ\sigma}, c^\dagger_{\mathbf{k}B\,YZ\sigma}, c^\dagger_{\mathbf{k}C\,YZ\sigma}\right) \tag{B.2}$$

We will below give the expression in the different parts of the Hamiltonian in turn, using the row-number and column-numbers to locate the entries. Only the necessary amount of entries are given, as the other entries can be found by complex conjugation. Starting with the expressions in $H_{X^2-Y^2}$

$$H_{11} = \varepsilon_{\mathrm{V}}^{X^2-Y^2} + 2t_{\mathrm{TNN}}^{X^2-Y^2,1}\cos(\mathbf{k}\cdot(\mathbf{t}_1+\mathbf{t}_2)) + 2t_{\mathrm{TNN}}^{X^2-Y^2,2}\left[\cos(\mathbf{k}\cdot\mathbf{t}_1)+\cos(\mathbf{k}\cdot\mathbf{t}_2)\right] \tag{B.3}$$

$$H_{22} = \varepsilon_{\mathrm{V}}^{X^2-Y^2} + 2t_{\mathrm{TNN}}^{X^2-Y^2,1}\cos(\mathbf{k}\cdot\mathbf{t}_1) + 2t_{\mathrm{TNN}}^{X^2-Y^2,2}\left[\cos(\mathbf{k}\cdot\mathbf{t}_2)+\cos(\mathbf{k}\cdot(\mathbf{t}_1+\mathbf{t}_2))\right] \tag{B.4}$$

$$H_{33} = \varepsilon_{\mathrm{V}}^{X^2-Y^2} + 2t_{\mathrm{TNN}}^{X^2-Y^2,1}\cos(\mathbf{k}\cdot\mathbf{t}_2) + 2t_{\mathrm{TNN}}^{X^2-Y^2,2}\left[\cos(\mathbf{k}\cdot\mathbf{t}_1)+\cos(\mathbf{k}\cdot(\mathbf{t}_1+\mathbf{t}_2))\right] \tag{B.5}$$

$$H_{12} = 2t_{\mathrm{NN}}^{X^2-Y^2}\cos(\mathbf{k}\cdot\mathbf{a}_{AB}) + 2t_{\mathrm{SNN}}^{X^2-Y^2}\cos(\mathbf{k}\cdot(\mathbf{t}_1+\mathbf{a}_{AB})) \tag{B.6}$$

$$H_{13} = 2t_{\mathrm{NN}}^{X^2-Y^2}\cos(\mathbf{k}\cdot\mathbf{a}_{AC}) + 2t_{\mathrm{SNN}}^{X^2-Y^2}\cos(\mathbf{k}\cdot(\mathbf{t}_1+\mathbf{t}_2+\mathbf{a}_{AC})) \tag{B.7}$$

$$H_{23} = 2t_{\mathrm{NN}}^{X^2-Y^2}\cos(\mathbf{k}\cdot\mathbf{a}_{BC}) + 2t_{\mathrm{SNN}}^{X^2-Y^2}\cos(\mathbf{k}\cdot(\mathbf{t}_2+\mathbf{a}_{BC})). \tag{B.8}$$

We then give the expression of H_{Sb}

$$\begin{aligned} H_{44} = \varepsilon_{\mathrm{Sb}} &+ 2t_{\mathrm{NN}}^{\mathrm{Sb}}[\cos(\mathbf{k}\cdot\mathbf{t}_1)+\cos(\mathbf{k}\cdot(\mathbf{t}_1-\mathbf{t}_2))+\cos(\mathbf{k}\cdot\mathbf{t}_2)] \\ &+ 2t_{\mathrm{SNN}}^{\mathrm{Sb}}[\cos(\mathbf{k}\cdot(2\mathbf{t}_1-\mathbf{t}_2))+\cos(\mathbf{k}\cdot(\mathbf{t}_1+\mathbf{t}_2))+\cos(\mathbf{k}\cdot(2\mathbf{t}_2-\mathbf{t}_1))]. \end{aligned} \tag{B.9}$$

The expressions in H_{YZ} is also given

$$\begin{aligned}
H_{55} =& \varepsilon_{\mathrm{V}}^{YZ} + 2t_{\mathrm{TNN}}^{YZ,1} \cos(\mathbf{k} \cdot (\mathbf{t}_1 + \mathbf{t}_2)) + 2t_{\mathrm{TNN}}^{YZ,2} \left[\cos(\mathbf{k} \cdot \mathbf{t}_1) + \cos(\mathbf{k} \cdot \mathbf{t}_2)\right] && \text{(B.10)}\\
H_{66} =& \varepsilon_{\mathrm{V}}^{YZ} + 2t_{\mathrm{TNN}}^{YZ,1} \cos(\mathbf{k} \cdot \mathbf{t}_1) + 2t_{\mathrm{TNN}}^{YZ,2} \left[\cos(\mathbf{k} \cdot \mathbf{t}_2) + \cos(\mathbf{k} \cdot (\mathbf{t}_1 + \mathbf{t}_2))\right] && \text{(B.11)}\\
H_{77} =& \varepsilon_{\mathrm{V}}^{YZ} + 2t_{\mathrm{TNN}}^{YZ,1} \cos(\mathbf{k} \cdot \mathbf{t}_2) + 2t_{\mathrm{TNN}}^{YZ,2} \left[\cos(\mathbf{k} \cdot \mathbf{t}_1) + \cos(\mathbf{k} \cdot (\mathbf{t}_1 + \mathbf{t}_2))\right] && \text{(B.12)}\\
H_{56} =& 2t_{\mathrm{NN}}^{YZ} \cos(\mathbf{k} \cdot \mathbf{a}_{AB}) + 2t_{\mathrm{SNN}}^{YZ} \cos(\mathbf{k} \cdot (\mathbf{t}_1 + \mathbf{a}_{AB})) + 2t_{\mathrm{4thNN}}^{YZ} \left[\cos(\mathbf{k} \cdot (\mathbf{t}_1 - \mathbf{a}_{AB}))\right.\\
&\left. + \cos(\mathbf{k} \cdot (\mathbf{t}_1 + \mathbf{t}_2 + \mathbf{a}_{AB}))\right] + 2t_{\mathrm{5thNN}}^{YZ} \cos(\mathbf{k} \cdot (\mathbf{t}_2 + \mathbf{a}_{AB})) && \text{(B.13)}\\
H_{57} =& 2t_{\mathrm{NN}}^{YZ} \cos(\mathbf{k} \cdot \mathbf{a}_{AC}) + 2t_{\mathrm{SNN}}^{YZ} \cos(\mathbf{k} \cdot (\mathbf{t}_1 + \mathbf{t}_2 + \mathbf{a}_{AC})) + 2t_{\mathrm{4thNN}}^{YZ} \left[\cos(\mathbf{k} \cdot (\mathbf{t}_2 + \mathbf{a}_{AC}))\right.\\
&\left. + \cos(\mathbf{k} \cdot (\mathbf{t}_1 + \mathbf{t}_2 - \mathbf{a}_{AC}))\right] + 2t_{\mathrm{5thNN}}^{YZ} \cos(\mathbf{k} \cdot (\mathbf{t}_1 - \mathbf{a}_{AC})) && \text{(B.14)}\\
H_{67} =& 2t_{\mathrm{NN}}^{YZ} \cos(\mathbf{k} \cdot \mathbf{a}_{BC}) + 2t_{\mathrm{SNN}}^{YZ} \cos(\mathbf{k} \cdot (\mathbf{t}_2 + \mathbf{a}_{BC})) + 2t_{\mathrm{4thNN}}^{YZ} \left[\cos(\mathbf{k} \cdot (\mathbf{t}_1 - \mathbf{a}_{BC}))\right.\\
&\left. + \cos(\mathbf{k} \cdot (\mathbf{t}_2 + \mathbf{a}_{BC}))\right] + 2t_{\mathrm{5thNN}}^{YZ} \cos(\mathbf{k} \cdot (\mathbf{t}_1 + \mathbf{t}_2 - \mathbf{a}_{BC})). && \text{(B.15)}
\end{aligned}$$

Finally, the expressions in V are given

$$\begin{aligned}
H_{45} =& 2it_{\mathrm{NN}}^{\mathrm{Sb}\text{-}YZ} \sin(\mathbf{k} \cdot (\mathbf{t}_1 + \mathbf{t}_2)/2) && \text{(B.16)}\\
H_{46} =& -2it_{\mathrm{NN}}^{\mathrm{Sb}\text{-}YZ} \sin(\mathbf{k} \cdot \mathbf{t}_1/2) && \text{(B.17)}\\
H_{47} =& -2it_{\mathrm{NN}}^{\mathrm{Sb}\text{-}YZ} \sin(\mathbf{k} \cdot \mathbf{t}_2/2). && \text{(B.18)}
\end{aligned}$$

Below is a table with the numerical values for the parameters of the model. The gauge of the tight binding Hamiltonian is different from the choice made in this work. We perform a gauge transformation to the tight binding model, using the transformation

Table B.1: The values of the parameters given in eV for the 7-band model. Taken from REF.

$\varepsilon_{\mathrm{V}}^{X^2-Y^2}$	-0.0946	$\varepsilon_{\mathrm{V}}^{YZ}$	0.3619	$\varepsilon_{\mathrm{Sb}}$	0.8215
$t_{\mathrm{NN}}^{X^2-Y^2}$	-0.4661	t_{NN}^{YZ}	0.1112	$t_{\mathrm{NN}}^{\mathrm{Sb}}$	-0.1813
$t_{\mathrm{SNN}}^{X^2-Y^2}$	0.0278	t_{SNN}^{YZ}	-0.1168	$t_{\mathrm{SNN}}^{\mathrm{Sb}}$	-0.0204
$t_{\mathrm{TNN}}^{X^2-Y^2,1}$	-0.008	$t_{\mathrm{TNN}}^{YZ,1}$	0.0077	$t_{\mathrm{NN}}^{\mathrm{Sb}-YZ}$	-0.0071
$t_{\mathrm{TNN}}^{X^2-Y^2,2}$	-0.0091	$t_{\mathrm{TNN}}^{YZ,2}$	0.1315		
		t_{4thNN}^{YZ}	0.0356		
		t_{5thNN}^{YZ}	-0.0802		

$$U_{\alpha\beta}(\mathbf{k}) = \delta_{\alpha\beta} e^{i\mathbf{k}\cdot\mathbf{d}_\alpha}, \tag{B.19}$$

where α and β are the site with orbital entries, and $\mathbf{d}_{\mathrm{Sb}} = \begin{pmatrix} -\frac{1}{4} \\ \frac{\sqrt{3}}{4} \end{pmatrix}$.

Appendix C

Mean field decoupling of the 7 band model

Here are the detailed calculations giving the corrections and the interactions due to on site orbital interactions. Starting with the on site density-density interaction, we Fourier transform the interaction to momentum space yielding

$$H_{U'} = \frac{U}{2N} \sum_{\mathbf{q}\kappa\sigma\sigma'} n_{\mathbf{q}\kappa\sigma} n_{-\mathbf{q}\overline{\kappa}\sigma'}. \tag{C.1}$$

Using the mean field approximation on this interaction we obtain

$$\begin{aligned} H_{U'}^{\mathrm{MF}} = \frac{U}{2N} \sum_{\mathbf{q}\mathbf{k}'} \sum_{\kappa\sigma\sigma'} \Big(& \left\langle c^{\dagger}_{\mathbf{k}\kappa\sigma} c_{\mathbf{k}+\mathbf{q}\kappa\sigma} \right\rangle c^{\dagger}_{\mathbf{k}'\overline{\kappa}\sigma'} c_{\mathbf{k}'-\mathbf{q}\overline{\kappa}\sigma'} + \left\langle c^{\dagger}_{\mathbf{k}'\overline{\kappa}\sigma'} c_{\mathbf{k}'-\mathbf{q}\overline{\kappa}\sigma'} \right\rangle c^{\dagger}_{\mathbf{k}\kappa\sigma} c_{\mathbf{k}+\mathbf{q}\kappa\sigma} \\ & - \left\langle c^{\dagger}_{\mathbf{k}'\overline{\kappa}\sigma'} c_{\mathbf{k}+\mathbf{q}\kappa\sigma} \right\rangle c^{\dagger}_{\mathbf{k}\kappa\sigma} c_{\mathbf{k}'-\mathbf{q}\overline{\kappa}\sigma'} - \left\langle c^{\dagger}_{\mathbf{k}\kappa\sigma} c_{\mathbf{k}'-\mathbf{q}\overline{\kappa}\sigma'} \right\rangle c^{\dagger}_{\mathbf{k}'\overline{\kappa}\sigma'} c_{\mathbf{k}+\mathbf{q}\kappa\sigma} \Big). \end{aligned} \tag{C.2}$$

Upon close inspection the sum over the first two terms are the same as are the sum over the last two terms.

$$H_{U'}^{\mathrm{MF}} = \frac{U}{N} \sum_{\mathbf{q}\mathbf{k}'} \sum_{\kappa\sigma\sigma'} \left\langle c^{\dagger}_{\mathbf{k}\kappa\sigma} c_{\mathbf{k}+\mathbf{q}\kappa\sigma} \right\rangle c^{\dagger}_{\mathbf{k}'\overline{\kappa}\sigma'} c_{\mathbf{k}'-\mathbf{q}\overline{\kappa}\sigma'} - \left\langle c^{\dagger}_{\mathbf{k}\kappa\sigma} c_{\mathbf{k}'-\mathbf{q}\overline{\kappa}\sigma'} \right\rangle c^{\dagger}_{\mathbf{k}'\overline{\kappa}\sigma'} c_{\mathbf{k}+\mathbf{q}\kappa\sigma}. \tag{C.3}$$

By reindexing **q**, using the definitions of the mean fields in momentum space with knowledge that 2**q** is a reciprocal lattice vector under our assumptions, we obtain the expression in the text.

$$H_{U'}^{\mathrm{MF}} = \frac{U'}{\sqrt{N}} \sum_{\mathbf{q}\mathbf{k}} \sum_{\kappa\sigma\sigma'} \Delta^{\kappa\sigma\kappa\sigma}_{\mathbf{q}+} c^{\dagger}_{\mathbf{k}\overline{\kappa}\sigma'} c_{\mathbf{k}+\mathbf{q}\overline{\kappa}\sigma'} - \Delta^{\kappa\sigma\overline{\kappa}\sigma'}_{\mathbf{q}+} c^{\dagger}_{\mathbf{k}\overline{\kappa}\sigma'} c_{\mathbf{k}+\mathbf{q}\kappa\sigma}. \tag{C.4}$$

This is rewritten in the basis where we only consider momenta in the reduced Brillouin zone, starting with the Hartree term, only writing the sum over momentum vector

$$\begin{aligned} H_{U'}^{\mathrm{H}} = \sum_{\mathbf{k}\in\mathrm{RBZ}} \Bigg[& \Delta^{\kappa\sigma\kappa\sigma}_{\mathbf{0}} \left(c^{\dagger}_{\mathbf{k}\overline{\kappa}\sigma'} c_{\mathbf{k}\overline{\kappa}\sigma'} + \sum_{i} c^{\dagger}_{\mathbf{k}+\mathbf{M}_i\overline{\kappa}\sigma'} c_{\mathbf{k}+\mathbf{M}_i\overline{\kappa}\sigma'} \right) + \\ & \sum_{j} \Delta^{\kappa\sigma\kappa\sigma}_{\mathbf{M}_j} \left(c^{\dagger}_{\mathbf{k}+\mathbf{M}_j\overline{\kappa}\sigma'} c_{\mathbf{k}\overline{\kappa}\sigma'} + c^{\dagger}_{\mathbf{k}\overline{\kappa}\sigma'} c_{\mathbf{k}+\mathbf{M}_j\overline{\kappa}\sigma'} + \sum_{i\neq j} c^{\dagger}_{\mathbf{k}+\mathbf{M}_i\overline{\kappa}\sigma'} c_{\mathbf{k}+\mathbf{M}_i\overline{\kappa}\sigma'} \right) \Bigg]. \end{aligned} \tag{C.5}$$

Similarly, computations can be made for the Fock contribution

$$H^{\mathrm{F}}_{U'} = \sum_{\mathbf{k}\in\mathrm{RBZ}} \left[\Delta^{\kappa\sigma\bar{\kappa}\sigma'}_{\mathbf{0}+} \left(c^{\dagger}_{\mathbf{k}\bar{\kappa}\sigma'} c_{\mathbf{k}\kappa\sigma} + \sum_i c^{\dagger}_{\mathbf{k}+\mathbf{M}_i\bar{\kappa}\sigma'} c_{\mathbf{k}+\mathbf{M}_i\kappa\sigma} \right) + \right. \tag{C.6}$$

$$\left. \sum_j \Delta^{\kappa\sigma\bar{\kappa}\sigma'}_{\mathbf{M}_j} \left(c^{\dagger}_{\mathbf{k}+\mathbf{M}_j\bar{\kappa}\sigma'} c_{\mathbf{k}\kappa\sigma} + c^{\dagger}_{\mathbf{k}\bar{\kappa}\sigma'} c_{\mathbf{k}+\mathbf{M}_j\kappa\sigma} + \sum_{i\neq j} c^{\dagger}_{\mathbf{k}+\mathbf{M}_i\bar{\kappa}\sigma'} c_{\mathbf{k}+\mathbf{M}_i\kappa\sigma} \right) \right].$$

The correction to the energy is written out in terms of the mean fields

$$E^{\mathrm{crxn}}_{U'} = -\frac{U'}{2N} \sum_{\mathbf{q}\mathbf{k}\mathbf{k}'} \sum_{\kappa\sigma\sigma'} \left\langle c^{\dagger}_{\mathbf{k}\kappa\sigma} c_{\mathbf{k}+\mathbf{q}\kappa\sigma} \right\rangle \left\langle c^{\dagger}_{\mathbf{k}'\bar{\kappa}\sigma'} c_{\mathbf{k}'-\mathbf{q}\bar{\kappa}\sigma'} \right\rangle - \left\langle c^{\dagger}_{\mathbf{k}'\bar{\kappa}\sigma'} c_{\mathbf{k}+\mathbf{q}\kappa\sigma} \right\rangle \left\langle c^{\dagger}_{\mathbf{k}\kappa\sigma} c_{\mathbf{k}'-\mathbf{q}\bar{\kappa}\sigma'} \right\rangle, \tag{C.7}$$

and can be written using the mean fields by reindexing in the second term. Here we will also use that $2\mathbf{q}$ is a reciprocal lattice vector, thus we can change $-\mathbf{q}$ to $\mathbf{q}$.

$$E^{\mathrm{crxn}}_{U'} = -\frac{U'}{2} \sum_{\mathbf{q}\kappa\sigma\sigma'} \left(\Delta^{\kappa\sigma\kappa\sigma}_{\mathbf{q}+} \Delta^{\bar{\kappa}\sigma'\bar{\kappa}\sigma'}_{\mathbf{q}+} - \Delta^{\kappa\sigma\bar{\kappa}\sigma'}_{\mathbf{q}+} \Delta^{\bar{\kappa}\sigma'\kappa\sigma}_{\mathbf{q}+} \right). \tag{C.8}$$

Similar calculations are made for the Hund's coupling, writing in momentum space

$$H_J = -\frac{J}{2N} \sum_{\mathbf{q}\mathbf{k}\mathbf{k}'} \sum_{\kappa\sigma\sigma'} c^{\dagger}_{\mathbf{k}\kappa\sigma} c_{\mathbf{k}+\mathbf{q}\kappa\sigma'} c^{\dagger}_{\mathbf{k}\bar{\kappa}\sigma'} c_{\mathbf{k}-\mathbf{q}\bar{\kappa}\sigma}. \tag{C.9}$$

Using the mean field approximation on this interaction and combining terms that are identical after summation we obtain

$$H^{\mathrm{MF}}_J = -\frac{J}{N} \sum_{\mathbf{q}\mathbf{k}\mathbf{k}'} \sum_{\kappa\sigma\sigma'} \left\langle c^{\dagger}_{\mathbf{k}\kappa\sigma} c_{\mathbf{k}+\mathbf{q}\kappa\sigma'} \right\rangle c^{\dagger}_{\mathbf{k}'\bar{\kappa}\sigma'} c_{\mathbf{k}'-\mathbf{q}\bar{\kappa}\sigma} - \left\langle c^{\dagger}_{\mathbf{k}\kappa\sigma} c_{\mathbf{k}'-\mathbf{q}\bar{\kappa}\sigma} \right\rangle c^{\dagger}_{\mathbf{k}'\bar{\kappa}\sigma'} c_{\mathbf{k}+\mathbf{q}\kappa\sigma'}. \tag{C.10}$$

By reindexing $\mathbf{q}$, using the definitions of the mean fields in momentum space with knowledge that $2\mathbf{q}$ is a reciprocal lattice vector under our assumptions, we obtain the expression in the text.

$$H^{\mathrm{MF}}_J = -\frac{J}{\sqrt{N}} \sum_{\mathbf{q}\mathbf{k}} \sum_{\kappa\sigma\sigma'} \Delta^{\kappa\sigma\kappa\sigma'}_{\mathbf{q}+} c^{\dagger}_{\mathbf{k}\bar{\kappa}\sigma'} c_{\mathbf{k}+\mathbf{q}\bar{\kappa}\sigma} - \Delta^{\kappa\sigma\bar{\kappa}\sigma}_{\mathbf{q}+} c^{\dagger}_{\mathbf{k}\bar{\kappa}\sigma'} c_{\mathbf{k}+\mathbf{q}\kappa\sigma'}. \tag{C.11}$$

This is rewritten in the basis where we only consider momenta in the reduced Brillouin zone, starting with the Hartree term, only writing the sum over momentum vector

$$H^{\mathrm{H}}_J = \sum_{\mathbf{k}\in\mathrm{RBZ}} \left[\Delta^{\kappa\sigma\kappa\sigma'}_{\mathbf{0}+} \left(c^{\dagger}_{\mathbf{k}\bar{\kappa}\sigma'} c_{\mathbf{k}\bar{\kappa}\sigma} + \sum_i c^{\dagger}_{\mathbf{k}+\mathbf{M}_i\bar{\kappa}\sigma'} c_{\mathbf{k}+\mathbf{M}_i\bar{\kappa}\sigma} \right) + \right. \tag{C.12}$$

$$\left. \sum_j \Delta^{\kappa\sigma\kappa\sigma'}_{\mathbf{M}_j} \left(c^{\dagger}_{\mathbf{k}+\mathbf{M}_j\bar{\kappa}\sigma'} c_{\mathbf{k}\bar{\kappa}\sigma} + c^{\dagger}_{\mathbf{k}\bar{\kappa}\sigma'} c_{\mathbf{k}+\mathbf{M}_j\bar{\kappa}\sigma} + \sum_{i\neq j} c^{\dagger}_{\mathbf{k}+\mathbf{M}_i\bar{\kappa}\sigma'} c_{\mathbf{k}+\mathbf{M}_i\bar{\kappa}\sigma} \right) \right].$$

Similarly, computations can be made for the Fock contribution

$$H^{\mathrm{F}}_J = \sum_{\mathbf{k}\in\mathrm{RBZ}} \left[\Delta^{\kappa\sigma\bar{\kappa}\sigma}_{\mathbf{0}+} \left(c^{\dagger}_{\mathbf{k}\bar{\kappa}\sigma'} c_{\mathbf{k}\kappa\sigma'} + \sum_i c^{\dagger}_{\mathbf{k}+\mathbf{M}_i\bar{\kappa}\sigma'} c_{\mathbf{k}+\mathbf{M}_i\kappa\sigma'} \right) + \right. \tag{C.13}$$

$$\left. \sum_j \Delta^{\kappa\sigma\bar{\kappa}\sigma}_{\mathbf{M}_j} \left(c^{\dagger}_{\mathbf{k}+\mathbf{M}_j\bar{\kappa}\sigma'} c_{\mathbf{k}\kappa\sigma'} + c^{\dagger}_{\mathbf{k}\bar{\kappa}\sigma'} c_{\mathbf{k}+\mathbf{M}_j\kappa\sigma'} + \sum_{i\neq j} c^{\dagger}_{\mathbf{k}+\mathbf{M}_i\bar{\kappa}\sigma'} c_{\mathbf{k}+\mathbf{M}_i\kappa\sigma'} \right) \right].$$

The correction to the energy is written directly in terms of the mean fields

$$E_J^{\text{crxn}} = \frac{J}{2} \sum_{\mathbf{q}\kappa\sigma\sigma'} \left(\Delta_{\mathbf{q}+}^{\kappa\sigma\kappa\sigma'} \Delta_{\mathbf{q}+}^{\overline{\kappa}\sigma'\overline{\kappa}\sigma} - \Delta_{\mathbf{q}+}^{\kappa\sigma\overline{\kappa}\sigma} \Delta_{\mathbf{q}+}^{\overline{\kappa}\sigma'\kappa\sigma'} \right). \tag{C.14}$$

And finally the computations for the pair wise coupling, writing it in momentum space

$$H_{J'} = \frac{J'}{N} \sum_{\mathbf{q}\mathbf{k}\mathbf{k}'} \sum_{\kappa} c_{\mathbf{k}\kappa\uparrow}^{\dagger} c_{\mathbf{k}+\mathbf{q}\overline{\kappa}\uparrow} c_{\mathbf{k}\kappa\downarrow}^{\dagger} c_{\mathbf{k}-\mathbf{q}\overline{\kappa}\downarrow}. \tag{C.15}$$

Using the mean field approximation on this interaction and writing the expression using a sum over spins, yields

$$H_{J'}^{\text{MF}} = \frac{J'}{N} \sum_{\mathbf{q}\mathbf{k}\mathbf{k}'} \sum_{\kappa\sigma} \left\langle c_{\mathbf{k}\kappa\sigma}^{\dagger} c_{\mathbf{k}+\mathbf{q}\overline{\kappa}\sigma} \right\rangle c_{\mathbf{k}'\kappa\overline{\sigma}}^{\dagger} c_{\mathbf{k}'-\mathbf{q}\overline{\kappa}\,\overline{\sigma}} - \left\langle c_{\mathbf{k}\kappa\sigma}^{\dagger} c_{\mathbf{k}'-\mathbf{q}\overline{\kappa}\,\overline{\sigma}} \right\rangle c_{\mathbf{k}'\kappa\overline{\sigma}}^{\dagger} c_{\mathbf{k}+\mathbf{q}\overline{\kappa}\sigma}. \tag{C.16}$$

By reindexing $\mathbf{q}$, using the definitions of the mean fields in momentum space with knowledge that $2\mathbf{q}$ is a reciprocal lattice vector under our assumptions, we obtain the expression in the text.

$$H_{J'}^{\text{MF}} = \frac{J'}{\sqrt{N}} \sum_{\mathbf{q}\mathbf{k}} \sum_{\kappa\sigma\sigma'} \Delta_{\mathbf{q}+}^{\kappa\sigma\overline{\kappa}\sigma} c_{\mathbf{k}\kappa\overline{\sigma}}^{\dagger} c_{\mathbf{k}+\mathbf{q}\overline{\kappa}\,\overline{\sigma}} - \Delta_{\mathbf{q}+}^{\kappa\sigma\overline{\kappa}\,\overline{\sigma}} c_{\mathbf{k}\kappa\overline{\sigma}}^{\dagger} c_{\mathbf{k}+\mathbf{q}\overline{\kappa}\sigma}. \tag{C.17}$$

This is rewritten in the basis where we only consider momenta in the reduced Brillouin zone, starting with the Hartree term, only writing the sum over momentum vector

$$\begin{aligned} H_{J'}^{\text{H}} = \sum_{\mathbf{k}\in\text{RBZ}} \Bigg[& \Delta_{\mathbf{0}+}^{\kappa\sigma\overline{\kappa}\sigma} \left(c_{\mathbf{k}\kappa\overline{\sigma}}^{\dagger} c_{\mathbf{k}\overline{\kappa}\,\overline{\sigma}} + \sum_i c_{\mathbf{k}+\mathbf{M}_i\kappa\overline{\sigma}}^{\dagger} c_{\mathbf{k}+\mathbf{M}_i\overline{\kappa}\,\overline{\sigma}} \right) + \\ & \sum_j \Delta_{\mathbf{M}_j}^{\kappa\sigma\overline{\kappa}\sigma} \left(c_{\mathbf{k}+\mathbf{M}_j\kappa\overline{\sigma}}^{\dagger} c_{\mathbf{k}\overline{\kappa}\,\overline{\sigma}} + c_{\mathbf{k}\kappa\overline{\sigma}}^{\dagger} c_{\mathbf{k}+\mathbf{M}_j\overline{\kappa}\,\overline{\sigma}} + \sum_{i\neq j} c_{\mathbf{k}+\mathbf{M}_i\overline{\kappa}\sigma'}^{\dagger} c_{\mathbf{k}+\mathbf{M}_i\overline{\kappa}\,\overline{\sigma}} \right) \Bigg]. \end{aligned} \tag{C.18}$$

Similarly, computations can be made for the Fock contribution

$$\begin{aligned} H_{J'}^{\text{F}} = \sum_{\mathbf{k}\in\text{RBZ}} \Bigg[& \Delta_{\mathbf{0}+}^{\kappa\sigma\overline{\kappa}\,\overline{\sigma}} \left(c_{\mathbf{k}\kappa\overline{\sigma}}^{\dagger} c_{\mathbf{k}\overline{\kappa}\sigma} + \sum_i c_{\mathbf{k}+\mathbf{M}_i\kappa\overline{\sigma}}^{\dagger} c_{\mathbf{k}+\mathbf{M}_i\overline{\kappa}\sigma} \right) + \\ & \sum_j \Delta_{\mathbf{M}_j}^{\kappa\sigma\overline{\kappa}\,\overline{\sigma}} \left(c_{\mathbf{k}+\mathbf{M}_j\kappa\overline{\sigma}}^{\dagger} c_{\mathbf{k}\overline{\kappa}\sigma} + c_{\mathbf{k}\kappa\overline{\sigma}}^{\dagger} c_{\mathbf{k}+\mathbf{M}_j\overline{\kappa}\sigma} + \sum_{i\neq j} c_{\mathbf{k}+\mathbf{M}_i\kappa\overline{\sigma}}^{\dagger} c_{\mathbf{k}+\mathbf{M}_i\overline{\kappa}\sigma} \right) \Bigg]. \end{aligned} \tag{C.19}$$

The correction to the energy is written directly in terms of the mean fields

$$E_{J'}^{\text{crxn}} = -J' \sum_{\mathbf{q}\kappa\sigma} \Delta_{\mathbf{q}+}^{\kappa\sigma\overline{\kappa}\sigma} \Delta_{\mathbf{q}+}^{\kappa\overline{\sigma}\,\overline{\kappa}\,\overline{\sigma}} - \Delta_{\mathbf{q}+}^{\kappa\sigma\overline{\kappa}\,\overline{\sigma}} \Delta_{\mathbf{q}+}^{\kappa\overline{\sigma}\,\overline{\kappa}\sigma}. \tag{C.20}$$